SIMULATION-BASED ANALYSIS OF REENTRY DYNAMICS FOR THE SHARP ATMOSPHERIC ENTRY VEHICLE

A THESIS
SUBMITTED TO THE DEPARTMENT OF
AERONAUTICS AND ASTRONAUTICS
AND THE COMMITTEE ON GRADUATE STUDIES
OF STANFORD UNIVERSITY
IN PARTIAL FULFILLMENT OF THE REQUIREMENTS
FOR THE DEGREE OF
ENGINEER

By
Clemens Emmanuel Tillier
May 1998

ABSTRACT

This thesis describes the analysis of the reentry dynamics of a high-performance lifting atmospheric entry vehicle through numerical simulation tools. The vehicle, named SHARP, is currently being developed by the Thermal Protection Materials and Systems branch of NASA Ames Research Center, Moffett Field, California. The goal of this project is to provide insight into trajectory tradeoffs and vehicle dynamics using simulation tools that are powerful, flexible, user-friendly and inexpensive. Implemented using MATLAB and SIMULINK, these tools are developed with an eye towards further use in the conceptual design of the SHARP vehicle's trajectory and flight control systems.

A trajectory simulator is used to quantify the entry capabilities of the vehicle subject to various operational constraints. Using an aerodynamic database computed by NASA and a model of the earth, the simulator generates the vehicle trajectory in three-dimensional space based on aerodynamic angle inputs. Requirements for entry along the SHARP aerothermal performance constraint are evaluated for different control strategies. Effect of vehicle mass on entry parameters is investigated, and the cross range capability of the vehicle is evaluated. Trajectory results are presented and interpreted.

A six degree of freedom simulator builds on the trajectory simulator and provides attitude simulation for future entry controls development. A Newtonian aerodynamic model including control surfaces and a mass model are developed. A visualization tool for interpreting simulation results is described. Control surfaces are roughly sized. A simple controller is developed to fly the vehicle along its aerothermal performance constraint using aerodynamic flaps for control. This end-to-end demonstration proves the suitability of the 6-DOF simulator for future flight control system development.

Finally, issues surrounding real-time simulation with hardware in the loop are discussed.

I certify that I have read this thesis and that in my opinion it is fully adequate, in scope and quality, as a thesis for the degree of Engineer.

Robert Twiggs, Academic Advisor

I certify that I have read this thesis and that in my opinion it is fully adequate, in scope and quality, as a thesis for the degree of Engineer.

Ilan Kroo, Principal Advisor

Approved for the University Committee on Graduate Studies:

ACKNOWLEDGEMENTS

This research was carried out under the direction of Prof. Robert Twiggs, in the Space Systems Development Laboratory (SSDL), Department of Aeronautics and Astronautics, Stanford University. Prof. Twiggs provided this research opportunity, found the funds to purchase software and hardware, participated in all phases of the process, and provided moral support. Paul Kolodziej of the Thermal Protection Materials and Systems branch at NASA Ames Research Center provided technical advice on SHARP, motivated many of the problems described in this thesis, provided literature references, and reviewed the work as it progressed. Prof. Ilan Kroo was the principal advisor and provided many useful suggestions, especially in the area of aerodynamics. Prof. Michael Tauber taught the excellent course on atmospheric entry, AA213. This course provided much of the basic knowledge required to perform this research. SSDL doctoral candidates Christopher Kitts and Michael Swartwout participated in the review process and offered many useful suggestions as writing progressed. Joseph Carroll and Robert Cunningham gave useful advice in the early stages of this project. Finally, thanks are due to the SSDL student crew, friends, and family – I won't name anyone for fear of forgetting someone. This research was carried out under the NASA Ames University Consortium, Interchange for Joint Research, funding grant number NCC2-5197 from January 1997 to May 1998.

CONTENTS

CHAPTER 1: INTRODUCTION 1
1.1: Problem Statement 1
1.2: Background and Motivation 2
1.2.1: Atmospheric Entry 2
1.2.2: Lifting Atmospheric Entry 3
1.2.3: Directions in Thermal Protection System Research 4
1.2.4: Sharp Leading Edges 5
1.2.5: Ultra High Temperature Ceramics 7
1.2.6: The SHARP Vehicle 9
1.2.7: Current SHARP Status and Needs 10
1.3: Development Approach and Thesis Overview 11
1.4: Significant Contributions 12
CHAPTER 2: SIMULATOR COMPONENT SELECTION 13
2.1: Bandwidth Requirement Estimation 13
2.1.1: Longitudinal Vehicle Dynamics 13
2.2: Software Selection 17
2.3: Hardware Selection 18
CHAPTER 3: TRAJECTORY SIMULATION 19
3.1: Simulator Implementation 19
3.1.1: Architecture 19
3.1.2: Modeling Details 20
3.2: Simulator Verification 21
3.2.1: Pullout Experiment 1: Effect of Vehicle Mass 22

3.2.2: Pullout Experiment 2: Effect of Angle of Attack 22
3.3: Simulator Applications and Results 23
3.3.1: Entry along Aerothermal Performance Constraint 23
3.3.1.1: High L/D Entry 25
3.3.1.2: Low L/D Entry 30
3.3.1.3: Trajectory Comparison and Discussion 33
3.3.2: Effect of Vehicle Mass on Entry Parameters 36
3.3.2.1: SHARP Vehicle 36
3.3.2.2: Scaled Up Vehicles 38
3.3.2.3: Trajectory Comparison and Discussion 39
3.3.3: Entry with High Cross Range 40
3.3.4: Entry with Ballistic Missile Launch 44
3.4: Summary 45
CHAPTER 4: ENTRY SIMULATION, 6-DOF 46
4.1: Simulator Implementation 46
4.1.1: Architecture 46
4.1.2: Modeling Details 47
4.2: SHARP Newtonian Aerodynamic Model 48
4.2.1: Geometrical Representation 49
4.2.2: Aerodynamic Computation 50
4.2.3: Model Verification 52
4.3: Simulator Verification 55
4.4: Simulation Visualization 55
4.5: Simulator Applications and Results 57
4.5.1: Control Surface Sizing 57
4.5.2: Aerodynamic Angle Control 60
4.5.2.1: Controller Details 60
4.5.2.2: Demonstration Results 61
4.6: Summary 65
CHAPTER 5: REAL TIME SIMULATION ISSUES 66
5.1: Background 66
5.2: A Low Cost HWIL System for SHARP 67

5.2.1: Channel Limitations 68
5.2.2: Processing Speed Limitations 69
5.2.3: Cost Constraints 71
5.3: Summary 71
CHAPTER 6: CONCLUSIONS AND FUTURE WORK 73
6.1: Conclusions 73
6.1.1: Trajectory Simulation 73
6.1.2: 6-DOF Simulation 74
6.1.3: Real Time Capability 75
6.2: Suggestions for Future Work 76
6.2.1: Trajectory Optimization 76
6.2.2: Improved Aerodynamic Model 76
6.2.3: Flight Control System Development 77
6.2.4: Hardware Development 77
APPENDIX A: SHARP VEHICLE PARAMETERS 78
A.1: Geometry 78
A.2: Mass Properties 79
A.2.1: Mass Distribution 79
A.2.2: Moments of Inertia 80
APPENDIX B: TRAJECTORY SIMULATOR DESCRIPTION 81
B.1: Model Block Diagram 81
B.2: Block Descriptions 83
B.3: User's Guide 86
APPENDIX C: TRAJECTORY SIMULATION DATA 87
C.1: Data Key 87
APPENDIX D: 6-DOF SIMULATOR DESCRIPTION 99
D.1: Model Block Diagram 99
D.2: Block Descriptions 101
D.3: Files for Newtonian Model 103
D.4: User's Guide 105
REFERENCES 107

LIST OF TABLES

Table 3-1: Pullout experiment initial conditions 22
Table 3-2: Pullout experiment 1 results 22
Table 3-3: Pullout experiment 2 results 23
Table 3-4: APC entry initial conditions 23
Table 3-5: Trajectory comparison 34
Table 3-6: Trajectory comparison 39
Table A-1: SHARP inertia properties 80
Table C-1: Symbol key 87
Table C-2: High lift to drag entry along the APC 88
Table C-3: Low lift to drag entry along the APC 91
Table C-4: Entry with high cross range 94

LIST OF FIGURES

Figure 1-1: UHTC leading edge assembly 8
Figure 1-2: SHARP B-01 test vehicle (left) 9
Figure 1-3: SHARP wire frame model 10
Figure 2-1: Pitching moment (example) 15
Figure 2-2: Short period pitch frequency (Hz) 16
Figure 3-1: Simulator architecture 20
Figure 3-2: Composite desired entry profile 24
Figure 3-3: Entry profile 26
Figure 3-4: Altitude error 26
Figure 3-5: Angle of attack profile 27
Figure 3-6: Lift to drag ratio 28
Figure 3-7: Aft-body heating rate 29
Figure 3-8: Body z-axis acceleration 29
Figure 3-9: Entry profile 31
Figure 3-10: Altitude error 31
Figure 3-11: Roll angle profile 32
Figure 3-12: Aft-body heating rate 32
Figure 3-13: Body z-axis acceleration 33
Figure 3-14: Radiative TPS summary (Anderson and Swann) 35
Figure 3-15: Effect of vehicle mass on AOA profile 37
Figure 3-16: Effect of vehicle mass on aft-body heating 38
Figure 3-17: Entry profile 41
Figure 3-18: Earth-referenced ground path 42

Figure 3-19: Angle of attack profile 43
Figure 3-20: Lift to drag ratio 43
Figure 3-21: Pullout from ballistic trajectory 45
Figure 4-1: Simulator architecture 47
Figure 4-2: SHARP wire frame model 49
Figure 4-3: Flap control modes (front view) 50
Figure 4-4: Polygon computation geometry 51
Figure 4-5: Lift coefficient comparison 53
Figure 4-6: Drag coefficient comparison at Mach 5, 10 and 20 54
Figure 4-7: Pitch moment coefficient comparison at Mach 5, 10 and 20 55
Figure 4-8: Predicted vs. measured pitch frequency 56
Figure 4-9: Raw simulation results 56
Figure 4-10: Visualization of simulation results 57
Figure 4-11: Pitch control authority 58
Figure 4-12: Yaw control authority 59
Figure 4-13: Controller architecture 61
Figure 4-14: Entry profile 62
Figure 4-15: Altitude error 63
Figure 4-16: Angle of attack profile 63
Figure 4-17: Flap position angle profile 64
Figure 5-1: Hardware in the loop system architecture 67
Figure 5-2: Analog output multiplexing 69
Figure A-1: SHARP vehicle geometry 78
Figure A-2: Simplified wedge geometry 79
Figure B-1: Trajectory simulator block diagram 82
Figure D-1: 6-DOF simulator block diagram 100

LIST OF SYMBOLS

A: Reference area (m^2)

a: Sound speed (m/s) or acceleration (m/s^2), according to context

α: Angle of attack (degrees)

α_i: Induced angle of attack (degrees)

β: Angle of sideslip (degrees)

c: Proportionality constant

C_D: Drag coefficient

C_f: Fiction coefficient

C_L: Lift coefficient

C_m: Pitching moment coefficient

C_p: Pressure coefficient

D: Drag (N)

δ: Angle of flow incidence

ϕ: Aerodynamic roll angle (degrees), not body roll angle

γ: Flight path angle (degrees)

γ_B: Angle between body x-axis and horizontal (degrees)

h: Altitude (m) or vehicle height (m), according to context

I_x: Roll moment of inertia ($kg \cdot m^2$)

I_y: Pitch moment of inertia ($kg \cdot m^2$)

I_z: Yaw moment of inertia ($kg \cdot m^2$)

L: Lift (N)

l: Vehicle length (m)

M: Vehicle mass (kg)

M_∞: Free stream Mach number

p: Body yaw rate (rad/s)

q: Free stream dynamic pressure (N/m^2) or body pitch rate (rad/s), according to context

$\dot{q}_s$: Stagnation point heating rate (W/m^2)

r: Body roll rate (rad/s)

r_n: Nose radius (m)

T: Temperature (K)

t: Time (s)

V_∞: Free stream velocity (m/s)

ω_y: Pitch frequency (Hz)

ψ: Earth-referenced heading angle (degrees)

ψ_B: Body heading angle (degrees)

LIST OF ACRONYMS

A/D: Analog to Digital

APC: Aerothermal Performance Constraint

D/A: Digital to Analog

6-DOF: Six Degree of Freedom

DPC: Dynamic Pressure Constraint

HWIL: Hardware in the Loop

L/D: Lift to Drag

LEO: Low Earth Orbit

NASA: National Aeronautics and Space Administration

PC: Personal Computer

PID: Proportional, Integral, Derivative

RLV: Reusable Launch Vehicle

SHARP (1): Slender Hypervelocity Aerothermodynamic Research Probes

SHARP (2): Sharp Hypersonic Aerodynamic Research Probe

SSDL: Space Systems Development Laboratory (Stanford)

TPS: Thermal Protection System

UHTC: Ultra High Temperature Ceramic

CHAPTER 2:
SIMULATOR COMPONENT SELECTION

The requirements leading to the selection of the software and hardware necessary to build the simulation tools are explored. Primarily this consists of using an aerodynamic database for SHARP, provided by NASA, to determine the expected bandwidth of the simulation system. The results of this analysis motivate the choice of commercial off-the-shelf software and hardware for building the simulation tools.

2.1 Bandwidth Requirement Estimation

Dynamical bandwidth plays a critical role in the design of a simulator where real-time capability is desired. In order to ensure meaningful and accurate results, the recalculation frequency of the simulation must be significantly above the maximum frequency in the dynamics of the vehicle being simulated. These dynamics must therefore be the subject of a preliminary investigation before frequency requirements can be set for the simulation system.

2.1.1 Longitudinal Vehicle Dynamics

The approach used to analyze the dynamics of the SHARP vehicle is the same as commonly used for any aircraft. The aim is to calculate the frequency of the fastest natural mode of the vehicle under the range of expected flight conditions. From experience, the fastest mode is expected to be the short-period pitch oscillation. A non real-time simulation where the simulator bandwidth is not a constraint (see Chapter 4)

later confirms this, allowing a numerically accurate determination of the vehicle dynamics.

In the short-period pitch mode, the vehicle's angle of attack α exhibits simple harmonic motion about some equilibrium pitch, which we take to be zero. The vehicle could also oscillate about some non-zero pitch trimmed equilibrium, but this produces essentially the same motion.

In this analysis pitch damping can be neglected, as is shown next. The perturbation to the angle of attack that is induced by the rotation of the body is given by

$$\tan\alpha_i = \dot{\alpha} l / V_\infty ,$$

where l is the vehicle length and V_∞ is the free stream velocity. In hypersonic flight of a small body, where l is small and V_∞ is large, we have $\alpha_i << \alpha$. The aerodynamic forces induced by pitch rotation are therefore negligible, compared to other forces such as the restoring force from which the harmonic motion arises. The short-period pitch motion can thus be realistically modeled as an undamped simple harmonic oscillator,

$$I_y \ddot{\alpha} + c\alpha = 0 .$$

The pitch moment-of-inertia I_y is estimated from the vehicle characteristics, and is computed in Appendix A. The constant c relates the restoring torque to α, and depends on the aerodynamic properties of the vehicle and the dynamic pressure.

The NASA-provided aerodynamic database for the SHARP vehicle geometry is used to compute a numerical value of c for any given flight condition. The database gives the lift and drag coefficients C_L and C_D, as well as the location of the center of pressure (where the lift and drag forces act) for any flight condition, as defined by the free stream Mach number M_∞, dynamic pressure q, and the vehicle angle of attack α. Knowing the location of the vehicle center of gravity, the database is used to compute the total aerodynamic force on the vehicle and its moment arm about the center of gravity. For any value of M_∞ and q, a plot of the pitching moment versus α is constructed, and the proportionality constant c is determined by fitting a straight line to the data through the origin. Using

MATLAB [MathWorks 1997], this technique gives a numerical value for c over a range of M_∞ and q. An example of a pitch torque plot is shown in Figure 2-1.

The pitch oscillation frequency ω_y is given by

$$\omega_y = \sqrt{\frac{c}{I_y}}.$$

This result allows us to produce a contour plot of the pitch frequency as a function of Mach number and dynamic pressure. The result is shown in Figure 2-2.

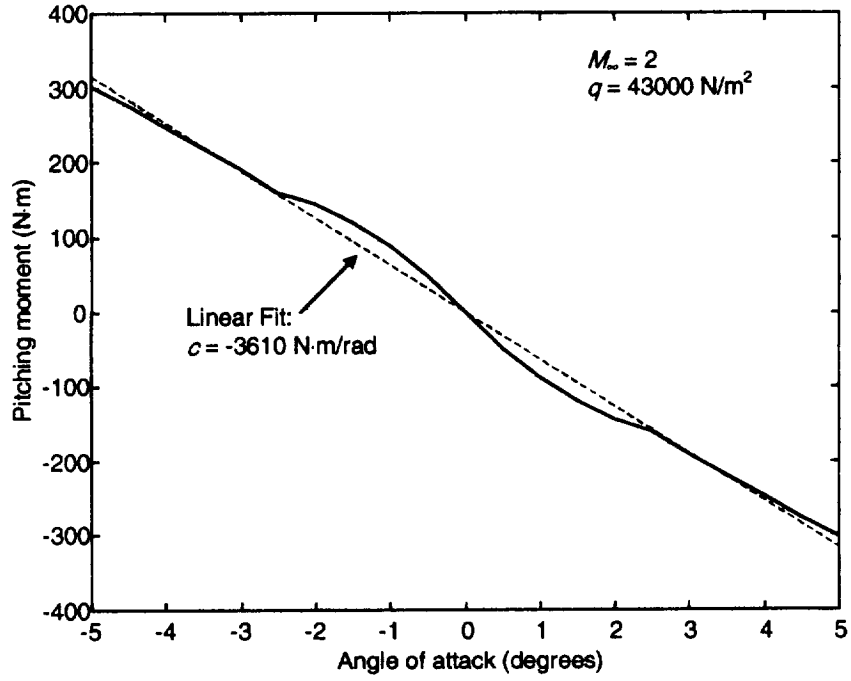

Figure 2-1: Pitching moment (example)

Under real operating conditions not every combination of Mach number and dynamic pressure can be attained. In particular, thermal considerations limit the possible velocity at any given altitude, and structural constraints limit the allowable dynamic pressure to 43000 N/m^2. Thus, several regions of the plot that lie outside of the flight envelope can be immediately excluded from consideration. The thermal limit, or aerothermal performance constraint (APC), is discussed in more detail in Chapter 3, as is the choice of dynamic pressure constraint.

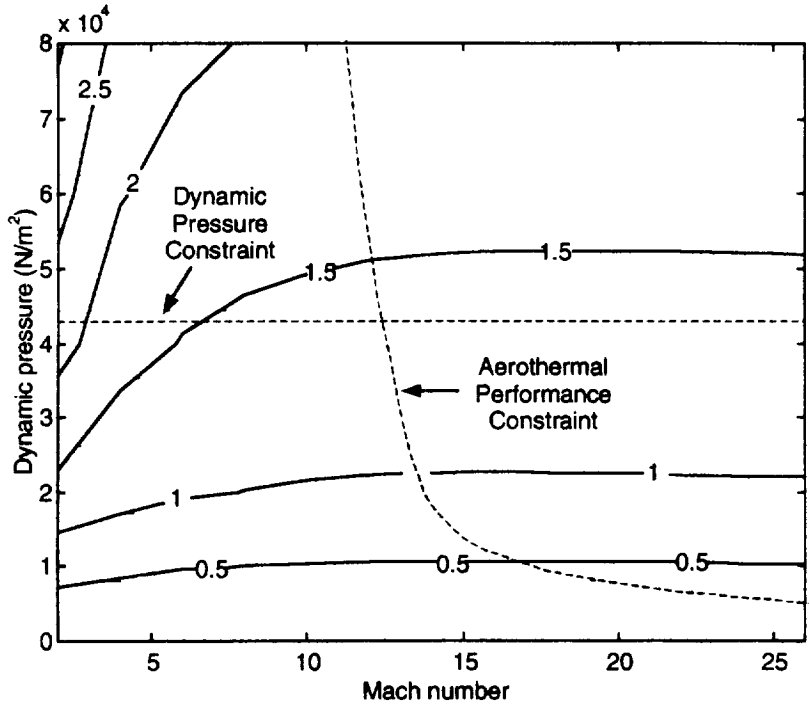

Figure 2-2: Short-period pitch frequency (Hz)

The APC is given in velocity-altitude, or (V_∞, h) coordinates. A coordinate transformation performed on the NASA-provided APC data allows expressing it instead in free stream Mach number-dynamic pressure, or (M_∞, q) coordinates. To do this, atmospheric density $\rho(h)$ and sound speed $a(h)$ are looked up for a given altitude h using the 1976 US Standard Atmosphere [NOAA 1976]. Thus, $M_\infty(V_\infty, h)$ and $q(V_\infty, h)$ can be obtained. The resulting transformed APC is overlaid on Figure 2-2.

The constraints delimit an area of Figure 2-2, below the constraint curves, that describes the flight envelope of the vehicle. Within this area the fastest longitudinal mode lies at approximately 2.5 Hz, a condition achieved at low speed and high dynamic pressure. For most of the flight conditions of interest the frequency is even lower.

Taking into account an appropriate margin and over-sampling rate, the requirement for the simulator is set at 30 Hz. This value provides adequate capability for accurately simulating the dynamics of the vehicle in real time. This value suggests the task is feasible using affordable off-the-shelf hardware and software.

2.2 Software Selection

Commercial off-the-shelf packages were favored over hand coding the simulation software, for reasons of time, cost and performance. Several powerful and full-featured off-the-shelf software packages are available for performing simulation. One of these is SIMULINK [MathWorks 1997]. SIMULINK is an interactive environment for modeling and simulating a wide variety of dynamic systems, including linear, non-linear, discrete-time, continuous-time, and hybrid systems. It combines the power and ease of use of an application package with the flexibility and extensibility of a language. Combined with the computation package MATLAB [MathWorks 1997], SIMULINK provides an ideal integrated environment for developing the simulation tools for SHARP. The reasons for choosing SIMULINK were:

- Ease of use. SIMULINK provides an intuitive visual interface where the user can click-and-drag components to assemble models in the familiar block diagram form.

- Affordability. SIMULINK is widely available and can run on inexpensive personal computers. SIMULINK models can also be run on high power workstations with little or no modification.

- Extensibility. SIMULINK models can be extended and modified at will with very little difficulty. If the model had been hand-coded directly in a computer language the desired modularity would have been difficult and time-consuming to provide.

- Power. SIMULINK has built-in integration schemes that are efficient and optimized. These schemes would have been difficult and time-consuming to implement in a fully custom simulator. The wide array of linear and non-linear capabilities built into SIMULINK insulates the user from the numerical complexity of solving a large model.

- Interface to MATLAB. Computations performed in the familiar MATLAB environment can be integrated into a SIMULINK model. This is an important capability in situations where the block diagram representation is not the most intuitive way to perform the desired computation. In addition, output data from the model can be displayed using MATLAB's powerful visualization capabilities.

- Interface to Toolboxes. SIMULINK and MATLAB can gain additional capabilities from widely available external software components. These "toolboxes" include the Real Time Toolbox [Humusoft 1997]. This toolbox seamlessly interfaces a data acquisition board to the simulation software, enabling simulation parameters to be passed to and from a physical system outside of the simulation host computer. The hardware in the loop capability thus afforded, while limited, is inexpensive and easy to implement. Should better hardware in the loop performance become necessary, packages such as Real Time Workshop [MathWorks 1997] can generate native code from a SIMULINK model for any target embedded processor.

2.3 Hardware Selection

The hardware choice for the simulation system is largely constrained by the funds avialable for this research. The simulation host computer is a Pentium PC running Windows 95 at 150 MHz. This computer is pre-existing SSDL equipment and was not originally purchased as a simulation computer. With rapid progress in processor speed and power, the simulation can run faster as better hardware becomes available. The choice of SIMULINK, a widely used product, ensures that simulation software capability will follow future improvements in hardware capability.

There are several approaches for hardware in the loop, real time simulation. Typically they require powerful, custom-developed hardware; however, there has been success in 6-DOF hardware in the loop simulation using only low-performance PC hardware [Sims 1996]. Without knowing in advance the chances of success, a relatively low-performance but inexpensive system was selected and purchased. This includes the Real Time Toolbox (described in section 2.2) and a simple Data Translation data acquisition board. This board features eight 12-bit analog to digital converters, two 12-bit digital to analog converters, and sixteen digital I/O lines. The limited number of D/A channels is a concern, since more than two analog output signals are required to drive external hardware. This issue and other real-time simulation concerns are addressed in Chapter 5.

CHAPTER 3: TRAJECTORY SIMULATION

The trajectory simulator, using NASA-provided vehicle aerodynamics data, is used to evaluate the characteristics of certain mission scenarios. In each case the simulator provides some relevant parameter or insight for the trajectory considered. In particular, the capability for generating the aerodynamic angle profiles required to follow any desired trajectory in velocity-altitude space proves flexible and useful. The simulator generates the vehicle trajectory in three-dimensional space based on aerodynamic angle inputs. Depending on its configuration, the simulator computes four or five degrees of freedom: three position variables and either or both of angle of attack and roll angle. The simulator is not limited to the SHARP vehicle or Earth entry, as different vehicle databases and planetary characteristics can easily be substituted.

3.1 Simulator Implementation

3.1.1 Architecture

The trajectory simulator was built in the SIMULINK graphical environment [MathWorks 1997]. The function of the simulator is to compute forces on the vehicle and to step forward in time using Newton's second law, $F = ma$. The result of the computation is the motion of the vehicle in three dimensions and the associated aerodynamic angle histories.

The architecture of the simulator is as follows. For a given flight condition, aerodynamic forces on the vehicle (i.e. the lift and drag coefficients C_L and C_D) are calculated via a three-dimensional table lookup on angle of attack α, dynamic pressure q, and free stream

Mach number M_∞. The table used for this purpose was constructed from NASA-provided aerodynamic data specific to the SHARP vehicle geometry [Kolodziej 1997]. Through a series of coordinate transformations, the net acceleration experienced by the vehicle (due to lift, drag and gravity) is calculated in inertial space, and integrated twice to compute inertial velocity and position. These quantities, along with aerodynamic angle inputs, are used to determine the new flight condition. The overall cycle is depicted in Figure 3-1.

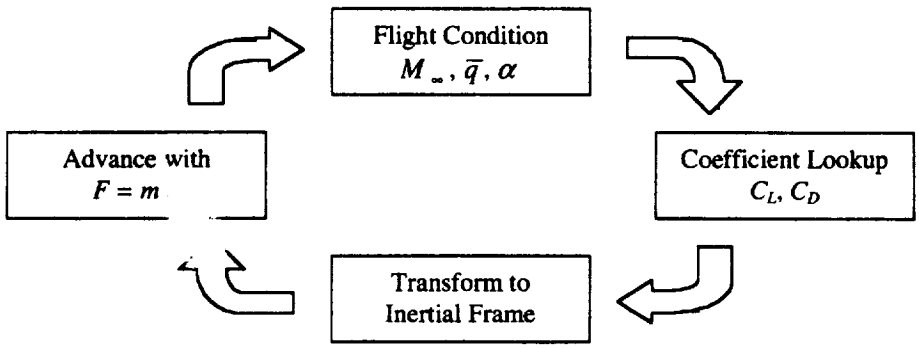

Figure 3-1: Simulator architecture

Angle of attack and angle of roll (about the velocity vector) can be commanded in open loop or based on feedback from any parameter in the model. Angle of sideslip is assumed zero throughout.

3.1.2 Modeling Details

The earth is modeled as an oblate, rotating spheroid. For computing gravitational forces it is considered a point mass and higher order terms of the multipole expansion of the gravitational field are not included. Lookup tables of scale height and sound speed, based on the 1976 US Standard Atmosphere [NOAA 1976], model the atmosphere. The vehicle's trajectory is controlled by direct command of the aerodynamic angles, namely angle of attack α and roll angle ϕ. Roll angle is defined about the velocity vector and not the body axis system. The angle of sideslip β is assumed to be zero throughout. Commanding angle of attack and roll angle may be effected in open loop or through feedback controllers using other parameters in the model to compute the desired angles. This direct commanding does not model the inertia properties of the vehicle or any

sensing or actuating devices. These features are implemented in the extension of the trajectory simulator to six degrees of freedom, described in Chapter 4.

The three coordinate frames used in the model (inertial, earth-referenced, and free-stream referenced) are related to each other via Euler angles. It was not deemed necessary to use the quaternion representation because the realistic range of the various angles precludes the gimbal lock problem.

Modeling of the thermal effects on the TPS can be included to monitor the time history of heating rates and temperature. While these results are not accurate due to a number of modeling assumptions, it can still be used as a qualitative metric in trajectory optimization studies where the thermal effects (maximum heating rate and integrated heat load) of various trajectories are compared among each other.

The time advancement scheme for the model is an adaptive-step fourth-order Runge-Kutta scheme built into SIMULINK. A complete and detailed description of the trajectory model and its usage, as well as a walk-through of each component, may be found in Appendix B.

3.2 Simulator Verification

The trajectory simulator was verified by comparing with results computed on another, unrelated simulator at Sandia National Laboratories by Dr. Larry Young [Young 1998]. While the vehicle aerodynamics data provided by NASA was the same for both models, the Sandia model used atmospheric data specific to the Kwajalein atoll in the South Pacific and a higher-order gravitational field.

Starting from a fixed initial condition, two different experiments were run: one at fixed angle of attack with varying vehicle weight, and another at fixed vehicle weight with varying angle of attack. The output parameter of interest was the pullout altitude, the altitude at which the vehicle flight path angle goes from below horizontal to above horizontal in a skipping trajectory. Initial conditions for the experiments are listed in the table below.

Longitude	169.4°
Latitude	10.3°
Altitude	60960 m
Entry angle	21.8°
Free stream velocity	6888.5 m/s

Table 3-1: Pullout experiment initial conditions

3.2.1 Pullout Experiment 1: Effect of Vehicle Mass

In this series of simulation runs, the angle of attack of the vehicle was taken to be constant at ten degrees and the mass was varied. The data in table 3-2 shows that the results from the two simulations come within less than a percent of each other, thereby validating the trajectory simulation. The small discrepancy likely arises from the differences in the geophysical model and from the initial heading angle, which was not known for the Sandia simulation.

Vehicle mass (kg)	Sandia pullout altitude (m)	Pullout altitude (m)	Difference
90.72	29633	29682	0.17 %
99.79	28987	29060	0.25 %
108.86	28401	28480	0.28 %
117.93	27863	27964	0.36 %
127.00	27368	27474	0.39 %
136.08	26909	27020	0.41 %
145.15	26480	26608	0.48 %
154.22	26080	26208	0.49 %
163.29	25703	25831	0.50 %

Table 3-2: Pullout experiment 1 results

3.2.2 Pullout Experiment 2: Effect of Angle of Attack

In the second series of simulation runs, the mass of the vehicle was taken to be constant at 136 kg and the angle of attack was varied. While the Sandia simulation results were given for angles of attack down to 0.5 degrees, this required extrapolation of the aerodynamic data to very high dynamic pressures. Table 3-3 shows only those values for which the flight parameters stayed within the range of the NASA aerodynamic data,

where a comparison is meaningful. Once again the different simulations came within less than one half of a percent, further increasing confidence in the model.

Angle of attack (deg)	Sandia pullout altitude (m)	Pullout altitude (m)	Difference
10.0	26909	27020	0.41 %
9.5	26542	26666	0.47 %
9.0	26155	26286	0.50 %
8.5	25746	25873	0.49 %

Table 3-3: Pullout experiment 2 results

3.3 Simulator Applications and Results

The trajectory simulator was successfully used to investigate a series of entry scenarios as requested by NASA. Simulation results provided key insights into the trajectory capabilities of the SHARP vehicle.

3.3.1 Entry along Aerothermal Performance Constraint

The aerothermal performance constraint (APC) is a contour, usually displayed in velocity-altitude space, which describes the thermal limits of a thermal protection system (TPS). At altitudes below this constraint and for a given velocity, the thermal performance is exceeded and the TPS is damaged or destroyed. Therefore, the entry trajectory must not cross much below the APC. In the case of SHARP it is desirable to fly closely along the constraint to compare actual and predicted TPS performance [Kolodziej 1998]. The SHARP APC was provided by NASA and describes the non-catalytic, multiple-use performance constraint of the ceramic leading edge.

In the simulation, the vehicle was assumed to start from a 400-km circular, equatorial orbit, after effecting a 98.5 m/s maneuver to drop the perigee of the orbit into the upper atmosphere to begin the entry. The resulting initial conditions are shown in Table 3-4:

Altitude	66446 m
Entry angle	0.452°
Free stream velocity	7435 m/s

Table 3-4: APC entry initial conditions

In velocity-altitude coordinates, the desired entry trajectory is a composite of three segments, beginning with a pullout maneuver to transfer from the incoming orbit to the next segment, flight along the APC, followed by a transition to a constant dynamic pressure profile when lower altitudes are reached. Due to structural requirements the dynamic pressure profile was fixed at 43000 N/m^2, in keeping with typical high dynamic pressure RLV trajectories [Windhorst 1997]. The composite entry profile, shown in Figure 3-2, is consistent with the mission goals of the SHARP lifting entry demonstration.

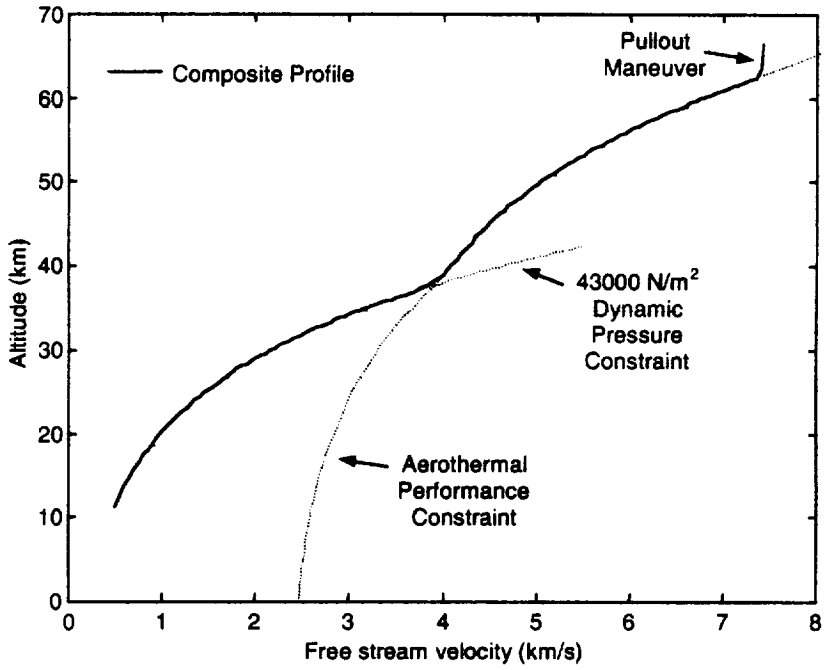

Figure 3-2: Composite desired entry profile

A given trajectory in velocity-altitude space such as in Figure 3-2 can be flown in an infinite number of ways. The constraint fixes the ratio of sink rate (*dh/dt*) to deceleration (*dv/dt*), but does not dictate a particular value of sink rate or deceleration. High values of sink rate and deceleration result in trajectories that follow the profile in a short time. Conversely, low values of sink rate and deceleration result in trajectories that follow the profile more slowly. Indeed, by using thrust one could stay fixed on one point in the velocity-altitude diagram, namely at a fixed velocity and altitude, or even fly back and forth along the entry profile.

To identify the range of trajectory capabilities of the SHARP vehicle in the context of its mission to test the new ceramic TPS, two different entries are simulated, both subject to the entry constraint in Figure 3-2. In the first, the vehicle's roll angle is fixed at zero and its angle of attack is modulated to follow the profile. In the second, the vehicle's angle of attack is fixed at 20 degrees and its roll angle is modulated to follow the profile. The first entry is flown at relatively high L/D, lasts longer, travels further, and incurs a larger integrated heat load for the TPS. The second entry is flown at low L/D, is of much shorter duration, and incurs a lower total heat load but higher structural loads. The two contrasting entries define the boundaries of the trajectory design space for the SHARP vehicle geometry, given the desired entry profile of Figure 3-2. The final choice of trajectory for the SHARP lifting demonstration necessarily lies somewhere in between the two extremes. This choice is largely a matter of establishing acceptable limits on thermal and structural loads; this issue is discussed in section 3.3.1.3.

3.3.1.1 High L/D Entry

The first entry, with the highest possible lift and lowest possible drag subject to the entry profile constraint, corresponds to an entry with zero roll angle (i.e. full use of the lift force against gravity) and modulation of the angle of attack α to follow the constraint. This results in a relatively long-lasting entry and high heat loads for the TPS. In the simulation, α was controlled in closed loop by using the altitude deviation from the constraint as an error signal. A PID controller was used to produce an acceptably small deviation from the constraint without excessive oscillations.

Figure 3-3 shows the resulting velocity-altitude profile, with tick marks at one-minute intervals. When the vehicle slows below Mach 2 at the end of the trajectory, the elapsed time is 57 minutes.

Figure 3-4 shows the altitude error in velocity-altitude space, in keeping with the representation of the entry profile. The data shows the vehicle following the profile very closely; the deviations can be attributed to the performance limitations of the PID controller. The good agreement is not intended as a demonstration of controller performance, but rather as a measure of how closely the entry trajectory follows the

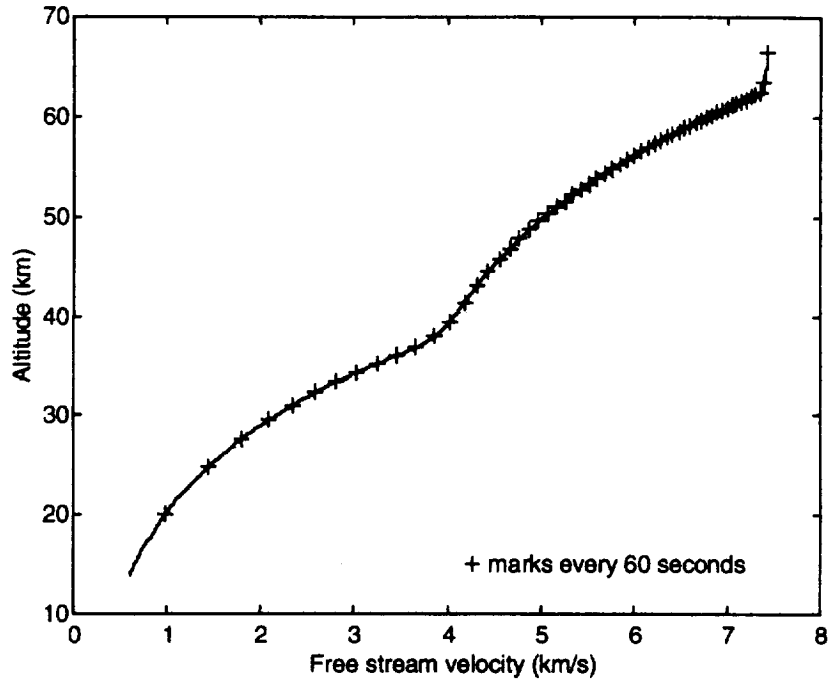

Figure 3-3: Entry profile

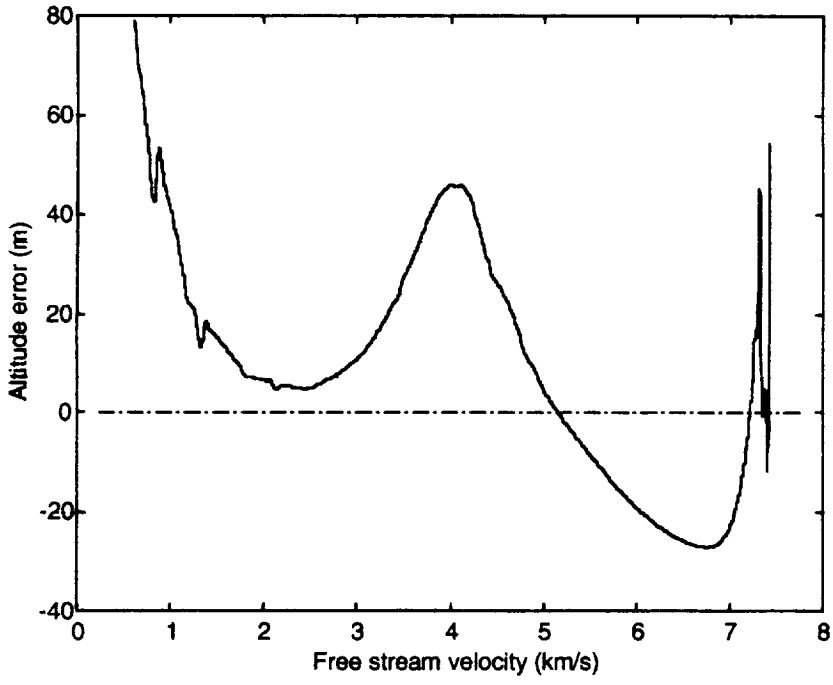

Figure 3-4: Altitude error

desired profile. This shows that the data for this trajectory is a valid representation of a high lift, low drag entry along the desired profile.

Figure 3-5 shows the resulting angle of attack profile, versus elapsed time, for the entire entry. The data shows the vehicle's α never exceeds four degrees, less than the half-angle of the wedge (refer to Appendix A for the SHARP vehicle geometry). This signifies that the top surface of the wedge would be facing into the flow during the entire entry, which could have important implications in the design and configuration of the aerodynamic control surfaces. The pullout maneuver appears in the first 200 seconds of the plot. The ringing is due to performance limitations of the controller in the face of sudden changes.

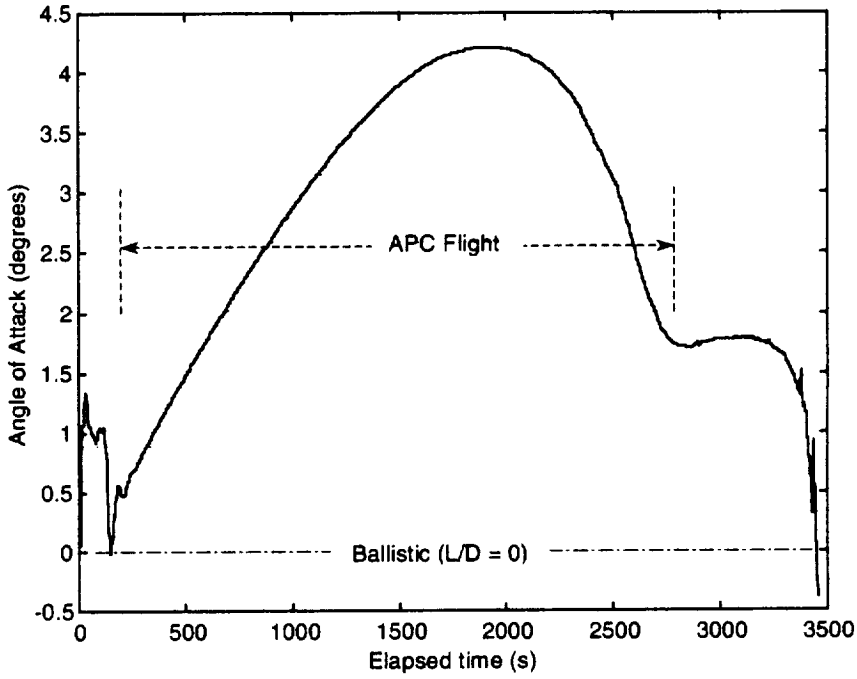

Figure 3-5: Angle of attack profile

Figure 3-6 shows the vehicle lift-to-drag ratio as a function of elapsed time. While the trajectory is not optimized for high L/D, the sharp wedge geometry demonstrates a hypersonic glide performance that far exceeds that of current RLV designs. In general for this entry the vehicle is flying at a lower than optimal α for maximum L/D, so still greater performance is possible, subject to the constraints of total heat load. An entry trajectory with yet higher L/D is described in section 3.3.3.

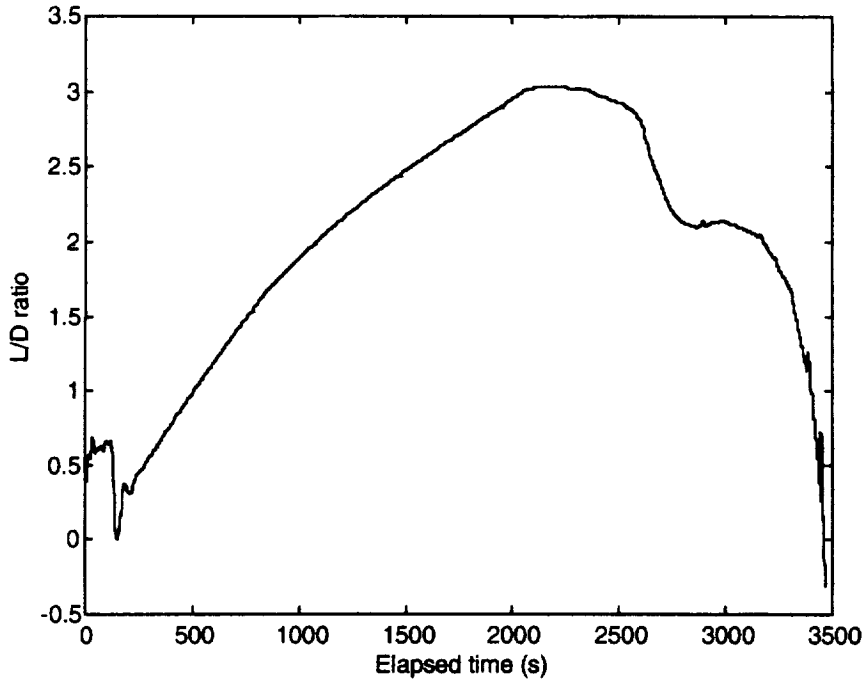

Figure 3-6: Lift-to-drag ratio

Figure 3-7 shows the heating rate at a point halfway along the wedge aft-body on its bottom (flow-facing) side. The heating rates are obtained by assuming Newtonian wedge flow and radiative thermal equilibrium; for modeling details see Appendix B. The time-integrated heat load, of interest in the design of the aft-body TPS, is 29600 joules per square centimeter. For purposes of calculating the total integrated heat load, the tail of the heating curve leading up to the "start" of the entry at $t = 0$ (i.e. the conditions of Table 3-4) is taken into account but not shown in the figure.

Figure 3-8 shows the acceleration experienced by the vehicle in the body-frame z-axis, a good measure of structural "wing load". As expected for entries with high lift, the loading is relatively benign with a maximum under one earth gravity.

A more complete data set for this trajectory can be found in Appendix C.

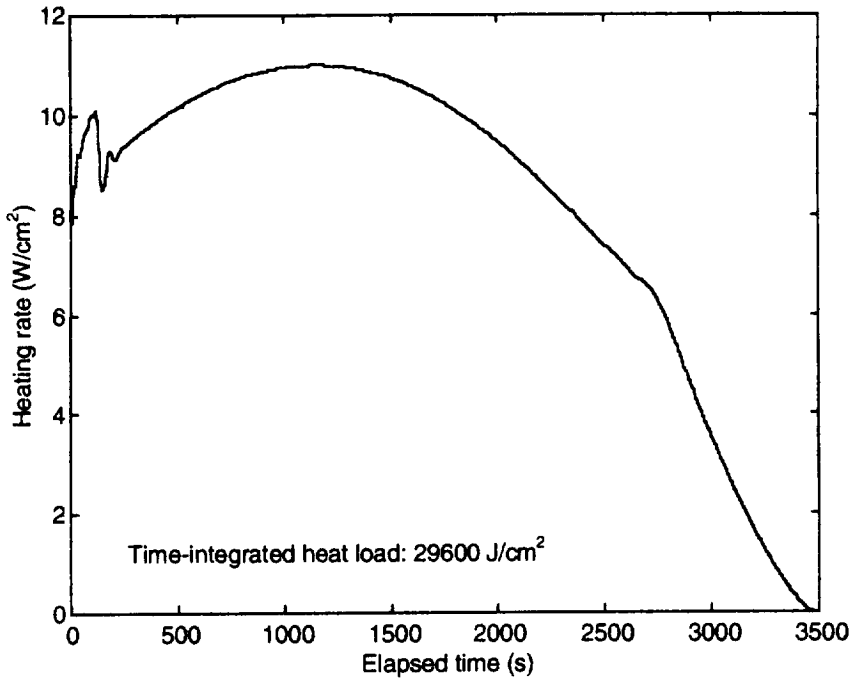

Figure 3-7: Aft-body heating rate

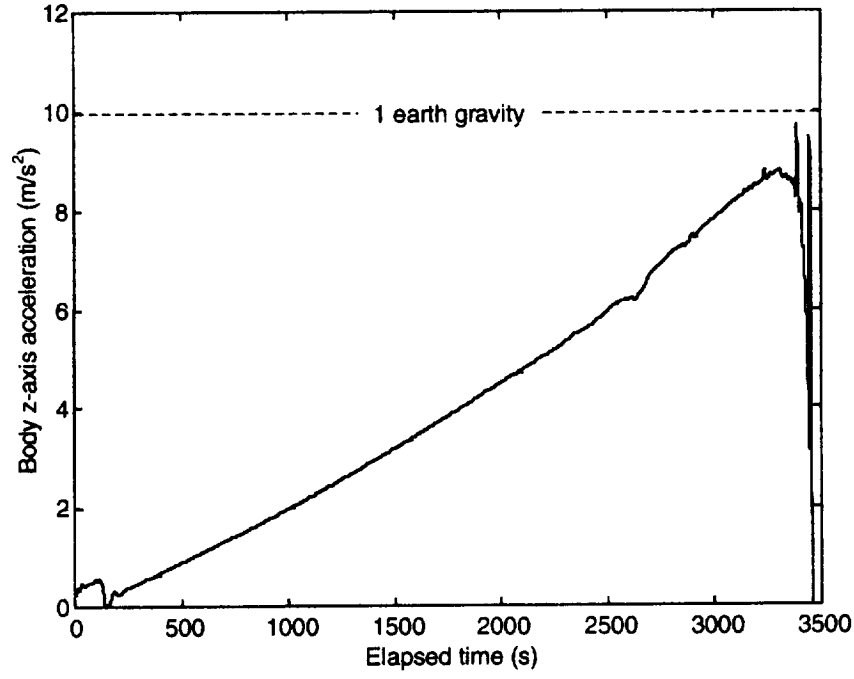

Figure 3-8: Body z-axis acceleration

3.3.1.2 Low L/D Entry

The second entry, with the highest possible drag subject to the entry profile constraint, corresponds to an entry with a fixed, high angle of attack and modulation of the roll angle ϕ to follow the constraint. This results in an entry of relatively short duration with lower integrated heat load for the TPS. In the simulation, α was held at 20 degrees, about four times greater than the value for maximum L/D and the maximum permissible within the aerodynamic database. Roll angle was controlled in closed loop by using the altitude deviation from the constraint as an error signal. As before, a PID controller was used to produce an acceptably small deviation from the constraint without excessive oscillations.

Figure 3-9 shows the resulting entry profile, with a slightly modified pullout segment to accommodate the high drag configuration. Tick marks at one-minute intervals indicate that this entry is eight times faster than before, at less than seven minutes from start down to Mach 2.

Figure 3-10 shows the altitude error, small enough throughout to consider the entry data an accurate representation of a quick entry along the constraint.

Figure 3-11 is a plot of the time variation of the roll angle ϕ. The APC segment is flown with slightly less than 90 degrees roll to provide enough of a lift component. When the vehicle transitions to constant dynamic pressure flight, the roll angle becomes inverted (lift vector down) so that lower altitudes and higher air densities can be reached fast enough to counteract the drag-induced rapid deceleration.

Figure 3-12 shows the aft-body-heating rate at the same location as in the previous trajectory. As expected the time-integrated heat load of 10500 joules per square centimeter is lower than for the previous entry, despite the much higher heating rate that results from high-α flight. As before the heat accumulated prior to $t = 0$ is taken into account, for a fair comparison.

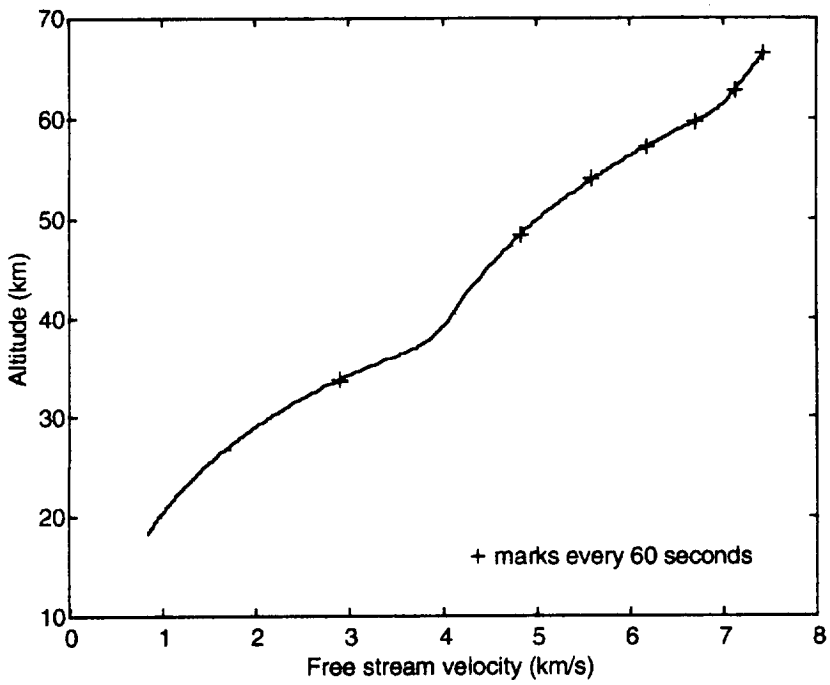

Figure 3-9: Entry profile

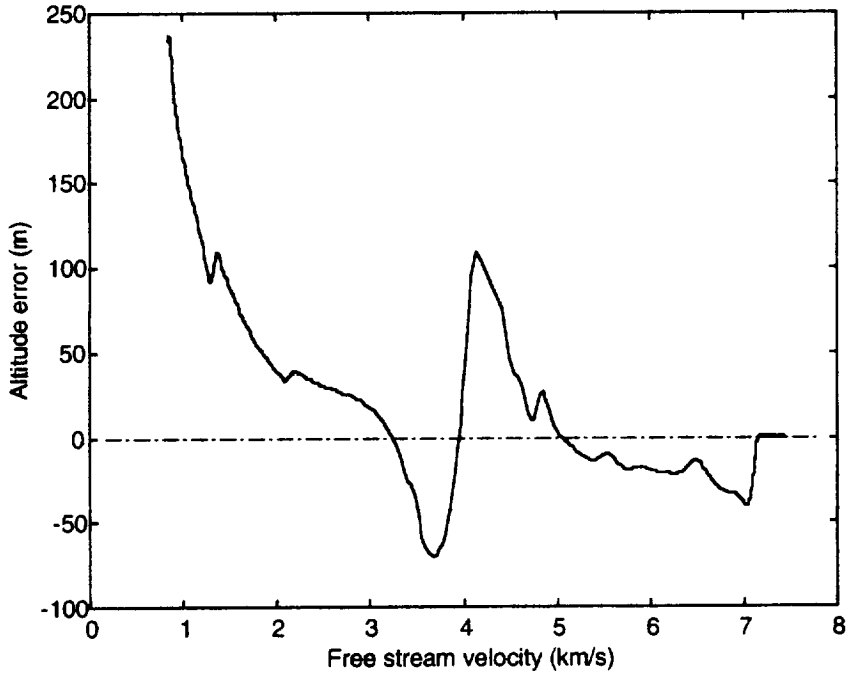

Figure 3-10: Altitude error

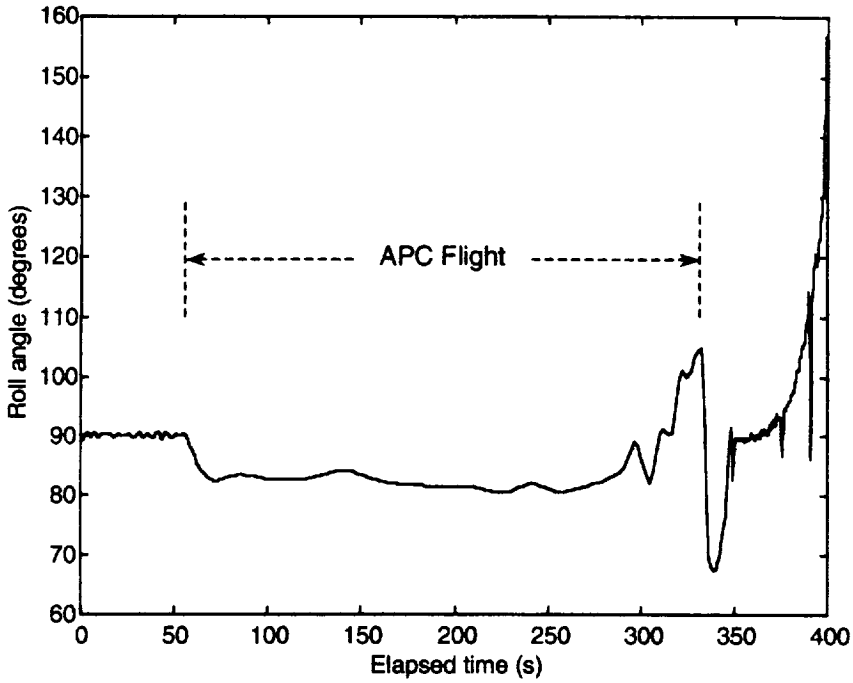

Figure 3-11: Roll angle profile

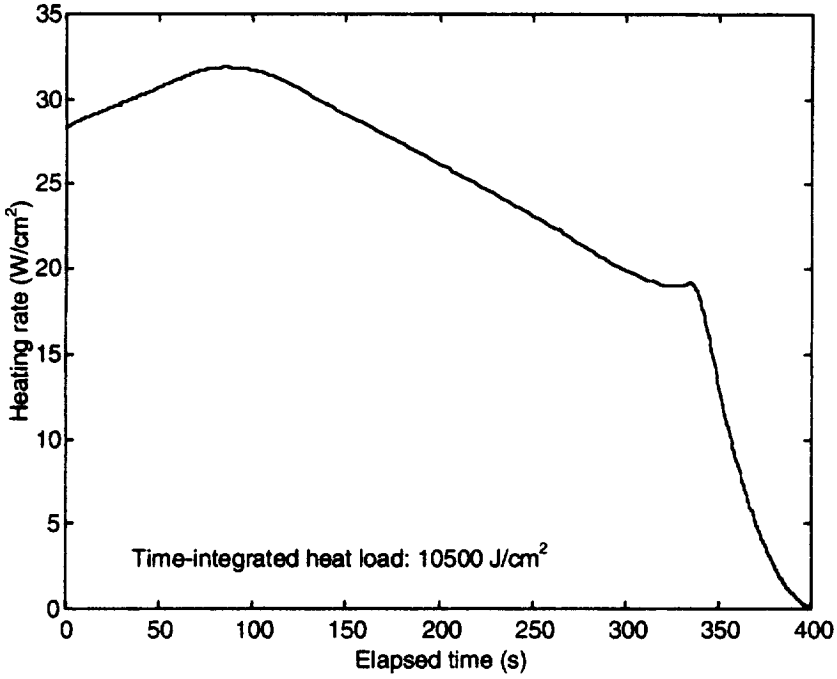

Figure 3-12: Aft-body heating rate

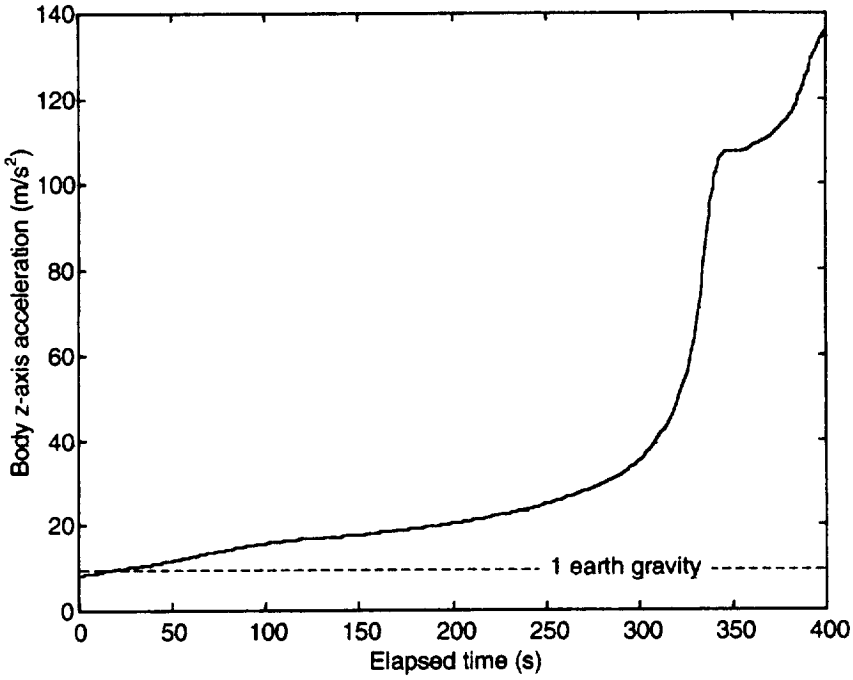

Figure 3-13: Body z-axis acceleration

Figure 3-13 shows the acceleration experienced by the vehicle in the body-frame z-axis, as before. The structural loads that the vehicle must withstand are much higher in this case, reaching up to fourteen times earth gravity. This would be a significant factor in structural design.

The ground track during this entry turns almost a full circle, since no attempt at Shuttle-like roll reversal maneuvers was made to keep the ground track straight.

More detailed data for this trajectory can be found in Appendix C.

3.3.1.3 Trajectory Comparison and Discussion

The two trajectories described above establish the limits of the trajectory design space for the SHARP lifting entry flight test, subject to the desired constraint in velocity-altitude coordinates. To summarize and discuss their characteristics, it is useful to extract from the data a few key metrics that succinctly describe each extreme. The chosen metrics are:

- Total time of entry, from the entry interface at 66 km altitude down to Mach 2
- Integrated heat load in the middle of the windward side of the wedge aft-body
- Maximum heating rate in the middle of the windward side of the wedge aft-body
- Time spent on the APC, a good measure of the integrated heat load incurred by the sharp leading edge (the heating calculation is not amenable to the same modeling assumptions as for the aft-body)
- Range, the integrated length of the path of the vehicle projected on the surface of the earth, without regard for vehicle heading.
- Maximum body z-axis acceleration, a measure of structural loading

The comparison in each metric is given in Table 3-5.

Trajectory Type	**High L/D (3.3.1.1)**	**Low L/D (3.3.1.2)**
Total time of entry	57 minutes	7 minutes
Aft-body total heat load	29600 J/cm^2	10500 J/cm^2
Aft-body max. heat rate	11 W/cm^2	32 W/cm^2
Time spent on APC	45 minutes	5 minutes
Range	18500 km	2200 km
Maximum Z-Acceleration	11.5 m/s^2	135 m/s^2

Table 3-5: Trajectory comparison

The trajectory to be chosen for the SHARP lifting entry flight will fall somewhere between these two extremes, according to the multi-disciplinary optimization to be performed as the conceptual design of the vehicle advances. As the design matures sufficient quantitative information will be available to construct an objective function for the purposes of optimization. The significant differences between the two trajectories already suggest that the choice of trajectory will have a large impact on the design of the structure and the thermal protection system.

To illustrate this impact from the point of view of aft-body thermal protection systems, a TPS selection chart by Anderson and Swann [Anderson 1960] is used to interpret the heating figures obtained for each of the two trajectories. Based on the values of maximum heating rate and total heat load at the location of interest, the chart is used to select the type of TPS material best applied to that location and to estimate the area weight of the TPS. It is important to remember that the heating calculations in this case apply not to the ceramic leading edge discussed before, but rather to a point midway along the body of the SHARP vehicle on the windward surface.

The thermal data from Figures 3-7 and 3-12 (aft-body heating rate) are plotted on the chart in Figure 3-14 to aid in the choice of TPS at the location of interest. For the high L/D trajectory, with its lower heating rates but higher integrated heat load, a Superalloy shield is sufficient. In contrast, for the low L/D trajectory, with its higher heating rates but shorter duration, a refractory metal TPS is appropriate.

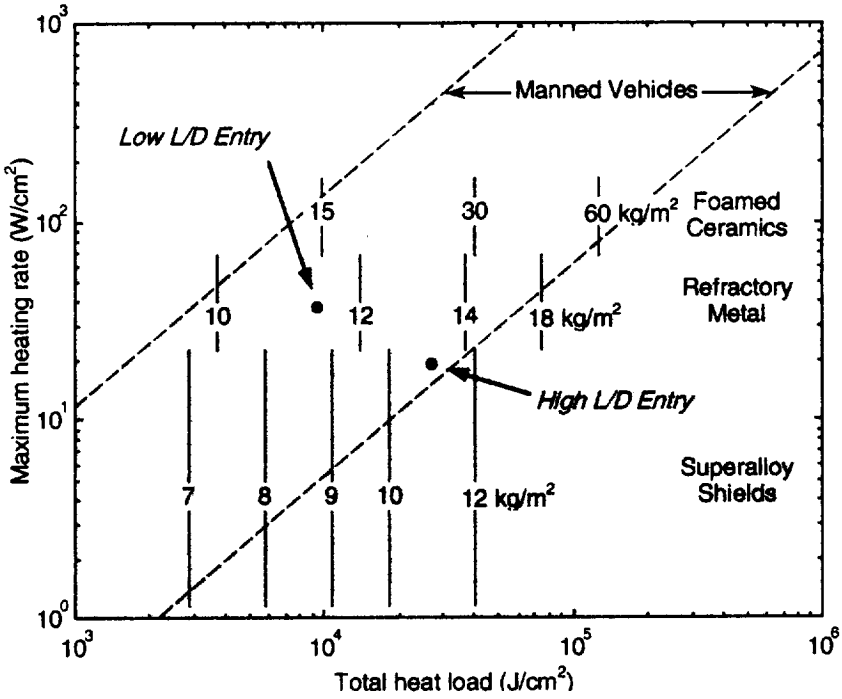

Figure 3-14: Radiative TPS summary (Anderson and Swann)

In both cases the estimated area weight of the TPS is 11 kg/m^2. The diagonal band drawn in Figure 3-14 shows the domain of application for manned entry vehicle trajectories.

While the chart dates from 1960 and TPS materials have evolved in the last four decades, and while the thermal data calculated in the trajectory simulations is approximate, the exercise just described shows that the trajectory design is tightly coupled with the vehicle design.

3.3.2 Effect of Vehicle Mass on Entry Parameters

In section 3.3.1, the mass of the SHARP vehicle was assumed to be 113 kg (250 lb.). This assumption is now relaxed and the effects of varying the vehicle mass are explored, subject to the same entry constraint originally shown in Figure 3-2. The method of control to fly along the constraint is the same as for the high L/D entry with zero roll angle of section 3.3.1.1.

In general reducing the mass of the vehicle means less angle of attack is necessary to produce the lift required for staying on the constraint, especially during the segment of flight along the APC. This has several important implications. First, limiting the angle of attack to be less than the half-angle of the wedge shape means the top surface of the vehicle will always be exposed to the flow. This allows aerodynamic control surfaces on the top surface of the vehicle (placed there because heating is less) to maintain their control effectiveness throughout the entry, avoiding operation in the low-pressure area created in the flow "shadow" of the vehicle. Second, the heating rate experienced by the windward facing surface of the vehicle decreases approximately linearly with angle of attack for a given flight condition. Finally, reducing the mass of the vehicle shortens the total time required to perform the entry because less kinetic energy must be dissipated. This in turn reduces total integrated heat load and TPS mass.

3.3.2.1 SHARP Vehicle

The SHARP vehicle (0.7 m^2 planform area) was simulated in the same entry as in section 3.3.1.1 with a mass ranging from 68 kg to 181 kg, encompassing a comfortably wide range of values around the 113 kg mass assumed in previous and subsequent simulations.

Figure 3-15 shows the effect of vehicle mass on the angle of attack profile. For lower masses the maximum angle of attack is reduced and the entry time is shortened. For

identification of the features of the profile, compare with Figure 3-5. The data in Figure 3-15 has been smoothed to remove oscillations that occur at pullout, due to controller limitations.

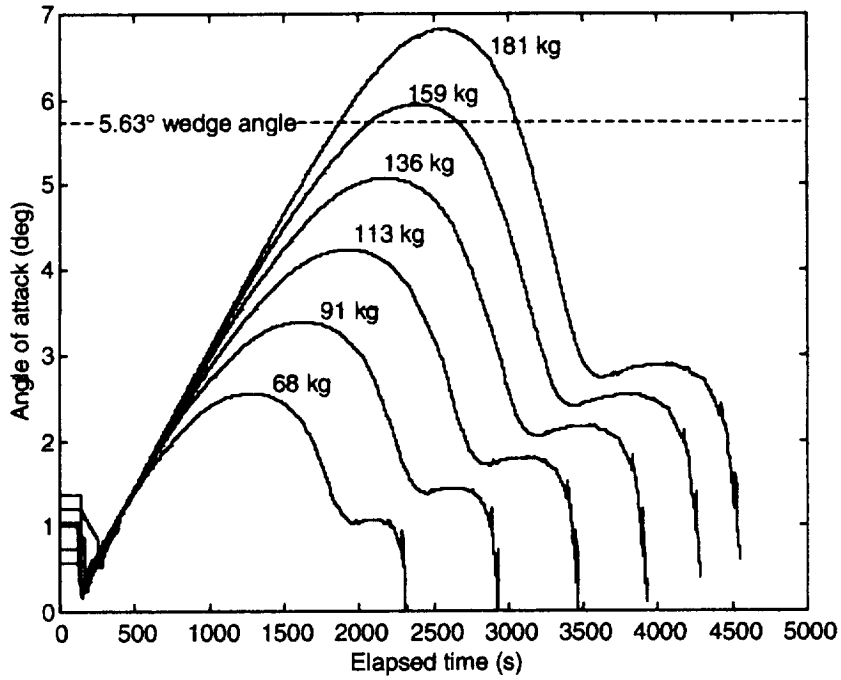

Figure 3-15: Effect of vehicle mass on AOA profile

Figure 3-16 shows the effect of vehicle mass on the aft-body heating rate profile. For lower masses the heating is reduced. The data in the first few seconds of the curves has been smoothed to remove the oscillations caused by the pullout maneuver. For purposes of calculating the total integrated heat load, the tail of the curves leading up to the "start" of the entry at $t = 0$ (i.e. the conditions of Table 3-4) is taken into account but not shown in the figure. Results are shown in Table 3-6.

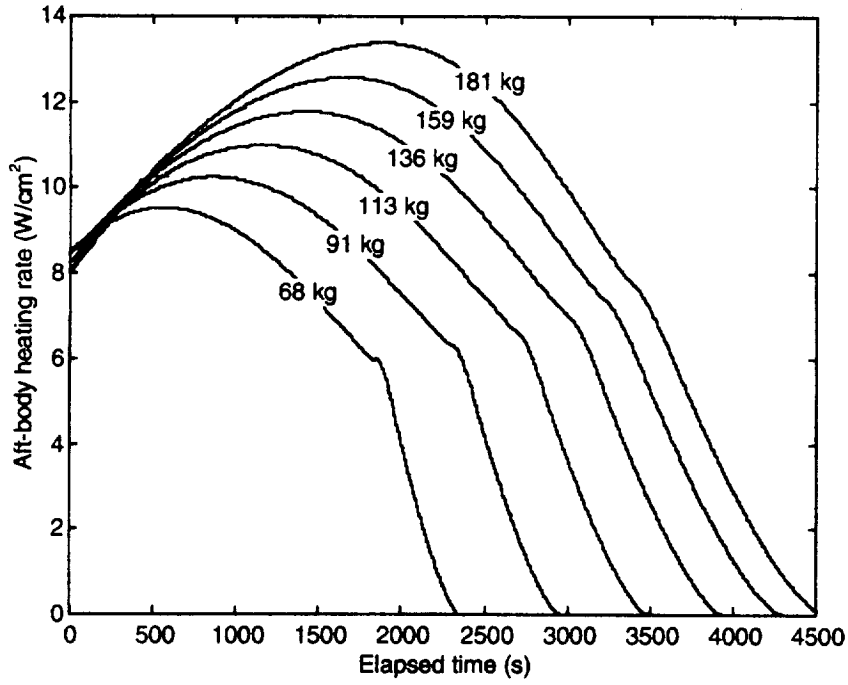

Figure 3-16: Effect of vehicle mass on aft body heating

3.3.2.2 Scaled-up Vehicles

The SHARP vehicle can be scaled up to gain a rough idea of the characteristics of full-size vehicles. Several aerodynamic effects (skin friction, boundary layer transition, etc.) make it incorrect to directly apply the SHARP aerodynamic data to a larger vehicle, but approximate results are still possible.

When scaling up a vehicle at constant density, the planform area does not rise as fast as volume and mass. The aerodynamic surface loading thus increases with vehicle size. The SHARP vehicle has a surface load of 160 kg/m^2 (assuming 113 kg vehicle mass), which is rather low in comparison to typical RLV surface loads. Additional simulation runs were made with surface loads up to and above 400 kg/m^2, close to the value for the Space Shuttle. The results are shown in Table 3-6. Note that the aft-body heating figures are not scaled up, but correspond to a point on the windward facing side of the vehicle 85 centimeters downstream from the leading edge.

3.3.2.3 Trajectory Comparison and Discussion

Table 3-6 summarizes the results from the two previous sections.

The time spent on the APC and the total heat load can be reduced from the values in Table 3-6 through some combination of banking maneuvers, following Space Shuttle practice [STS 1998]. However, this has the drawback of increasing the maximum aft-body heating rate since more angle of attack is needed to produce the same component of lift to oppose gravity.

It is clear that a light surface loading is favorable in most categories. Even for Shuttle-like surface loading, the maximum angle of attack required to stay above the APC is about 10 degrees or roughly twice that when the vehicle is banked by 60 degrees. This compares favorably with the 40-degree angle of attack practiced by the Space Shuttle orbiter and demonstrates the significant advantage of the sharp leading edge.

Vehicle Mass *(kg)*	**68**	**91**	**113**	**136**	**158**	**181**	**272**	**568**
Area loading (kg/m^2)	97	129	162	194	226	259	388	808
Total time of entry *(s)*	2330	2950	3480	3930	4290	4550	5230	5680
Time spent on APC *(s)*	1750	2200	2470	2800	3030	3160	3500	4000
Max. aft-body heating (W/cm^2)	9.53	10.2	11.0	11.8	12.6	13.4	16.4	24.2
Total aft-body heat (J/cm^2)	18100	24000	29600	35100	39900	44100	57700	81700
Max. AOA *(deg)*	2.55	3.39	4.24	5.08	5.95	6.81	10.0	18.6
Range *(km)*	12400	15600	18500	20800	22700	24100	27900	31700

Table 3-6: Trajectory comparison

3.3.3 Entry with High Cross Range

The SHARP vehicle can fly entries with very high cross range, as compared to current reusable launch vehicles. (The Space Shuttle has flown a maximum cross range of 1465 km [STS 1998]). To demonstrate this and quantify the maximum cross range possible with this geometry, an entry is performed at maximum L/D with an optimal roll angle. Shkadov et al. [Shkadov 1975] developed an expression for the optimum roll angle to achieve maximum lateral range, given in degrees by

$$\phi_{opt} = 45\left(1 + \frac{(L/D)^2}{3.6(L/D)^2 + 20.66}\right)$$

This roll angle is used until the vehicle achieves a northward ground track, at which time the roll angle is set to zero to continue northward and finish as close as possible to the pole.

To achieve maximum lateral range, the angle of attack is controlled for maximum L/D unless other constraints interfere. These constraints are the APC and an altitude ceiling. At the very beginning of the entry, the vehicle skips out of the atmosphere if α is maintained at maximum L/D. To avoid this, α must be temporarily reduced to fly at constant altitude until the vehicle slows enough that it will not skip when α is set for maximum L/D. Similarly, α must be temporarily increased when the vehicle approaches the APC, in order to avoid crossing under it.

The various control modes for α and ϕ are patched together manually for this entry, and the clearest way to describe the entry is chronological. From the entry interface until t = 350, the vehicle is flown at maximum L/D and left bank. A lookup table constructed from the NASA aerodynamic data gives the optimal α for maximum L/D at a given flight condition (Mach number and dynamic pressure). At t = 350, angle of attack control is switched to a constant altitude PID controller. This controller sets the angle of attack negative from t = 350 to t = 990, and the vehicle is banked right during this period in order to keep the trajectory deflected to the left of the de-orbit ground track. At t = 990 the vehicle is banked left once again as the angle of attack becomes positive. At t = 1820,

the constant-altitude flight ends and the maximum L/D controller takes over. The vehicle flies at maximum L/D until it meets the APC at t = 3500. The previously developed PID controller is used to follow the APC until t = 4230, when flight at maximum L/D resumes. At t = 4520, the vehicle achieves a northward ground track (perpendicular to the eastward de-orbit ground track) and the left bank is zeroed out, and the entry continues at maximum L/D until the vehicle slows below Mach 2 at t = 5600.

The entry is performed without regard for total integrated heat load. As it lasts even longer than the high L/D entry detailed in section 3.3.1.1, TPS limitations could make this type of trajectory infeasible, but even so the theoretical lateral range performance of the vehicle is of interest.

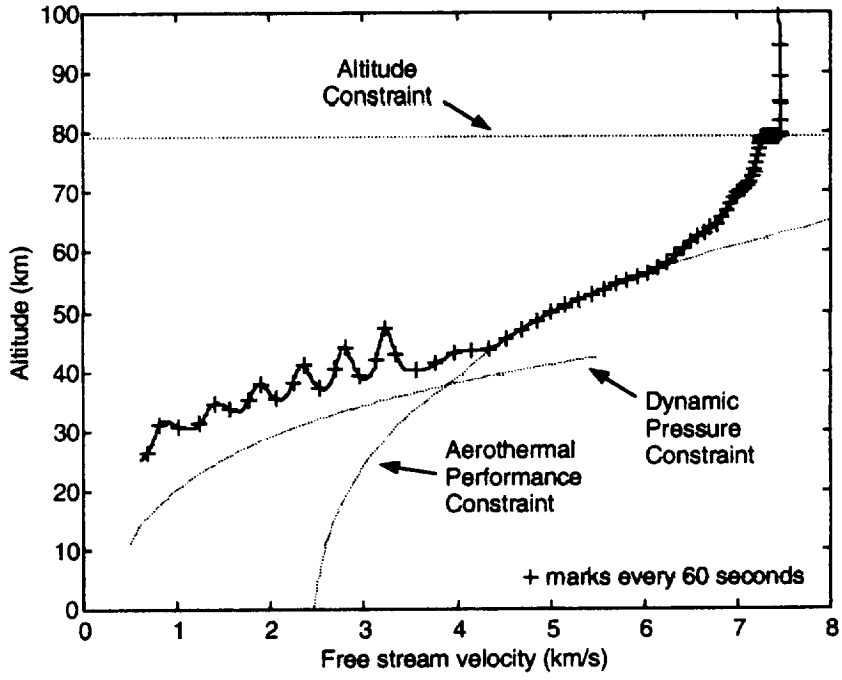

Figure 3-17: Entry profile

Figure 3-17 shows the resulting entry profile in velocity-altitude space. The large oscillations are manifestations of the phugoid mode, a slow and periodic exchange between the vehicle's potential and kinetic energies that is natural to the motion of any aircraft. This oscillation, triggered in this case by the end of banked flight at t = 4520, can be damped with an appropriate controller acting on the aerodynamic angles, but this

is not attempted here as it does not interfere with the principal features of the entry. The trajectory follows the APC for a relatively short period of 12 minutes.

Figure 3-18 shows the Earth-referenced ground path of the vehicle, which sweeps a broad arc from an equatorial start to a finish at 55 degrees latitude north. This is the most graphic representation of the theoretical cross-range capability of the vehicle, which can be seen to be approximately 6100 km. This value is a lower bound, since the simulation ends at an altitude above 25 km and a velocity of 600 m/s, giving the vehicle enough energy to glide somewhat further.

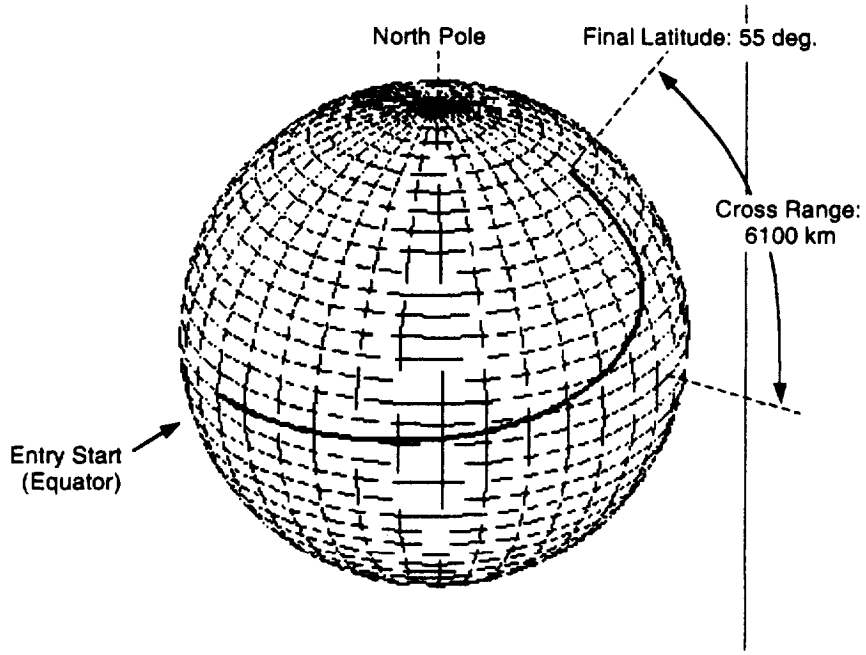

Figure 3-18: Earth-referenced ground path

The angle of attack profile in Figure 3-19 most clearly shows the different segments of the entry. After a short segment of maximum L/D flight, α is drastically reduced and slowly ramped back up to maintain constant altitude as the vehicle slows enough so it does not skip out of the atmosphere. In the next segment the vehicle is flown at maximum L/D. In the third segment, α is increased to follow the APC. The PID controller used to fly this segment causes a spike in the transition from maximum L/D flight and gives a noisy signal, but this should not detract from the general shape of the

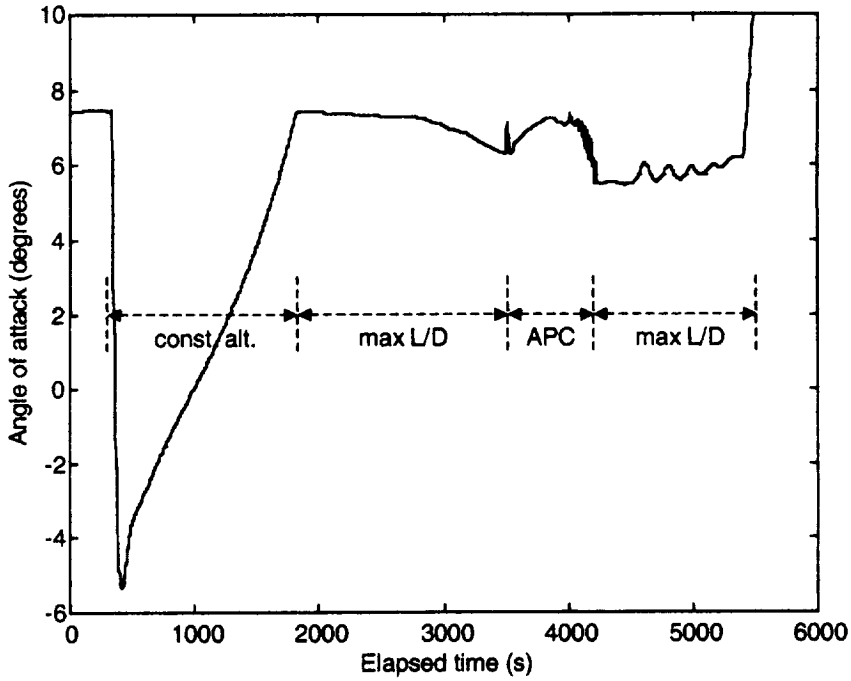

Figure 3-19: Angle of attack profile

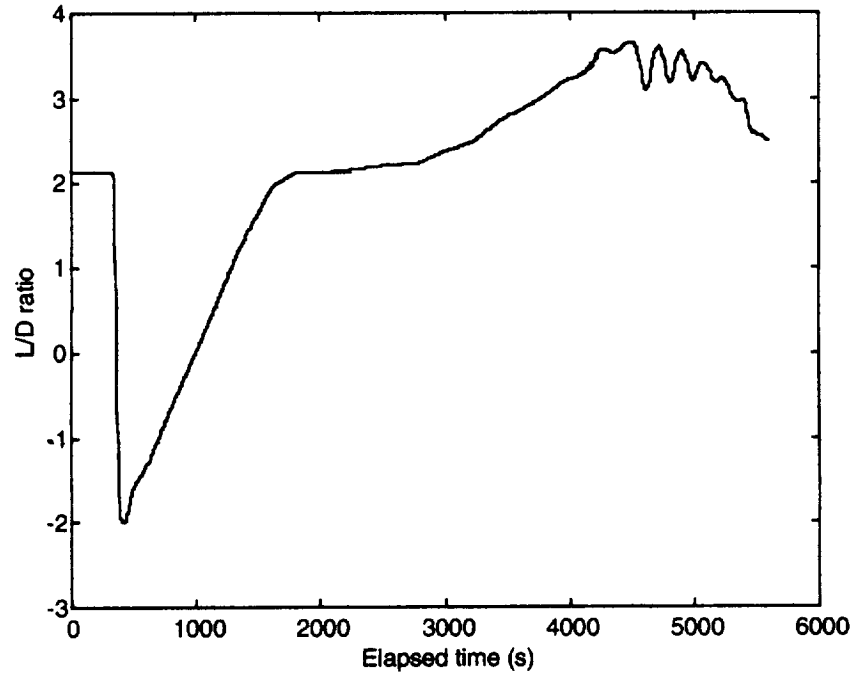

Figure 3-20: Lift-to-drag ratio

profile, which follows the APC closely as can be seen in Figure 3-17. Finally, the fourth segment is once again flown at maximum L/D, and shows small oscillations related to the phugoid motion triggered when the vehicle is leveled.

Figure 3-20 shows the L/D ratio as a function of time for the entire entry. The maximum near 4 once again highlights the aerodynamic efficiency of the sharp leading edge.

The optimization of a high cross range trajectory involves many parameters, and was performed here in a logical but improvised manner as described above. More cross range might be achievable using mildly skipping trajectories, or by doing an exhaustive numerical optimization of the parameters. In particular, the effect of vehicle mass (and hence surface loading) on the cross range performance is a worthwhile investigation. In the meantime, the entry described adequately demonstrates the cross range capability of the SHARP vehicle. Even better performance could be expected of larger vehicles, which suffer proportionately less from viscous drag effects.

A more complete data set for this entry can be found in Appendix C.

3.3.4 Entry with Ballistic Missile Launch

One early idea for the lifting flight test of the SHARP vehicle was to launch it using an Air Force Minuteman III missile, as was done for the SHARP-B01 flight experiment of May 1997 when a ballistic nose tip was tested. It was hoped that the high L/D of the vehicle would permit a pullout maneuver from the steep ballistic entry trajectory of the missile. Using representative parameters for a Minuteman entry trajectory, the simulator was used to determine whether the vehicle could transition from the ballistic trajectory to a lifting trajectory, without crossing under the APC.

As seen in Figure 3-21, this is not feasible. The figure shows the trajectory of the vehicle as it pulls out using a 20-degree angle of attack, generating the most possible lift. The vehicle goes far below the APC and pulls out just fifteen seconds after the start of the simulation. This trajectory would destroy the TPS and immediately rules out a ballistic missile launch for the SHARP lifting entry mission.

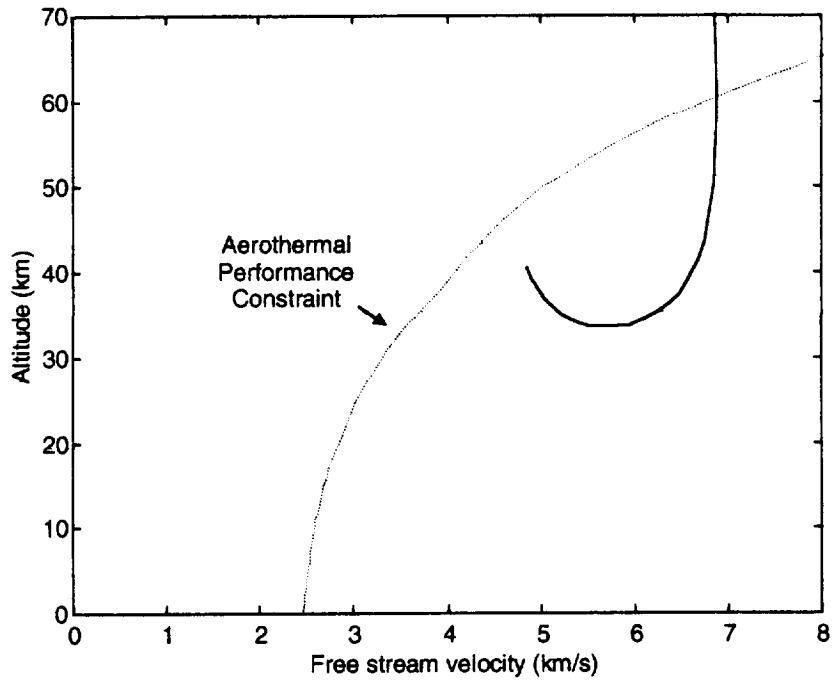

Figure 3-21: Pullout from ballistic trajectory

3.4 Summary

The trajectory simulator used NASA aerodynamic data to provide insights into the trajectory design space for the SHARP mission. The simulator determined the aerodynamic angle profiles required for achieving the primary mission, to enter along the aerothermal performance constraint. Full parameter histories for high lift and low lift entries were computed and interpreted in the context of TPS tradeoffs. The effect of vehicle mass on key trajectory parameters was investigated. The theoretical cross range capability of the SHARP vehicle was established. The ballistic launch system used in the SHARP B-01 was eliminated from consideration for the lifting entry flight test. The trajectory simulator can be used to investigate trajectory performance for any desired entry profile; flexible model inputs (vehicle mass, aerodynamics, initial conditions, planetary properties, atmospheric properties, etc.) give it the desired flexibility.

CHAPTER 4: ENTRY SIMULATION, 6-DOF

The six-degree of freedom simulator described in this chapter builds on the trajectory simulator from Chapter 3 by modeling the attitude dynamics of the vehicle. A Newtonian model of the SHARP vehicle replaces the aerodynamic database used in Chapter 3, which was originally computed by NASA using its HAVOC code. The Newtonian model is verified against the NASA data and features easily configurable control surfaces. The primary application of the 6-DOF simulator is flight control system development, but this is not seriously attempted here. Instead, simple aerodynamic flap controllers are developed and a short segment along the APC is flown, demonstrating that the 6-DOF simulator is a functioning test bed for flight control system development.

4.1 Simulator Implementation

4.1.1 Architecture

The 6-DOF simulator was built in the SIMULINK graphical environment as an extension to the trajectory simulator. Most of the components from that simulator are reused, and described in detail in Chapter 3.1 and Appendix B.

In addition to computing the forces on the vehicle to determine its motion, the torque on the vehicle is computed to determine its attitude dynamics. The attitude dynamics feed back into the force computation, for example because changing angle of attack changes the amount of lift. To simulate these three additional degrees of freedom, a mass model of the vehicle is developed in Appendix A.

The architecture of the simulator is as follows. For a given flight condition, aerodynamic forces and moments on the vehicle (i.e. lift, drag, lateral force, as well as yaw, pitch and roll moments) are calculated via a new aerodynamic model. The model used for this purpose was checked against NASA-provided aerodynamic data specific to the SHARP vehicle geometry [Kolodziej 1997]. Through a series of coordinate transformations the forces and moments experienced by the vehicle are computed, and the equations of motion are advanced in the inertial frame. The overall cycle is depicted in Figure 4-1.

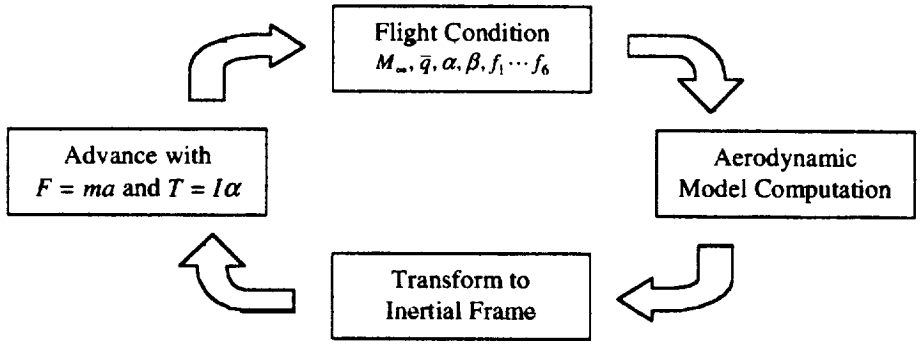

Figure 4-1: Simulator architecture

4.1.2 Modeling Details

The NASA-provided aerodynamic database for the SHARP vehicle and used in Chapter 3 was a simple database limited to the pitch plane. In order to provide 6-DOF capability the aerodynamic database had to be augmented or replaced. NASA was not able to provide numerical data for motion outside of the pitch plane, and such data would still have required aerodynamic modeling for the effects of aerodynamic control surfaces.

Even if NASA had extended the aerodynamic database to include more variables, the numerical lookup and interpolation that is required at each step in the simulation quickly becomes prohibitively expensive to compute. In Chapter 3 the lookup consisted of two coefficients (C_L and C_D) as a function of three parameters (α, M_∞, q). In the case of the 6-DOF simulator one would have to lookup six coefficients (three for force, another three for moment) as a function of ten or more parameters (α, β, M_∞, q, and one deployment position angle for each flap). While three-dimensional lookup and interpolation is

computationally easy, ten-dimensional lookup is difficult, if not impossible, from the point of view of both storage and number of operations.

In addition, the control surface configuration of the vehicle is not decided at this time. A numerical database taking into account the effect of control surface positions would have to be recomputed entirely each time a control surface configuration change is made as the design evolves.

A further complication arises from the higher bandwidth of the simulation parameters. The model must be computed at least five to ten times faster than the pitch oscillation frequency discussed in Chapter 2 or at a rate on the order of 20 to 30 Hz. This figure is roughly two orders of magnitude faster than in the trajectory simulations of Chapter 3, and further increases the computational challenge of numerical lookup.

This motivates the development of a simplified aerodynamic model that is both quick to compute and reasonably accurate. This model is described in section 4.2.

The attitude dynamics are computed as follows: α, β, q, and one deployment angle for each flap are fed into the aerodynamic model. The model output is the aerodynamic moment as seen in the body-fixed frame. From the components of moment and the mass properties of the vehicle, the body rates are determined. From the body rates the Euler angles of the body-fixed frame with respect to the horizontal frame are determined. By comparing the Euler angles of the body with the Euler angles of the wind frame, new values of the aerodynamic angles are determined. This computation assumes the horizontal frame is inertial, which is correct to first order.

A complete and detailed description of the 6-DOF model and its usage, as well as a walk-through of each component, may be found in Appendix D.

4.2 SHARP Newtonian Aerodynamic Model

An aerodynamic model of the SHARP vehicle was constructed to replace and extend the capabilities of the NASA-provided aerodynamic database used previously. The model

uses Newtonian aerodynamics [Tauber 1996] to compute forces and moments imparted to the vehicle. Control surfaces are included in the model.

4.2.1 Geometrical Representation

For modeling purposes, the vehicle is represented as a collection of polygons that make up a wire frame drawing as shown in Figure 4-2.

Using NASA dimensional data, the vehicle is represented as a wedge with trapezoidal top and bottom faces and conical sides. The conical sides are each broken into six triangles to simplify computations by generalizing curved surfaces as a collection of flat polygons. Six control surfaces are introduced, configured as shown in Figure 4-2. They are drawn in a 20° deployed position, for geometrical clarity. The chord length of the control surfaces is variable and can be set as a fraction of the total vehicle length. This permits rapid reconfiguration of the model for different simulation runs.

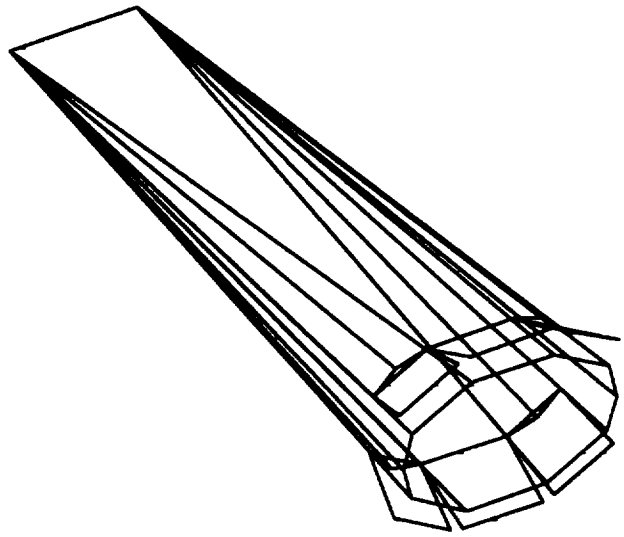

Figure 4-2: SHARP wire frame model

NASA motivated the particular choice of six trailing edge control flaps as a flexible configuration that would provide control authority in all axes. Pitch control is achieved by deploying groups of three flaps on the top and bottom of the vehicle in concert. For example, a positive steady-state angle of attack can be maintained by deploying the three flaps on the top side of the vehicle. Yaw control is achieved by deploying opposite pairs

of side flaps (paired top and bottom on each side). Roll control is achieved by deploying diagonally opposed corner flaps. Carroll [Carroll 1995] describes this type of control surface arrangement using four flaps; however, it was deemed better to design with six flaps to provide more decoupling between axes and better control authority in yaw. Flap actuation mechanisms for the real vehicle can be embedded in the body and act directly on the surface rather than apply a moment at the hinge line.

Figure 4-3 is a front view of the vehicle (compare with Figure 4-2) showing the flaps configured for the different control modes. The deployment angles shown in the figure are arbitrarily chosen for the sake of clarity. Flap commands can be blended to achieve simultaneous control of all three axes; this will be discussed later in this chapter.

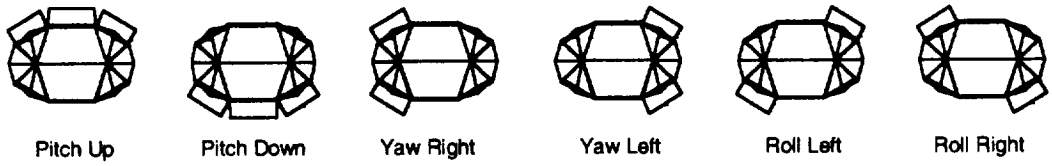

Figure 4-3: Flap control modes (front view)

4.2.2 Aerodynamic Computation

The aerodynamic force calculations are reduced to computations on three- and four-sided polygons. The resulting forces and moments are expressed in the wind frame, with the x-axis along the velocity vector and the z-axis "down" as seen in the vehicle. All that is needed for the computation is the polygon's outward pointing normal unit vector, the position vector of its centroid in the body frame, and the polygon's area.

To compute the force imparted to the polygon by the impinging flow, the pressure on the surface is calculated according to Newtonian theory. The coefficient of pressure is given as

$$C_p = 2\sin^2\delta$$

where δ is the angle between the free stream velocity vector and the plane of the polygon. This angle is computed through a product with the outward pointing normal vector of the

polygon. When δ is zero, the flow is parallel to the surface. When δ becomes negative, the flow appears to come from inside the body and through the surface. When this condition arises, on the lee side of the vehicle and as a result of a polygon being shadowed from the flow by the body, the coefficient of pressure is assumed to be zero. The component of force due to pressure acts inwards at the centroid of the polygon, with a magnitude of

$$F_N = \frac{1}{2}\rho V_\infty^2 C_p A$$

where A is the area of the polygon.

A fixed coefficient of friction C_f approximates the effects of shearing stresses within the boundary layer. The value of C_f is fixed at 0.004 in the simulation, a mid-range value as shown in Figure 9 of [Kolodziej 1998]. This coefficient of friction gives rise to a force that acts at the centroid of the polygon and along the intersection of to planes: the plane of the polygon, and the plane defined by the polygon normal vector and the free stream vector. The magnitude of this force is

$$F_P = \frac{1}{2}\rho V_\infty^2 C_f A$$

Figure 4-4 shows the forces as seen in the plane of the velocity vector and the polygon normal. The outward normal vector is n, and the position of the polygon centroid in the body frame is r, and does not necessarily lie in the plane of the figure.

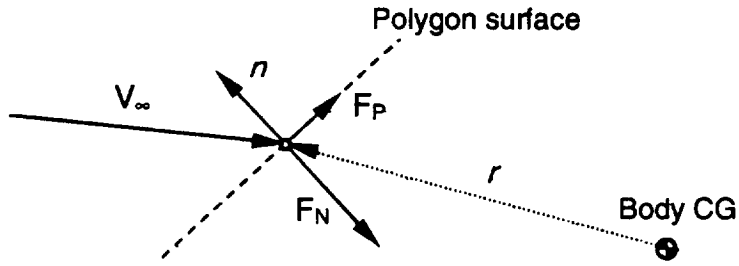

Figure 4-4: Polygon computation geometry

A sum is performed over all the polygons that describe the vehicle, to find both the total force and total torque on the vehicle. Drag due to leading edge bluntness is added after the sum, but is small due to the sharpness of the leading edge.

Control surfaces are treated like any other polygon, with the exception that the normal vector and centroid position vector (as seen in the body frame) must be recomputed with each simulation step to reflect changes in the deployment angle as the simulation progresses.

In a real situation, hypersonic control surfaces work inside the shock layer and cause complex flow effects (shock interactions, boundary layer tripping, etc.) when they are deployed. Control surface design for hypersonic vehicles is a difficult problem [Neumann 1989] and predicting the pressure distribution (and hence the force) on a control surface is not usually done well using Newtonian theory. The pressure is typically overestimated, because the vehicle's nose bluntness increases the enthalpy of the upstream flow thus reducing pressure recovery at the flap surface. In the case of SHARP this effect is less pronounced because the sharp leading edge allows flight at low angle of attack, resulting in a thin shock layer with relatively less enthalpy. The effect of a sharp leading edge on downstream pressure recovery has been investigated [Tiwari 1992] and bears out this effect. Newtonian theory is therefore a reasonable but not perfect predictor of the control surface pressures in the case of SHARP, especially if the control surface deployment is limited to small angles. The Newtonian model is considered sufficient for the purpose of a preliminary analysis of the vehicle.

A more detailed description of the model computations may be found in Appendix D.

4.2.3 Model Verification

The Newtonian model is verified against the NASA aerodynamic database by performing several tests to ensure that the Newtonian results agree reasonably closely with the NASA data. The NASA data, computed using a much more sophisticated code, includes aerodynamic flow effects not captured in the simplified Newtonian model, for example boundary layer transition. Lift, drag and pitching moment coefficients for the NASA aerodynamic data and the Newtonian model are compared. For the Newtonian model, the forces and moments resulting from the calculation are divided by dynamic pressure and the appropriate reference area so that the coefficients may be compared.

Figure 4-5 shows the comparison of lift coefficient C_L as a function of angle of attack. For both the Newtonian model and the NASA data C_L is independent of dynamic pressure. The NASA data is plotted for several Mach numbers as indicated on the figure; not surprisingly, the Newtonian model does not exhibit this Mach number dependence. Also expected, the Newtonian result agrees more closely with the NASA data as Mach number is increased. At Mach 10 C_L is under-predicted by 25 to 30%. Agreement is poor below Mach 10, or about the speed of the vehicle when the entry profile transitions from the APC to the DPC.

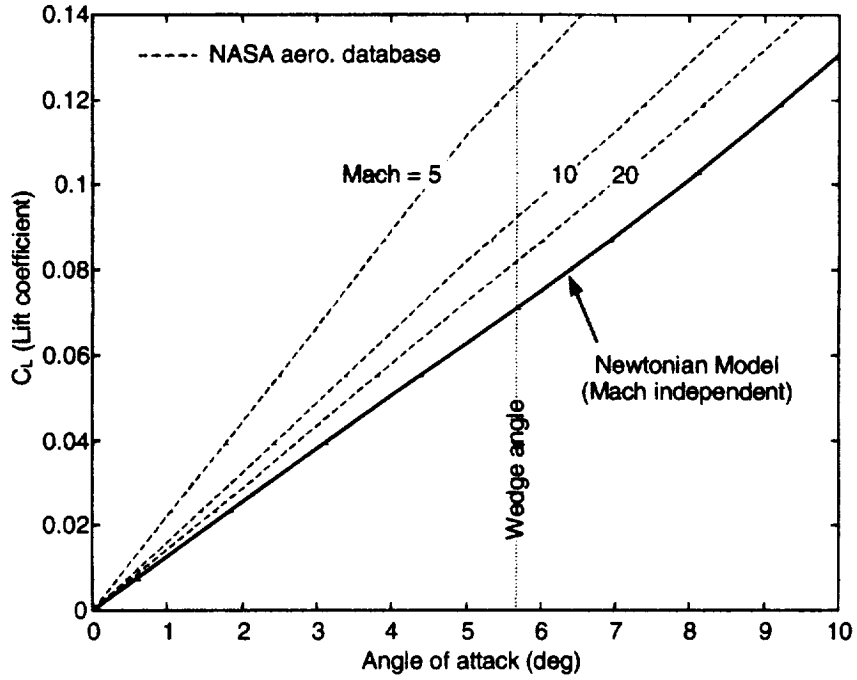

Figure 4-5: Lift coefficient comparison

Figure 4-6 shows the same comparison for the drag coefficient C_D. In this case the NASA data is dependent on both Mach number and dynamic pressure. The results are therefore plotted separately for Mach 5, 10 and 20. In each plot the NASA data is plotted at zero and 43000 N/m^2 dynamic pressure, the minimum and maximum of the flight envelope (the upper curve corresponds to zero dynamic pressure). This establishes a band within which the C_D is known to lie at the given Mach number. Agreement is generally better than for C_L and the Newtonian model follows the NASA data well above Mach 10.

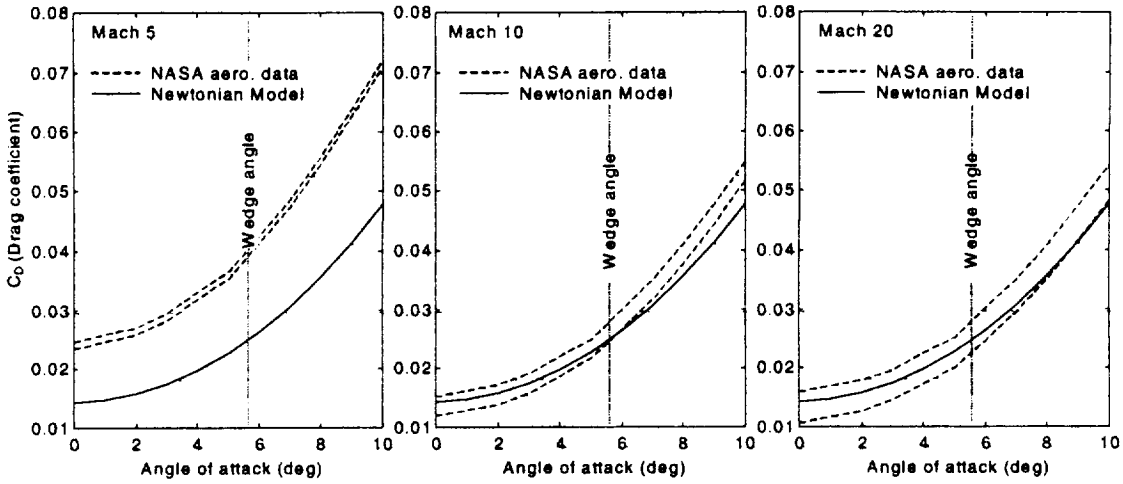

Figure 4-6: Drag coefficient comparison at Mach 5, 10 and 20

Figure 4-7 shows the comparison of pitching moment coefficient C_m. It was found that in the Newtonian model the C_m was quite sensitive to flap angle trim. To produce the data in Figure 4-7, all six flaps were deployed by two degrees, moving the center of pressure back slightly. This deployment angle corresponds to the trailing edge of the flaps moving outward by six millimeters, a small amount compared to the resolution of the wire frame model. It is believed that the gross approximation of the aft-body geometry through a relatively small number of polygons explains the requirement for a small amount of flap angle trim in order to make the pitch data agree with the NASA data, which was calculated using a finer mesh. More generally this discrepancy shows the great sensitivity of the vehicle's pitch behavior to aft body configuration: each degree of flap trim produces a 30% increase in the Newtonian model's C_m. Results are shown at Mach 5, 10 and 20 and the dynamic pressure dependence of the NASA data is shown in the same way as in Figure 4-6.

Through the comparison with the NASA aerodynamic database, the Newtonian model displays its limitations. However, at speeds above Mach 10 and angle of attack below the wedge angle all coefficients come reasonably close to the NASA data, with the worst disagreement shown in C_L. As the NASA data is insufficient to simulate lateral dynamics and the effect of flap deployments, the limitations of the Newtonian model are accepted for the purpose of conceptual design.

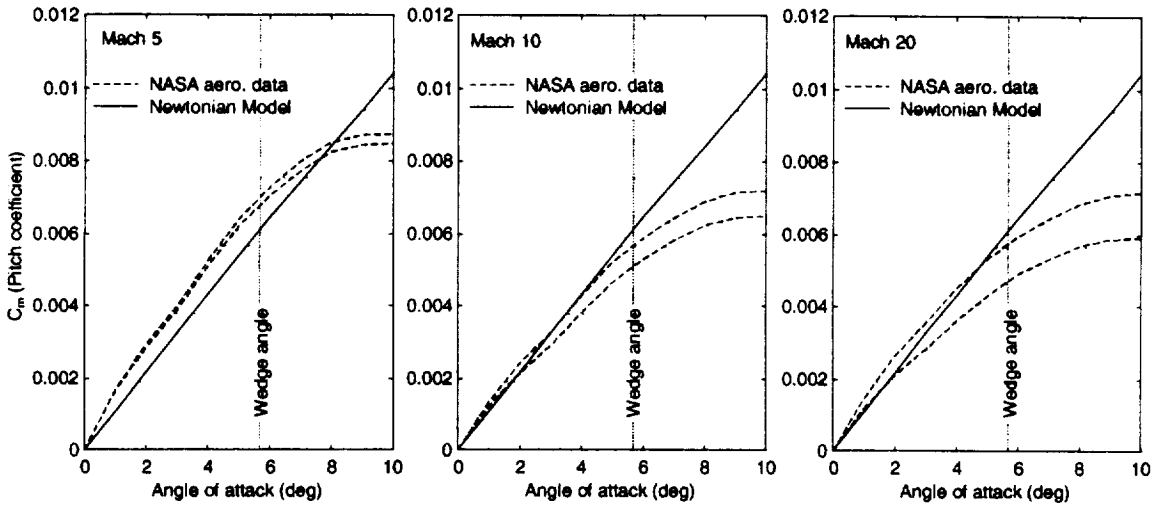

Figure 4-7: Pitch moment coefficient comparison at Mach 5, 10 and 20

4.3 Simulator Verification

For the 6-DOF simulator no convenient comparison with an established simulator (as was done in Chapter 3 for the trajectory simulator) was possible. The only verification attempted was to predict the natural pitch oscillation frequency for a given dynamic pressure and to verify if the 6-DOF simulator indeed reproduced that frequency. The pitch oscillation frequency was predicted using the method in Chapter 2. Simulation results, determined from a plot of angle of attack as a function of time, agreed quite well as shown in Figure 4-8. This agreement confirms that the attitude physics are modeled correctly. The trajectory physics remain the same as before and were verified in Chapter 3.

4.4 Simulation visualization

The results produced by the 6-DOF simulator are in the form of time histories of the desired parameters, for example angle of attack or flap position angle. This information can be plotted, but does not easily provide insight into the dynamical behavior of the vehicle, as seen in Figure 4-9. When α, β, ϕ, and the positions of the six control flaps are

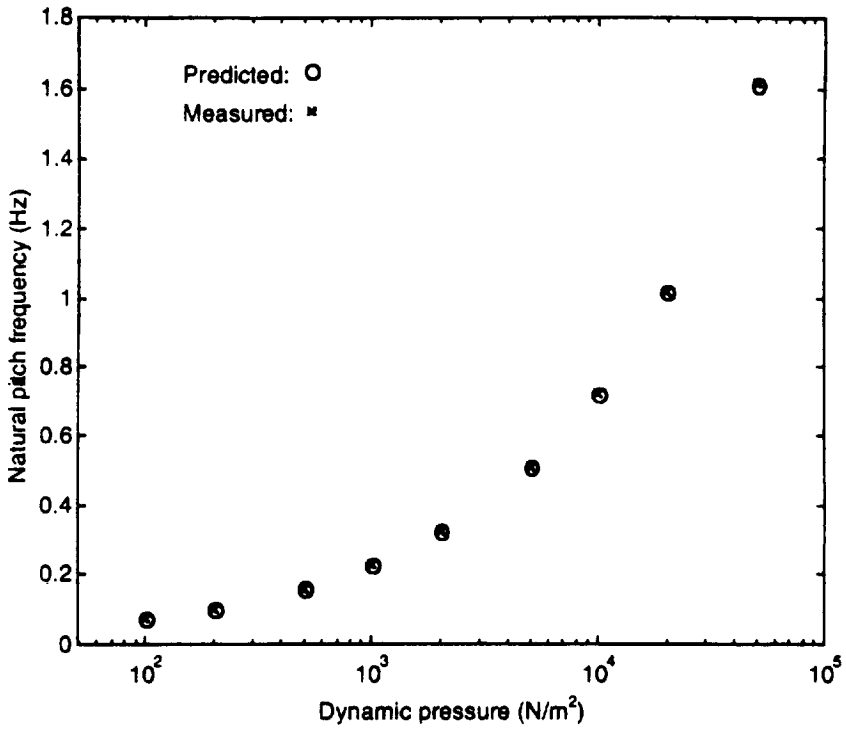

Figure 4-8: Predicted vs. measured pitch frequency

all changing with time, understanding the behavior from a number of simple two-dimensional plots is difficult. To better understand and interpret the simulation results, a visualization tool was developed in MATLAB.

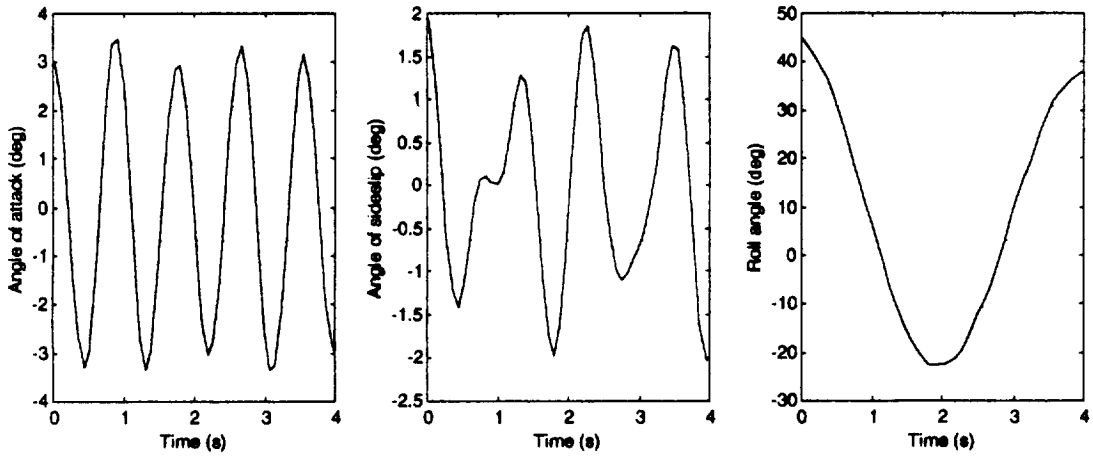

Figure 4-9: Raw simulation results

The tool displays a wire-frame drawing of the vehicle (as in Figure 4-2) and animates it. The motion of the vehicle and its control flaps is easy to see, and the viewpoint can be rotated at will. If the angles of the motion are small, an exaggeration factor can be added to make the motion more obvious. The display calculations are based on the same geometrical information underlying the Newtonian aerodynamic model, and use a series of matrix rotations to compute the orientation of the vehicle as seen in the wind frame. While an animation cannot be included here, Figure 4-10 shows how the plots of Figure 4-9 would appear using the visualization tool at three instants in time.

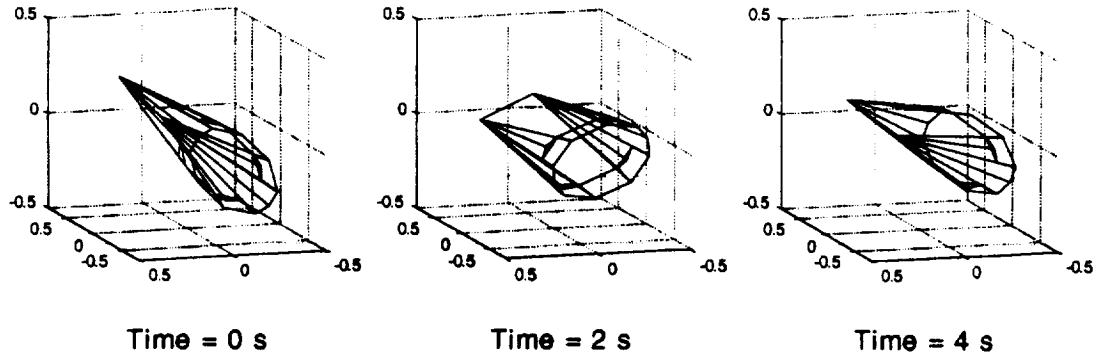

Figure 4-10: Visualization of simulation results

4.5 Simulator Applications and Results

The 6-DOF simulator combined with the Newtonian aerodynamic model for SHARP is demonstrated to be useful for control surfaces configuration and entry flight control system design.

4.5.1 Control Surface Sizing

The control surface configuration shown in Figure 4-2 (six trailing edge flaps of the same chord length) is used to investigate the effect of control flap chord length on control authority in the pitch and yaw axes. For the purpose of demonstration, this analysis must remain qualitative, as the Newtonian modeling does not capture some of the aerodynamic effects that occur at the flap surface. The values given should be considered as generous

upper bounds. Care was taken to restrict the amount of flap deployment (from the body-flush position) to less than ten degrees to avoid gross deviations from Newtonian behavior.

For different values of flap chord length (as a percentage of vehicle length), the equilibrium angle of attack of the vehicle is computed as a function of control surface deployment angle from the body-flush position. To generate a steady-state angle of attack, the three flaps located on the topside of the vehicle are deployed simultaneously as shown in Figure 4-3. The resulting angle of attack curves are shown in Figure 4-11. Not surprisingly, larger flaps require less deflection for a given desired angle of attack. The wedge angle is indicated on the figure; if this angle of attack is exceeded the top surface of the vehicle begins shading the flaps from the free stream. In this regime the Newtonian modeling breaks down.

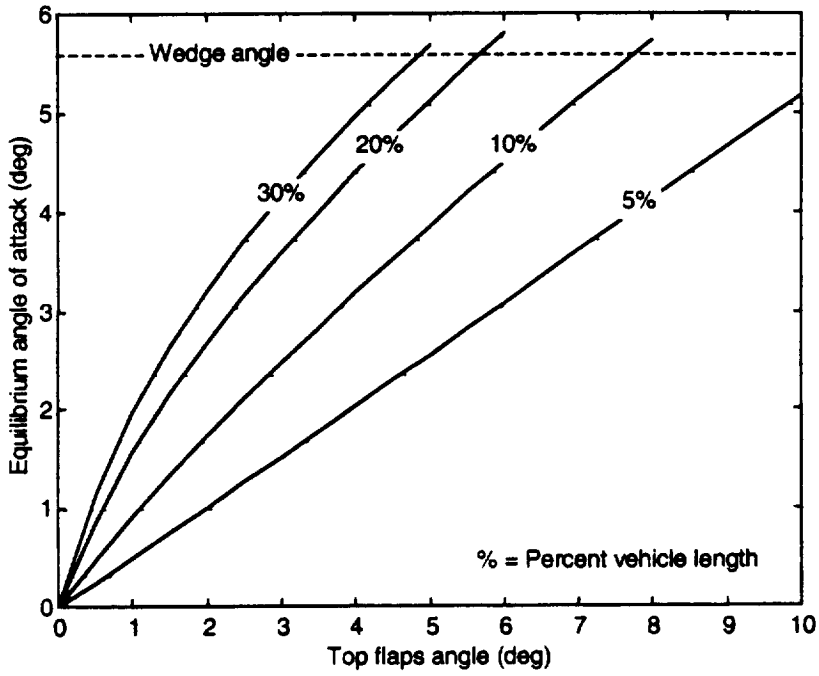

Figure 4-11: Pitch control authority

Figure 4-12 shows the results of a similar analysis in the yaw axis. In this case, the two flaps on one side of the vehicle (top and bottom) were deployed simultaneously to create a yawing moment, as shown in Figure 4-3. For different values of flap chord length (as a

percentage of vehicle length), the equilibrium angle of sideslip of the vehicle is computed as a function of control surface deployment angle from the body-flush position. The "shade angle", indicated on the figure, is the angle at which the conical side of the vehicle begins to be shaded from the free stream; however, this does not affect the control flaps.

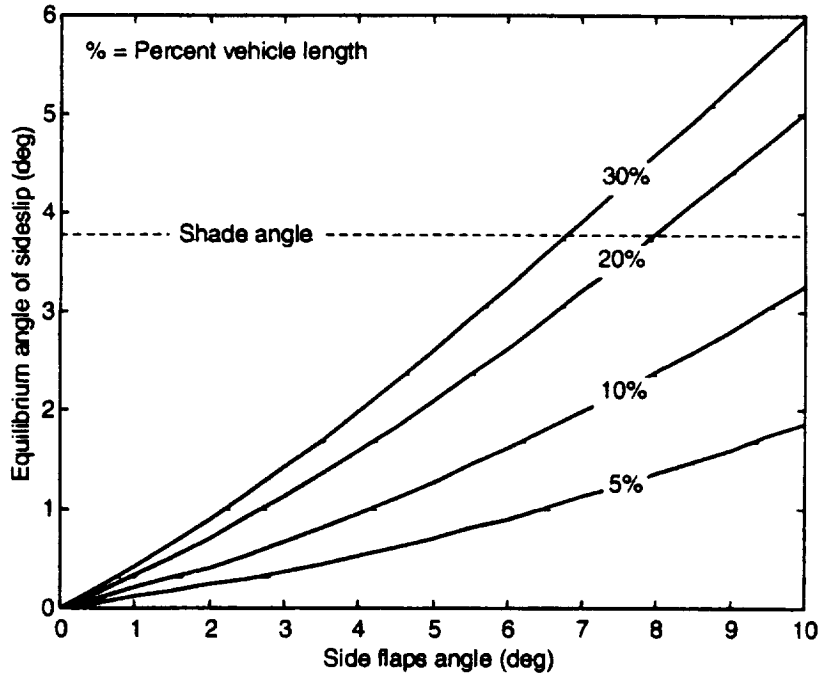

Figure 4-12: Yaw control authority

Comparing Figure 4-12 with Figure 4-11, it is clear that the control authority in yaw is not as great as that in pitch, for the particular control surface configuration chosen in the Newtonian model. This result can be explained by examining the forces acting on the control surfaces. In the pitch case, nearly the full force exerted on the flaps contributes to the pitching moment, because the flap normal vectors are almost perpendicular to the pitch axis. In the yaw case, not only are two control flaps used instead of three but their normal vectors are mostly parallel to the yaw axis so that the moment generated about that axis is not as great.

This effect could be countered by changing the placement, number, or relative sizing of the flaps. To increase yaw control authority additional flaps could be placed on the sides of the vehicle, or the outboard flaps in Figure 4-2 could be moved further onto the sides

of the vehicle. Possibly the best solution would be to make the outboard flaps slightly larger than the top and bottom flaps, with associated benefits in roll control authority.

Roll control (achieved through the simultaneous deployment of diagonally opposed control flaps, as shown in Figure 4-3) was not found to be a problem in simulations. Indeed, there is no restoring moment in the roll axis as there is in pitch and yaw. This, combined with the relatively small roll moment of inertia, causes the vehicle to accelerate rapidly into a spin about the roll axis when the flaps are positioned accordingly.

Alternate control surface configurations were not investigated, but the modular design of the Newtonian model of SHARP would make any changes easy to implement. To improve on this investigation a better hypersonic flap model would be necessary.

4.5.2 Aerodynamic Angle Control

Flight control system development is another application of the 6-DOF simulator. Developing the flight control system for a lifting entry vehicle is a difficult task that would take many man-months of labor. The 6-DOF simulator is demonstrated to be useful for this task with a short segment of flight along the APC using a very simple example controller.

4.5.2.1 Controller Details

The controller assumes perfect state knowledge (altitude, velocity, aerodynamic angles) and operates the six control surfaces so as to follow the APC. First, taking the difference between the current altitude and the altitude corresponding to the APC results in an error signal. From this altitude error signal a PID controller determines the commanded angle of attack; this controller was reused directly from section 3.3.1.1. Sideslip and roll angles are commanded to fixed values. For each of α, β and ϕ, an error signal is produced from the difference of the commanded angle and the actual angle. These three error signals are fed into three separate PID controllers, each of which determines a commanded angle for the six control surfaces. The three resulting control surface command signals are blended by simple addition. The actuator dynamics for individual control surfaces are not modeled; however, the control surface deployment angles are constrained between zero

and 10° with a maximum rate of 10 degrees per second. The final control surface angle signal is fed into the aerodynamic model. The overall architecture of the angle of attack controller is shown in Figure 4-13. A fast inner feedback loop controls angle of attack while a slower outer feedback loop controls altitude. The controllers for angle of sideslip and roll angle are similar.

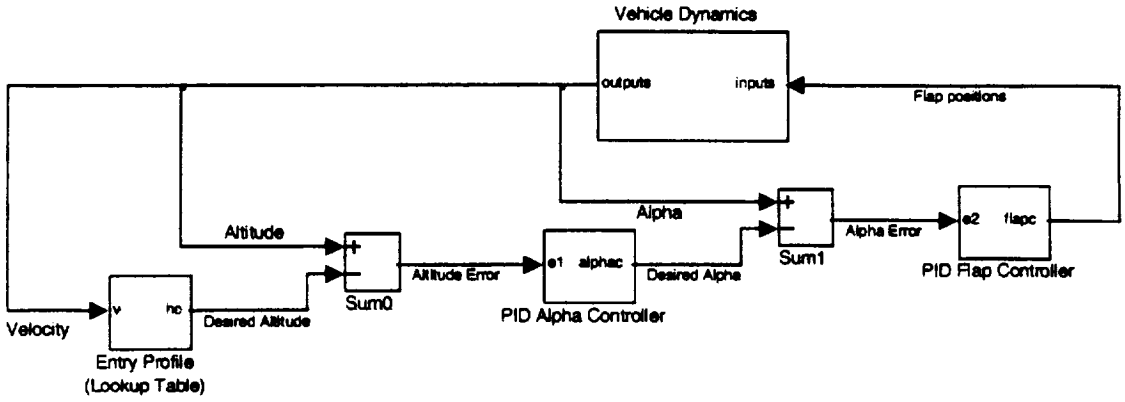

Figure 4-13: Controller architecture

The control surface controller gains were determined manually, and thus subjectively, by tuning the step response until adequate characteristics (rise time, overshoot, settling time) were observed. Since the vehicle responds very differently depending on the dynamic pressure, the tuning process was repeated at low and high dynamic pressures. Overall controller gain was then adjusted based on a linear interpolation of the dynamic pressure value. This process did not produce a good controller–such was never the intent. However, the example controller allows a full end-to-end demonstration of the application of the 6-DOF simulator, namely solving for the motion of the vehicle given an aerodynamic model and a flight control system model.

4.5.2.2 Demonstration Results

For this demonstration the goal is to show the end-to-end capability of the 6-DOF simulator by flying along the APC. Since the controller design is not refined, the trajectory initial conditions are chosen close to the APC. The resulting trajectory data is shown in the plots below. The entry segment lasts 20 minutes, before the angle of attack controller experiences instability. While a full entry demonstration (along the APC and down to Mach 10 where the aerodynamic model breaks down) would have been more

impressive, the demonstration is still successful. The reader is once again reminded that the aim was not to measure or prove controller performance.

Figure 4-14 shows the entry profile in velocity-altitude coordinates. The entry segment lasts 1200 seconds and slows the vehicle from Mach 25 to Mach 22. Tick marks indicate one-minute intervals.

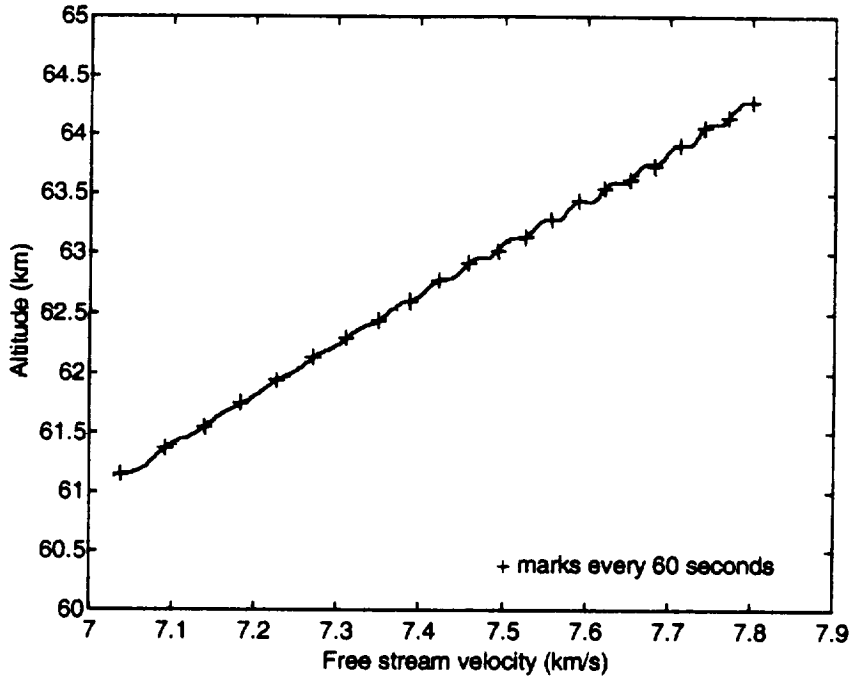

Figure 4-14: Entry profile

Figure 4-15 shows the altitude error in velocity-altitude coordinates, in keeping with the representation of Figure 4-14. The data shows the vehicle following the APC within 80 meters. This good agreement is not intended as a demonstration of controller performance, but shows the success of the end-to-end demonstration of the 6-DOF simulator including models of the aerodynamics and flight controls.

Figure 4-16 shows the time history of the vehicle's angle of attack. The angle of attack rises with time as in Figure 3-5. The slow oscillatory motion arises from the performance limitations of the altitude controller, while the instability at the end of the simulation run is due to performance limitations of the angle of attack controller.

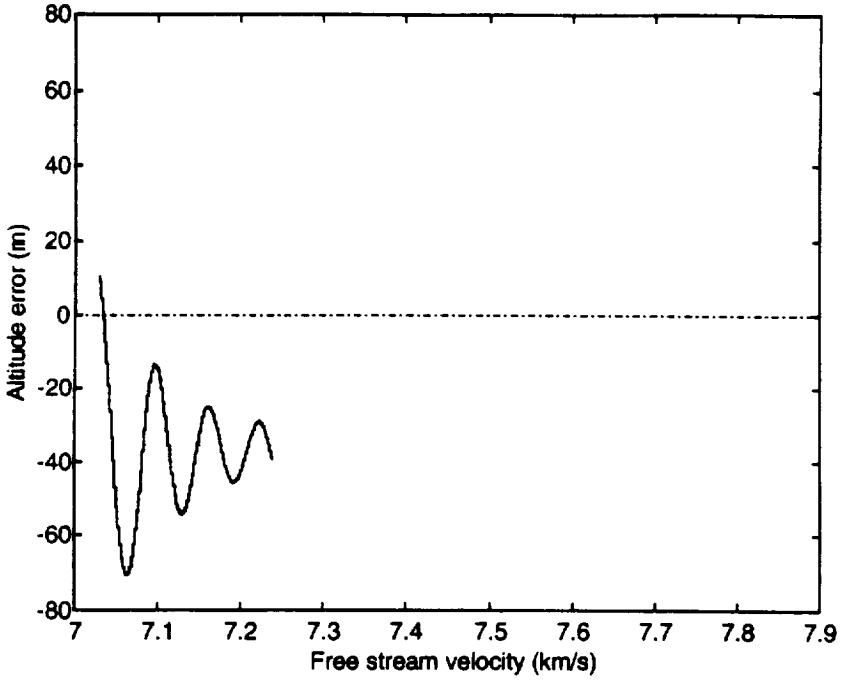

Figure 4-15: Altitude error

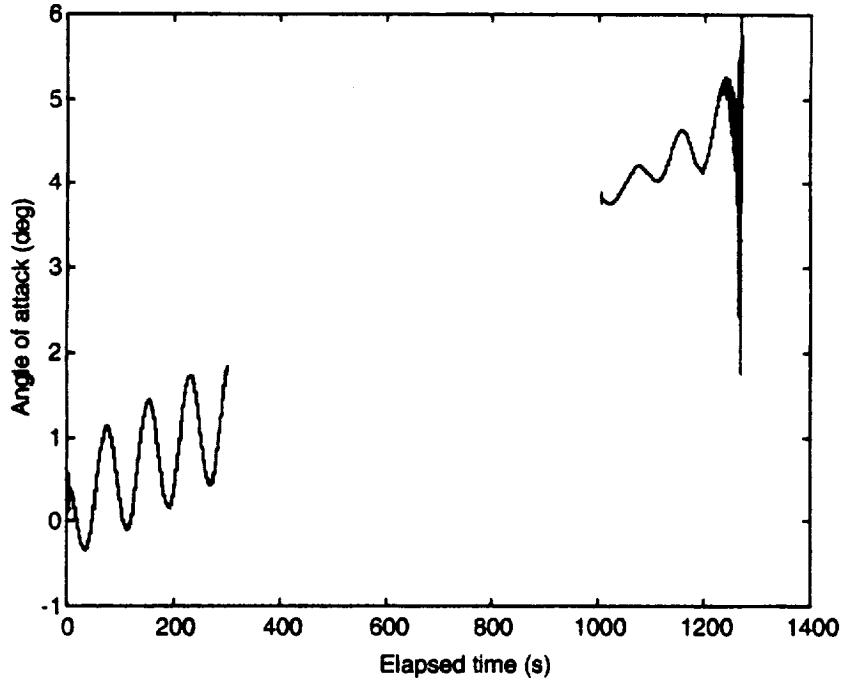

Figure 4-16: Angle of attack profile

Figure 4-17 shows the time history of the position angle of the center flap on the top side of the vehicle. The flap position first follows the slow oscillations in commanded angle of attack, and begins rapid oscillation near the end when the angle of attack controller becomes unstable. The small flap deployment angle bears out the data in Figure 4-11, considering the flap chord length was 15% of the vehicle length.

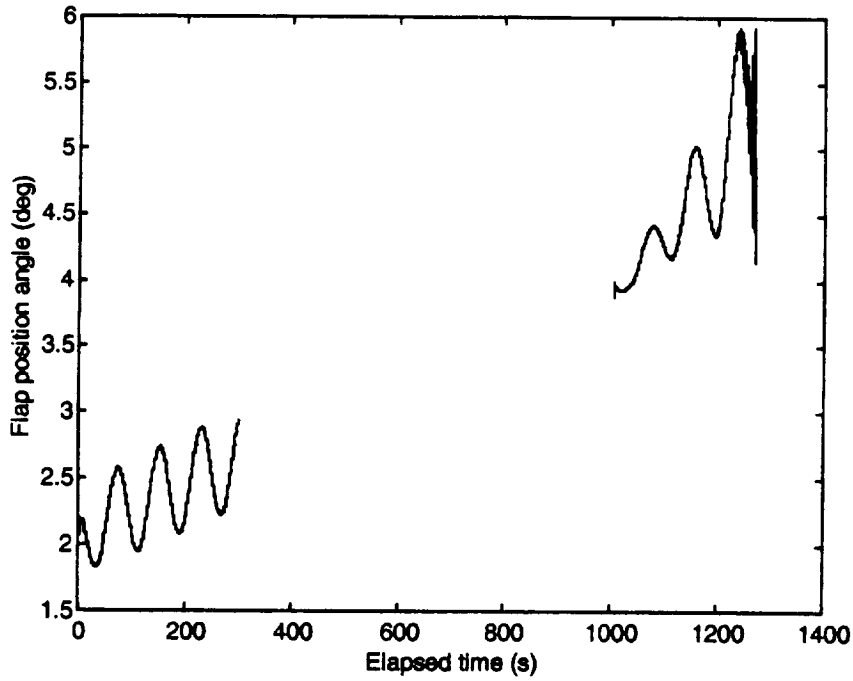

Figure 4-17: Flap position angle profile

The time necessary to perform the calculations was significant. The typical simulation step size was 30 milliseconds and the aerodynamic model was recalculated at every time step, for an overall simulation speed about ten times slower than real time. Note that the recalculation rate (determined by the SIMULINK solver based on the specified tolerances) is on the same order of magnitude as the simulation bandwidth determined in Chapter 2 and lends credence to that analysis. Solutions for speeding up the simulation are discussed in Chapter 5.

The 20-minute flight along the APC successfully demonstrates all the elements that are necessary for using simulation to support flight control development.

4.6 Summary

The 6-DOF simulator, built up from the trajectory simulator of Chapter 3, is demonstrated to be a useful tool for the development of the SHARP vehicle's entry flight control systems. This end-to-end demonstration is accomplished with a Newtonian aerodynamic model and a simple example autopilot in the simulation loop. The Newtonian aerodynamic model of SHARP is developed for the 6-DOF simulator and verified against the NASA-provided aerodynamic database of Chapter 3. The results are found to agree well at Mach numbers above 10. The new model can compute the aerodynamic forces and moments caused by sideslip; it is not limited to the pitch plane as for the aerodynamic database of Chapter 3. Control surfaces are modeled using Newtonian aerodynamics. While this practice is questionable, the use is justified in the case of SHARP (until a better flap model is implemented) because of the lesser effect of the leading edge on the downstream flow as well as the small deflection angles. The 6-DOF simulator is verified by comparing predicted and measured natural pitch oscillation dynamics. A visualization tool is developed to animate the dynamics of the vehicle and better understand its motion. Control surface sizing is briefly investigated, with rough estimates on the required sizes; a nominal six-flap configuration is analyzed. Finally, a rudimentary entry flight controller is developed to permit an end-to-end demonstration of the 6-DOF simulator in concert with the aerodynamic model.

CHAPTER 5: REAL TIME SIMULATION ISSUES

The requirements for real-time simulation (for hardware in the loop development) are briefly discussed with a focus on low-cost simulator components, since funding for this research was limited. While real-time simulation has been performed using inexpensive hardware [Sims 1996], it was not known if a low-cost approach would succeed when this research began. Since the SHARP project is not yet mature enough to attempt hardware development of the entry flight control computer (independently of whether or not a hardware in the loop system is used), the issues explored here will become relevant only later in the design process.

5.1 Background

Hardware in the loop (HWIL) simulation is a ground-based testing and validation method that is intended to reduce the risk and cost of flight testing aerospace vehicles. It is commonly used in manned and unmanned flight vehicle development programs. By providing a synthetic environment generated in real time, HWIL systems can exercise hardware and software subsystems under realistic conditions such as would be encountered in a flight test. This type of testing can be useful throughout the development of a system, from initial conceptual development to qualification and demonstration of flight readiness.

A HWIL simulation system must interface seamlessly with the device under test. While only an actual flight test can provide the desired environment, a properly designed HWIL system can emulate it very closely. A generic HWIL simulation test bed, as shown in Figure 5-1, consists of three distinct parts: the simulator that provides the synthetic

environment, the device under test, and a suitable interface to link the two. Software is every bit as important as hardware, so perhaps "hardware in the loop" should more accurately read "device in the loop".

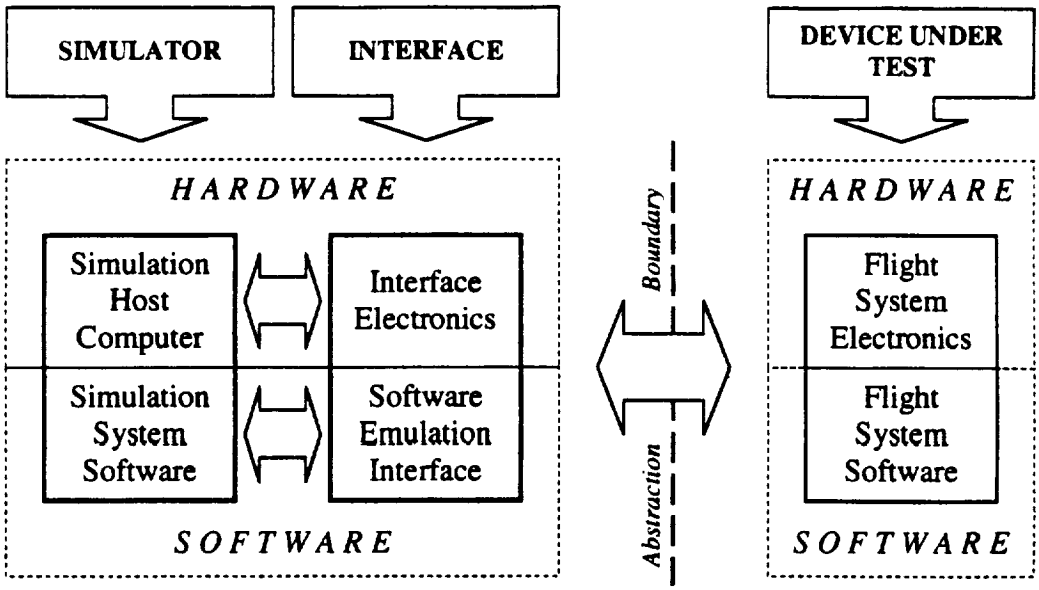

Figure 5-1: Hardware in the loop system architecture

The abstraction boundary (above) is the abstract interface between the simulation system and the device under test. With a good abstraction boundary the device under test cannot distinguish between HWIL operation and real operation. In particular, the simulation and interface must update at a rate significantly faster than the fastest dynamic of the device under test. This makes an estimation of the system bandwidth, as performed in Chapter 2, an important first step prior to component selection for the simulator.

Since this bandwidth is not accurately known prior to building a HWIL system to measure it, some guesswork is involved in selecting appropriate hardware and software for the simulator and interface, based on rough estimates.

5.2 A Low-Cost HWIL System for SHARP

Hardware in the loop simulation problems were explored subject to funding constraints, using Real Time Toolbox [Humusoft 1997] and a Data Translation DT2801 data

acquisition board. The DT2801 features eight 12-bit analog inputs, sixteen digital I/O channels, and two 12-bit analog outputs. The simulation host was a personal computer running Windows 95 on a 150 MHz Pentium microprocessor. The DT2801 interfaces to the computer's motherboard using the ISA bus.

For the purpose of developing the SHARP entry flight control computer, the interface between the simulation hardware and the device under test consists of electrical signals that travel to and from the flight computer. Simulated sensors drive the D/A outputs of the data acquisition board, mimicking the signals that would be experienced in flight. The flight computer outputs are fed into the A/D inputs of the data acquisition board to drive simulated actuators. At this writing no flight computer development has been attempted, as it is too early in the design process to do so.

Several issues arising from hardware and software limitations are addressed to evaluate the use of low-cost equipment for future SHARP HWIL simulation.

5.2.1 Channel Limitations

The Data Translation DT2801 is equipped with only two 12-bit digital-to-analog outputs. An entry flight control system, regardless of its exact configuration, requires more than two sensors in order to achieve its task. While this problem could be overcome using a more expensive data acquisition board with more output channels, the channel limitations can be overcome with output multiplexing.

Output multiplexing consists of combining several analog signals onto one physical channel by alternating time slices of the original signals. This scheme requires a synchronization signal so that the multiplexed output can be properly decoded into its component signals by external electronics. The original signals are then fed to the device under test.

This approach was demonstrated using one analog output channel and one digital output channel driven from a SIMULINK model. Three different simulated signal sources were multiplexed and a time synchronization signal generated using SIMULINK blocks. The multiplexed analog output and the synchronization signal drove the outputs of the data

acquisition board. Outside of the simulation host, a channel decoding circuit was designed around LF398 analog sample-and-hold integrated circuits. Using this circuit, the multiplexed signal was split and the three original analog signals were recovered. The overall process is depicted in Figure 5-2.

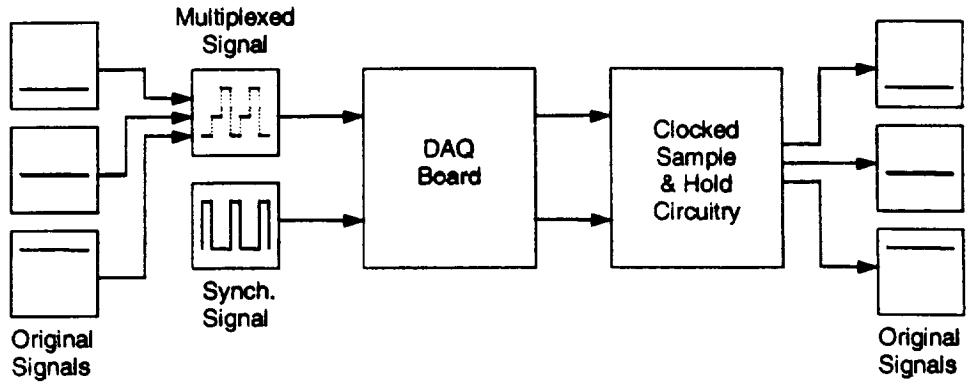

Figure 5-2: Analog output multiplexing

Concerns with the multiplexing approach are twofold. First, in order for each of the final decoded output signals to be driven at the frequency required by the system bandwidth, it is necessary to multiply the frequency of computation of the simulation by a factor of three, or however many analog signals are multiplexed together on each channel. This is because SIMULINK must sample the multiplexing blocks every time the multiplexed signal transitions from one input to the next. Since sample times are globally determined in SIMULINK, the entire model must be recalculated at each transition. If enough processing speed is available, this is a viable option. If not, a better acquisition board (with more D/A channels) must be purchased. This tradeoff is constrained mostly by cost. The second drawback of the multiplexing approach is that the external circuitry must be specially designed and calibrated to retain the full 12-bit output resolution of the acquisition board. Any offset voltages can introduce unwanted effects that are propagated through the simulation. For the demonstration this was not attempted.

5.2.2 Processing Speed Limitations

The 6-DOF model used in Chapter 4 is not optimized for speed. It includes several calls to the MATLAB workspace to run functions that compute the aerodynamic model or interpolate the entry constraint. This considerably slows the simulation speed, as the

MATLAB interpreter is called each time. The 30 Hz recalculation frequency that was deemed necessary in Chapter 2 cannot be achieved with these inefficiencies, especially when the need for multiplexing is factored in. To speed up the simulation, several approaches are possible. These are:

1) Rewrite the function calls to MATLAB as SIMULINK S-Functions. S-Functions use a special calling syntax that allows them to interact with the SIMULINK solver in the same manner as other simulation blocks. When they are written in C language and compiled, calls to the MATLAB interpreter become unnecessary.

2) Upgrade to a faster computer. The 150 MHz Pentium processor used in this research is out of date as of this writing. A speed gain of a factor of three can already be had with current PC technology, and progress continues rapidly.

3) Switch to using Real Time Workshop [MathWorks 1997], a package that can convert a SIMULINK model to faster and more efficient code that can run native on the processor. The switch to compiled execution (rather than interpreted execution) will result in a significant speed gain.

While the above suggestions are made with the goal of achieving the speed for full hardware in the loop simulation, an alternate strategy is suggested for future development. Using an open loop, stimulus-response method can possibly help to test flight hardware. Using this method the SIMULINK model could be solved off-line, thus obviating the processing speed limitations. The stimulus response method might consist of the following steps:

1) An initial guess of the time history of the sensor parameters is fed in real time into the flight hardware. The flight hardware's response is recorded.

2) The recorded response is played back into an off-line (non real time) simulation of the vehicle's environment. The hardware's response drives the simulated actuators. The actuators affect the vehicle dynamics, and the vehicle dynamics in turn affect the simulated sensors. The simulated sensors' outputs are recorded.

3) The sensor output history is fed back in real time into the flight hardware. Once again the flight hardware's response is recorded, and the process is iterated until it possibly converges. (Convergence is speculative and certainly not guaranteed)

Until this approach is tested its validity or success cannot be evaluated.

5.2.3 Cost Constraints

In this research the expense for simulation hardware is quite limited. The limitations of the simulator hardware, pointed out in the previous two sections, suggest that real time hardware in the loop simulation is not easily done at such low cost. The tradeoffs between hardware and software approaches for solving simulation problems are changed according to the allowable expense. For example, increasing simulation speed through compilation might not be as attractive as purchasing a faster computer if the budget allows it. The total budget for hardware and software in this project was under $2000. On the scale of an aerospace project such as SHARP, this is an insignificant amount. While the simulation tools were shown to be useful for trajectory and vehicle dynamics analyses in Chapters 3 and 4, the low-cost setup does not appear suitable for real time simulation.

5.3 Summary

Hardware in the loop simulation issues were discussed with a focus on low-cost systems. Using the Real Time Toolbox for SIMULINK and a data acquisition board, a simulation interface was described. Limitations of the system (number of channels, computing power) are thought to be avoidable through strategies such as output multiplexing or open loop stimulus-response simulation, although these approaches were not proven. The choice of whether to solve a problem by hardware or software (for example, software multiplexing vs. a better data acquisition board) remains a tradeoff and is driven by cost. While the prospect of effective and useful HWIL simulation appears unreachable with a low-cost setup, it can be expected that future performance increases in hardware and software will make it possible within a few years. In light of this, the choice of widely used commercial products such as SIMULINK is a good one since they will almost certainly be supported on future computer hardware. Migrating the simulation tools

developed in this thesis to a more advanced system will thus be a matter of evolution, rather than revolution. With the cost constraint removed, a more capable system is clearly preferable for HWIL simulation-based development of the SHARP entry flight control systems.

CHAPTER 6: CONCLUSIONS AND FUTURE WORK

6.1 Conclusions

This thesis described the analysis of the capabilities of the SHARP high-performance lifting atmospheric entry vehicle using custom developed numerical simulation tools. These simulation tools are more powerful than closed form modeling and analysis and provide the ease of use, flexibility and extensibility necessary for rapidly gaining insight into system-level tradeoffs. Two tools were developed, each with several variants: a trajectory simulator, integrating a NASA-provided aerodynamic database, and a six degree of freedom simulator, using a Newtonian aerodynamic model. These tools were used to investigate a series of design issues facing the SHARP mission. The trajectory simulator was used to investigate the trajectory design space, or entry flight envelope, and the effect of entry parameters on the vehicle's aerodynamic, structural and thermal environment. The 6-DOF simulator was used to perform a preliminary study of control surface configuration, and showed the vehicle could be controlled to follow a designated entry profile. This simulator is well suited to future flight control system development. The simulation tools were delivered to NASA vehicle designers to assist further conceptual development on the SHARP mission.

6.1.1 Trajectory Simulation

The trajectory simulator demonstrated the capability for generating atmospheric entry trajectories for the SHARP vehicle. The simulator incorporated the vehicle model and the planetary and atmospheric model in such a way as to make it easy to configure the

simulator for a different vehicle or a different planet. The trajectory simulator was verified by comparing results with another established trajectory simulator; the agreement was almost perfect. Using the NASA-provided aerodynamic database for the SHARP vehicle the simulator demonstrated the ability to generate aerodynamic angle profiles needed to follow a designated entry profile. With two of the three aerodynamic angles determined, the simulator solved for the missing degree of freedom.

In particular, the simulator provided the first quantitative look at the range of possible entry trajectories along the aerothermal performance constraint of the leading edge TPS. In one case the roll angle was fixed at zero and the required angle of attack profile was generated, while in the other the angle of attack was fixed at a high value and the required roll angle profile was generated. These two different cases demonstrated the range of possible entry trajectories and gave quantitative information on heating rates, structural loads, aerodynamic angles, and many other flight parameters. The results showed a tight coupling between trajectory choice and the environment experienced by the vehicle, and thus proved that vehicle design choices are strongly driven by trajectory choice.

The trajectory simulation capability is required for multi-disciplinary optimization of the SHARP vehicle design. While no formal optimization was attempted, the trajectory simulator nonetheless demonstrated the capability for quickly producing trajectory data subject to the variation in one parameter, the vehicle mass. This type of parameter sensitivity study could be repeated for any other vehicle property in the model.

The trajectory simulator, built in the Simulink environment, has attributes that will make it useful in further research on the SHARP project or in other atmospheric entry problems. These include flexibility, ease of use, power, extensibility, and affordability.

6.1.2 6-DOF Simulation

The six-degree of freedom simulator extended the capability of the trajectory simulator and sets the stage for flight control system development. The simulator demonstrated the ability to solve for the six degrees of freedom of the motion of the vehicle on time scales sufficient for an entire entry trajectory.

To fully demonstrate the 6-DOF simulator a new aerodynamic model was necessary. The NASA-provided aerodynamic database used in the trajectory simulator only provided the required parameters in the pitch plane. To remove this limitation a replacement model was developed using Newtonian theory. The SHARP vehicle was decomposed into polygonal facets; at each simulation time step the forces and moments imparted to each facet were recomputed. The model included movable control surfaces and was designed so changes in the vehicle geometry (for example, control surface placement) could be implemented easily and quickly. The Newtonian aerodynamic model was verified against the NASA-provided aerodynamic database and showed adequate agreement in lift, drag and pitching moment coefficients at speeds above Mach 10.

The 6-DOF simulator was augmented with a visualization tool that displays a three-dimensional animation of the vehicle motion. The visual display was a more intuitive way to understand the behavior of the vehicle than individual plots of the aerodynamic angles or control surface position angles.

The 6-DOF simulator can be used to generate entry trajectory parameters based on the aerodynamic model and a flight control system implementation. This capability was demonstrated with several minutes of actively controlled flight along the aerothermal performance constraint, using an example controller and assuming perfect state knowledge. The capability for analyzing the vehicle's flight dynamics for a wide range of conditions is valuable for the purpose of eventual flight control system development.

6.1.3 Real Time Capability

The 6-DOF simulator was designed from the outset with real time capability in mind. As flight control system development progresses, real time simulation with hardware functioning in the simulation loop becomes a powerful development and testing method. Simulation system performance using an affordable personal computer proved insufficient to achieve the desired capability. For a budget not constrained to the $2000 spent on simulator components in this research, however, much more effective options become available for hardware in the loop simulation.

6.2 Suggestions for Future Work

At this time the SHARP program is in early conceptual development. The requirements for lifting entry include an active flight control system to perform guidance, navigation and control tasks during the entry flight. This requirement alone is a major challenge which would likely involve many engineers for a period of several years. The extent and complexity of the development task ahead make it very easy to find further avenues of research.

6.2.1 Trajectory Optimization

The trajectory studies performed in Chapter 3 highlighted the close coupling between trajectory choice and vehicle parameters. The mission goal of following the aerothermal performance constraint does not lead to a unique trajectory solution; indeed, many free parameters remain to be optimized. As the design of the SHARP vehicle progresses, more accurate data will become available on the consequences of certain design choices on performance and cost. This will make it possible to perform a formal multidisciplinary optimization, using a well-constructed objective function. Defining the parameters of an objective function is impossible at the present point in the design process, but will become feasible when design details become better understood. The optimization process will ensure the best design choices are made to achieve the mission.

6.2.2 Improved Aerodynamic Model

The Newtonian aerodynamic model developed in Chapter 4 has many limitations. Without a good aerodynamic model the task of developing a flight control system is not possible. Since this is one of the most promising applications of the 6-DOF simulator, an improved aerodynamic model is a high priority. A more sophisticated aerodynamic model would have to contend with issues of computer storage and execution since so many parameters affect the aerodynamic coefficients of the vehicle. This is simply a reflection of the complexity of the aerodynamic effects encountered in re-entry. In particular, special attention should be paid to the control surface model. As mentioned in Chapter 4, modeling hypersonic control surfaces with Newtonian aerodynamics is not

recommended practice, even if the SHARP geometry alleviates some of the concerns with doing so. In general, an improved aerodynamics model should strike the appropriate balance between fidelity and complexity.

6.2.3 Flight Control System Development

Once an improved aerodynamics model is implemented, the most interesting application of the 6-DOF simulator is flight control system development. SIMULINK is a powerful tool for the task and controller designs could very easily be integrated and tested with the simulator. Since the vehicle's response depends on its environment, this task amounts to more than adjusting a few gains. Several references provide insight into the shuttle orbiter entry flight control design [JSC 1973, Graves 1978, Kafer 1983] and would provide a good starting point for attacking the problem. The flight control system would have to tolerate uncertainties in state estimation and in aerodynamic modeling, while still achieving the mission goal of following the designated entry flight profile as closely as possible. Measuring the effect of parameter variations on trajectory performance metrics can test this robustness.

6.2.4 Hardware Development

As the flight control system design progresses, simulation tools can be used to begin hardware development. The 6-DOF simulator could be extended with external hardware and software interfaces specific to the hardware configuration of the flight computer. Using these interfaces the code could be tested in closed loop with the simulator providing a synthetic environment. Pre-flight hardware in the loop testing of flight software using a simulated environment is a standard phase for any flight system that is difficult or expensive to test in flight, but itself need not be costly. Flight code validation using simulation has been applied using inexpensive computers and hardware interfaces [Sims 1996]. With the rapid progress of computer technology, the approach promises to be more and more accessible.

APPENDIX A: SHARP VEHICLE PARAMETERS

A.1 Geometry

The SHARP vehicle is wedge-shaped, with conical sides and a sharp leading edge. Hankey originally investigated this class of hypersonic lifting vehicle shapes, which explains why SHARP is sometimes referred to as a "Hankey wedge" [Kolodziej 1998]. A few key physical dimensions are indicated in the drawings below.

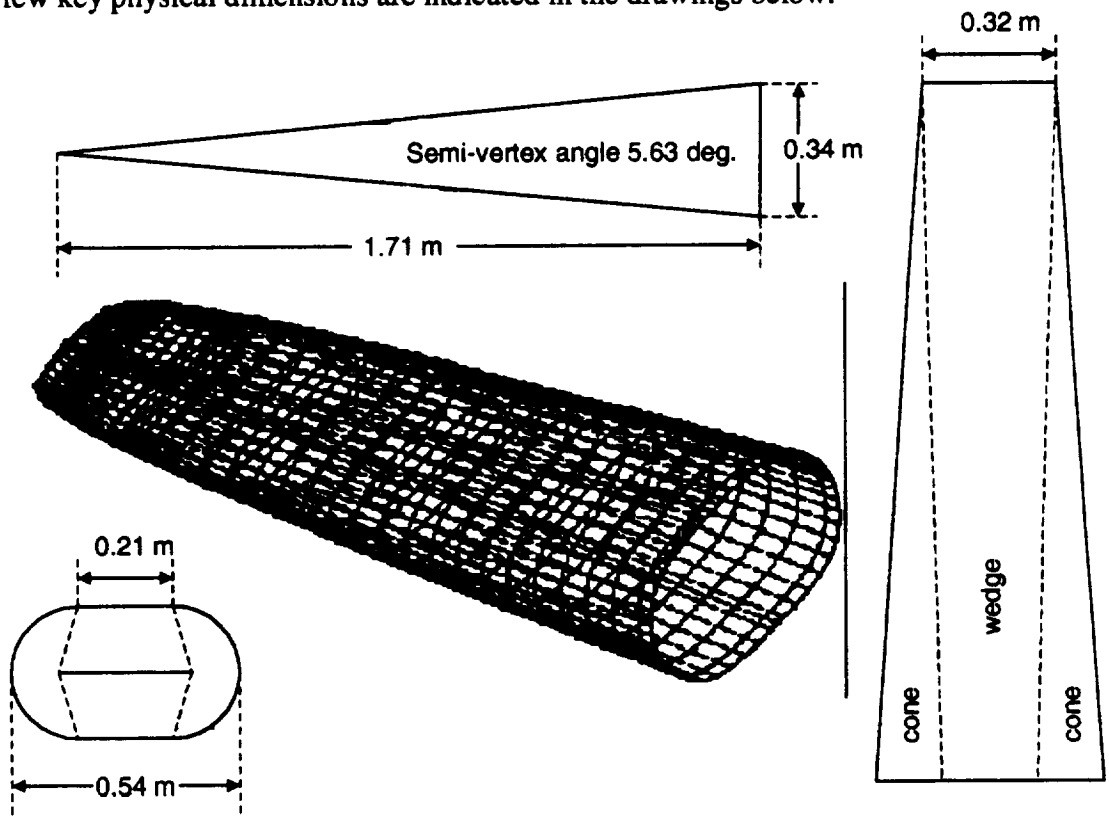

Figure A-1: SHARP vehicle geometry

The wire-frame drawing at the center of Figure A-1 is a more refined configuration than what appears in the dimensioned drawings. Aerodynamic control surfaces are not shown in the drawing because their configuration is not uniquely specified.

For further description of the vehicle, we adopt a body axes system with its origin at the vehicle's center of gravity. The x-axis is taken along the length of the vehicle (from back to front), the y-axis along its width (from left to right) and the z-axis downward (from top to bottom).

A.2 Mass Properties

The mass M of the vehicle was assumed to be 113.4 kg (250 lbs.) unless otherwise specified. The center of gravity location, of great importance to the aerodynamic stability of the vehicle, was set at 50% of the vehicle length, in the center of the body, unless otherwise specified. The moments of inertia, which factor into the attitude dynamics of the vehicle, were computed approximately based on the mass and geometry. For this purpose the geometry was simplified to an isosceles triangular prism with h = 0.337 m, L = 1.71 m, and w = 0.381 m, as shown in Figure A-2.

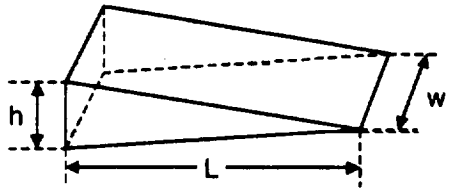

Figure A-2: Simplified wedge geometry

A.2.1 Mass Distribution

The prism was split into two pieces of length $L/2$, each with homogeneous density, with the total mass distributed so as to place the center of gravity of the entire wedge at one-half its length. (With a completely homogeneous wedge the CG would be two-thirds of the way back.) Let m_1 and m_2 be the respective masses of the front and back halves of the wedge, with $m_1 + m_2 = M$. Their densities ρ_1 and ρ_2 are then:

$$\rho_1 = \frac{8m_1}{Lwh}, \quad \rho_2 = \frac{8m_2}{3Lwh}.$$

We then balance the moments of the front and back about the CG by solving

$$\int_{front} \rho_1 x\, dV = \int_{back} \rho_2 x\, dV,$$

giving $m_1 = 5M/8$ and $m_2 = 3M/8$. This mass distribution ensures the center of gravity is located exactly as desired. Knowing the mass distribution we may go on to calculate the moments of inertia.

A.2.2 Moments of Inertia

The moments of inertia were calculated from the standard formulas. For a wedge as in Figure A-2, simple algebra starting from the formula for the moment of inertia of a slab about its CG and using the parallel-axis theorem yields the following principal moments of inertia:

$$I_{yaw} = \frac{M}{6}\left(\frac{L^2}{3} + \frac{w^2}{2}\right), \quad I_{pitch} = \frac{M}{6}\left(\frac{L^2}{3} + \frac{h^2}{4}\right), \quad I_{roll} = \frac{M}{12}\left(\frac{h^2}{2} + w^2\right).$$

To account for the distribution of mass as calculated above, we use the parallel axis theorem to determine the principal moments of overall configuration.

Axis	Formula	Value (kg·m^2)
Yaw (z)	$I_z = \frac{M}{4}\left(\frac{L^2}{4} + \frac{w^2}{3}\right)$	22.1
Pitch (y)	$I_y = \frac{M}{8}\left(\frac{L^2}{2} + \frac{h^2}{3}\right)$	21.2
Roll (x)	$I_x = \frac{M}{12}\left(\frac{5h^2}{12} + w^2\right)$	1.82

Table A-1: SHARP inertia properties

APPENDIX B:

TRAJECTORY SIMULATOR DESCRIPTION

B.1 Model Block Diagram

The description of the block diagram for the trajectory simulator refers to Figure B-1. In the figure each block is labeled with a number. The blocks are described in the order of their numbers. They are all SIMULINK "subsystems" in that they each contain more sub-blocks. For the purpose of the description the different levels are not explained to the last detail, as the model includes hundreds of elementary SIMULINK blocks.

The block diagram here is one particular configuration of the trajectory simulator, showing a controller for the angle of attack. This configuration is not unique, as either or both of angle of attack and roll angle can be controlled from other parameters in the model. The model is easily modified to suit the problem being investigated; for each of the sections in Chapter 3, different configurations were used.

All blocks sending simulation data to the MATLAB workspace have been deleted for clarity.

For additional details the reader is referred to the actual SIMULINK files; these are available from the archives of the Space Systems Development Laboratory at Stanford University.

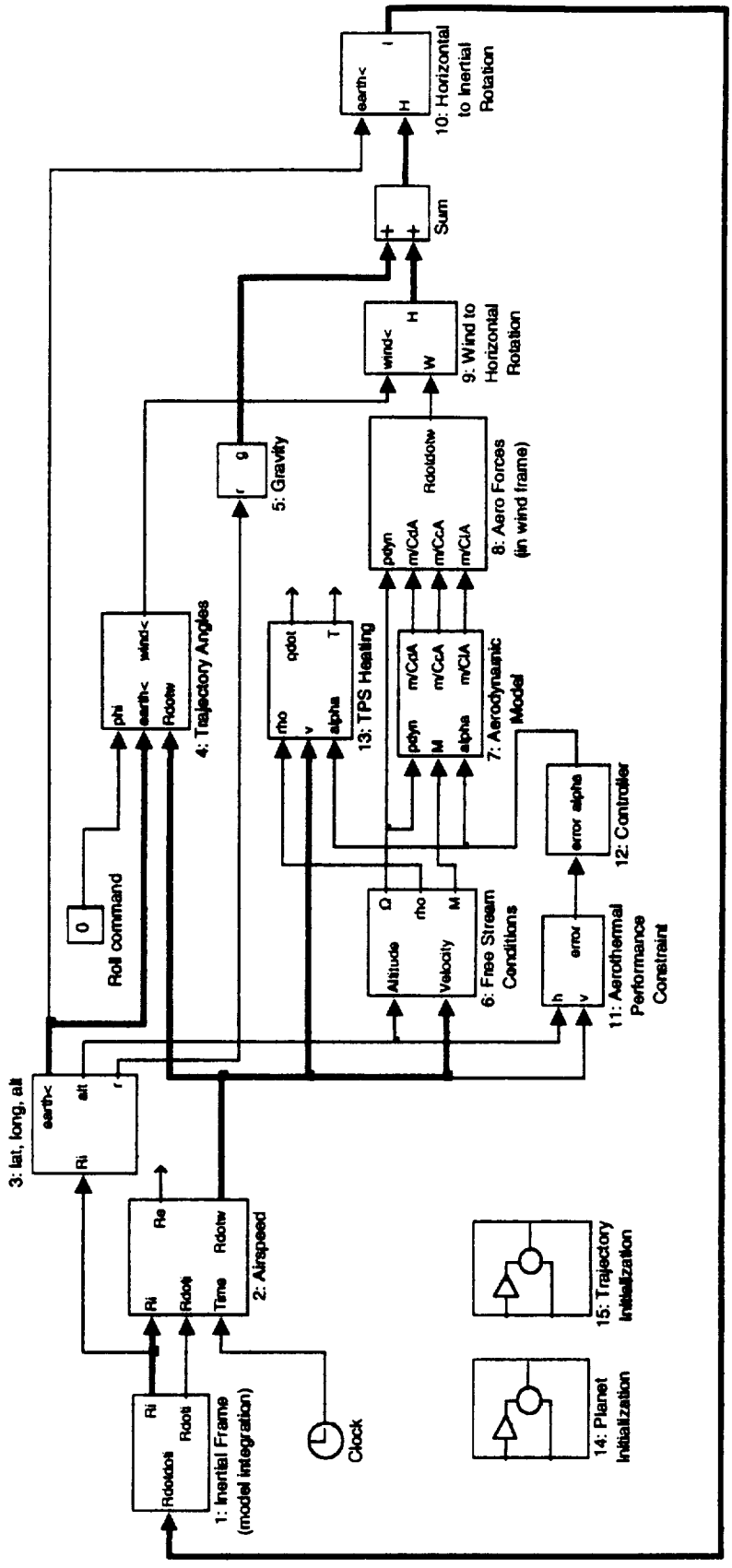

Figure B-1: Trajectory simulator block diagram

B.2 Block Descriptions

1) **Inertial Frame**: This block is where the motion of the vehicle is integrated. The input of the block is the acceleration of the vehicle in the inertial frame. Inside this block, this signal is integrated twice to produce the velocity and position in inertial space. Both integrators have their initial condition set by block 15, Trajectory Initialization. The integration scheme is 4^{th} order Runge-Kutta with adaptive time step, built into SIMULINK. The relative tolerance is 10e-3 and the absolute tolerance is 10e-6.

2) **Airspeed**: This block computes the free stream velocity vector in the wind frame and the position vector in the earth frame. The earth frame rotates with the earth rather than being fixed in inertial space. The position vector in the earth frame is useful for plotting trajectories as seen from the surface of the earth. It also allows comparison with the inertial position vector to see the effect of earth rotation on the trajectory (Coriolis effect). The free stream velocity vector is computed by subtracting the cross product of earth's angular rotation vector and the position vector from the inertial velocity vector.

3) **Lat, Lon, Alt**: This block computes the latitude, longitude and altitude of the vehicle. The latitude and longitude are calculated for the purpose of rotations later in the model, and are inertial-referenced, as opposed to the conventional earth-referenced definition. The sine and cosine of both angles are passed along to the earth angle output to avoid redundant recomputation of these quantities further downstream. The altitude of the vehicle is computed by subtracting the local earth radius (the earth being modeled as an oblate spheroid) from the magnitude of the position vector. The magnitude of the position vector is also passed along, for computing the acceleration of gravity.

4) **Trajectory Angles**: This block computes the Euler angles of the wind frame with respect to the locally horizontal frame. This includes the heading angle and the

trajectory angle (the angle that the velocity vector makes from horizontal.) The roll angle (defined as roll around the velocity vector) is also included, and is fed in via either a constant input (as shown in the block diagram) or by a controller similar to the one of blocks 11 and 12. All angles are passed along with their sine and cosine to avoid redundant computation further downstream.

5) **Gravity**: This block computes the acceleration due to gravity based on the distance of the vehicle from the center of the earth. There is no high order gravitational field model but this could be included as a future improvement.

6) **Free Stream Conditions**: This block takes the altitude and the velocity of the vehicle, and computes the free stream Mach number and dynamic pressure. Dynamic pressure is determined by a table lookup of density (based on the U.S. Standard Atmosphere). Mach number is determined by dividing the free stream velocity by the sound speed, also determined by table lookup from the atmospheric model.

7) **Aerodynamic Model**: This block implements the aerodynamic model for SHARP, based on the database computed by NASA. Any other aerodynamic database can be substituted. The database takes three inputs (angle of attack, Mach number and dynamic pressure) and computes lift and drag coefficients. This feature is implemented using calls to the MATLAB function "interp3" which performs three-dimensional interpolation of the three-dimensional matrix of aerodynamic data. The coefficients are combined with the vehicle mass and reference area and passed along in the same form as the familiar ballistic coefficient. Three values are passed to the output: one for lift, one for drag and one for side force. The side force is defined to be zero.

8) **Aero Forces (wind frame)**: This block takes the values passed by the aerodynamic model and computes the acceleration due to aerodynamic forces experienced by the vehicle in the wind frame. This is done by simply multiplying by the dynamic pressure and forming the output vector in the wind frame.

9) **Wind to Horizontal Rotation**: This block takes the Euler angles of the wind frame and transforms the acceleration vector to the horizontal frame using the usual rotation

matrices. This transformation is accurate since the relative angular velocity of the two frames is always small enough to be negligible.

10) **Horizontal to Inertial Rotation**: After adding gravity, the input of this block is the net acceleration on the vehicle from gravity and aerodynamic forces. Using the usual rotation matrices the vector is transformed to the inertial frame. This transformation is accurate since the relative angular velocity of the two frames is always small enough to be negligible.

11) **Aerothermal Performance Constraint**: This block is specific to the configuration of the trajectory simulator as shown in Figure B-1. In this configuration the angle of attack of the vehicle is controlled so the vehicle follows its aerothermal performance constraint. Alternately this could be any flight profile and not just the APC. The block computes the altitude error by doing a table lookup of velocity to find the altitude corresponding to the APC. This value is then subtracted from the actual altitude of the vehicle to form the error signal.

12) **Controller**: This block is a PID controller which determines the correct angle of attack for staying on the APC (or on whichever trajectory is desired, according to block 11). The output angle of attack is fed directly into the aerodynamic model. There is no modeling of the vehicle's pitch dynamics.

13) **TPS Heating**: This block uses the flight conditions to compute aerodynamic heating rate and temperature on the aft-body TPS of the vehicle. Radiation equilibrium is assumed, so that input heat rate determines surface temperature. Both quantities are computed using the empirical relations for a flat plate as derived by Tauber [Tauber 1997]. Since heating rate and temperature depend on each other (a situation denoted as "algebraic loop" in SIMULINK) a special algebraic constraint block must be used.

14) **Planet Initialization**: This block allows the user to specify the characteristics of the planet on which the entry is done. These characteristics include polar radius, equatorial radius, rotation rate and mass. Planets other than earth can easily be specified as long as the atmospheric model (embedded in block 6) is also changed. One interesting investigation using this block is to vary the earth's rotation rate.

15) **Trajectory Initialization**: This block allows the user to specify the trajectory initial conditions in a familiar form. The latitude, longitude, altitude, heading angle, entry angle and speed can be changed at will. The block then uses these quantities (and the inputs of block 14) to compute the initial velocity and position vectors in the inertial frame. These vectors are then used as initial conditions for the integrators in block 1.

B.3 User's Guide

To use the simulator, follow these steps:

1) Launch MATLAB

2) Type 'simulink' at the prompt

3) From the SIMULINK File menu, select the model to be opened

4) In MATLAB, run 'sharpinit.m'. This file creates all the variables necessary for the aerodynamic database interpolation.

5) In MATLAB, run the m-file that specifies the entry profile to be flown (if applicable)

6) By clicking on the appropriate blocks, enter the desired planetary characteristics and trajectory start conditions.

7) Place all the 'To Workspace' blocks required for collecting data to the MATLAB workspace.

8) From the Simulation menu in SIMULINK, select the stop time, the integration method and the solver tolerances.

9) From the Simulation menu, select 'Start'.

10) Monitor simulation progress by clicking on the 'clock' block.

11) When simulation ends, display and analyze data using MATLAB plotting functions. Useful m-files include 'plotapc.m' for plotting the aerothermal performance constraint and 'earth3.m' for displaying a three dimensional plot of the earth for trajectory plotting.

APPENDIX C: TRAJECTORY SIMULATION DATA

The data in the following pages is referred to from Chapter 3. Three different trajectories are logged, all originating from a 400-km circular equatorial orbit after the vehicle performs a 98.5 m/s de-orbit burn. The entry interface is taken to be at 100-km altitude and the simulation ends when vehicle slows below Mach 2.

C.1 Data Key

The data tables C-2, C-3 and C-4 in the next few pages have each column headed with a symbol. The meaning of the symbols is detailed in Table C-1 below.

Symbol	unit	Description
t	s	Elapsed time since entry interface
h	m	Altitude above surface of oblate earth
v	m/s	Free-stream velocity
a	m/s^2	Acceleration in wind axes, magnitude
$a_{x,y,z}$	m/s^2	Components of a
M	-	Free-stream Mach number
q	N/m^2	Free-stream dynamic pressure
ψ	deg	Heading angle
γ	deg	Flight path angle
ϕ	deg	Roll angle
α	deg	Angle-of-attack
C_D	-	Drag coefficient
C_L	-	Lift coefficient
r	m	Range (along ground track)
l	m	Lateral range (from original ground track)
T	K	Aft-body temperature
c	W/m^2	Aft-body heating rate

Table C-1: Symbol key

Table C-2: High lift to drag entry along the APC (See Section 3.3.1.1)

t	h	v	a	a_x	a_y	a_z	M	q	ψ	γ	ϕ	α	C_D	C_L	r	l	T	c
0	100457.0	7448.6	0.002	-0.002	0.000	0.000	25.7	14.5	90	-0.98	0	0	0.026	0.000	0	0	628	7499
60	93136.6	7457.6	0.009	-0.009	0.000	0.000	26.6	54.7	90	-0.89	0	0	0.026	0.000	447178	0	720	12955
120	86521.1	7465.0	0.028	-0.028	0.000	0.000	27.0	171.9	90	-0.80	0	0	0.026	0.000	894856	0	808	20504
180	80638.9	7469.7	0.074	-0.074	0.000	0.000	27.0	457.9	90	-0.70	0	0	0.026	0.000	1342898	0	885	29550
240	75498.0	7469.2	0.167	-0.167	0.000	0.000	26.1	1028.2	90	-0.61	0	0	0.026	0.000	1791063	0	947	38767
300	71066.5	7460.6	0.318	-0.318	0.000	0.000	25.2	1973.9	90	-0.53	0	0	0.026	0.000	2238941	0	987	45777
360	67244.6	7440.8	0.509	-0.509	0.000	0.000	24.4	3331.6	90	-0.46	0	0	0.025	0.000	2685927	0	1000	48223
420	64107.2	7407.5	0.869	-0.729	0.000	-0.472	23.8	5000.3	90	-0.30	0	1.1	0.024	0.015	3131272	0	1182	93932
480	62612.0	7362.3	0.983	-0.825	0.000	-0.535	23.4	5988.3	90	-0.09	0	1.0	0.022	0.014	3574174	0	1201	100384
540	62370.3	7313.9	0.828	-0.808	0.000	-0.178	23.2	6096.9	90	-0.04	0	0.3	0.021	0.005	4014209	0	1168	89747
600	62144.0	7265.2	0.879	-0.822	0.000	-0.312	23.0	6194.3	90	-0.03	0	0.6	0.021	0.008	4451341	0	1177	92573
660	61917.9	7215.7	0.943	-0.835	0.000	-0.438	22.8	6291.3	90	-0.03	0	0.8	0.021	0.011	4885526	0	1185	94986
720	61694.3	7165.5	1.015	-0.848	0.000	-0.559	22.6	6385.9	90	-0.03	0	1.0	0.021	0.014	5316717	0	1191	97051
780	61471.2	7114.6	1.096	-0.860	0.000	-0.679	22.4	6479.6	90	-0.03	0	1.2	0.021	0.017	5744871	0	1197	98930
840	61247.2	7063.0	1.184	-0.872	0.000	-0.801	22.2	6573.6	90	-0.03	0	1.4	0.021	0.020	6169944	0	1202	100649
900	61021.0	7010.6	1.278	-0.884	0.000	-0.923	22.0	6668.8	90	-0.03	0	1.6	0.021	0.022	6591893	0	1207	102221
960	60791.4	6957.5	1.378	-0.896	0.000	-1.046	21.8	6766.2	90	-0.03	0	1.7	0.021	0.025	7010675	0	1211	103647
1020	60557.5	6903.7	1.482	-0.909	0.000	-1.170	21.6	6866.8	90	-0.03	0	1.9	0.021	0.028	7426246	0	1215	104934
1080	60318.6	6849.1	1.589	-0.922	0.000	-1.295	21.4	6971.1	90	-0.03	0	2.1	0.021	0.030	7838560	0	1218	106076
1140	60074.2	6793.8	1.701	-0.935	0.000	-1.421	21.2	7079.6	90	-0.03	0	2.3	0.021	0.032	8247572	0	1221	107106
1200	59824.3	6737.9	1.815	-0.947	0.000	-1.548	21.0	7179.5	90	-0.04	0	2.4	0.021	0.035	8653244	0	1223	107942

t	h	v	a	a_x	a_y	a_z	M	q	ψ	γ	ϕ	α	C_D	C_L	r	l	T	c
1260	59566.9	6681.0	1.932	-0.966	0.000	-1.673	20.8	7278.7	90	-0.04	0	2.6	0.021	0.037	9055531	0	1225	108584
1320	59299.2	6622.6	2.057	-0.992	0.000	-1.802	20.6	7384.2	90	-0.04	0	2.7	0.022	0.039	9454355	0	1227	109134
1380	59020.7	6562.7	2.185	-1.018	0.000	-1.934	20.4	7496.5	90	-0.04	0	2.9	0.022	0.042	9849624	0	1228	109551
1440	58730.8	6501.3	2.317	-1.045	0.000	-2.068	20.2	7616.3	90	-0.04	0	3.0	0.022	0.044	10241245	0	1229	109839
1500	58428.9	6438.2	2.451	-1.072	0.000	-2.204	20.0	7744.4	90	-0.05	0	3.2	0.022	0.046	10629123	0	1229	109986
1560	58113.9	6373.6	2.588	-1.100	0.000	-2.343	19.7	7881.7	90	-0.05	0	3.3	0.023	0.048	11013162	0	1229	109983
1620	57784.8	6307.2	2.728	-1.129	0.000	-2.484	19.5	8029.7	90	-0.05	0	3.4	0.023	0.050	11393260	0	1229	109837
1680	57441.4	6239.1	2.870	-1.158	0.000	-2.626	19.3	8188.8	90	-0.05	0	3.6	0.023	0.052	11769318	0	1228	109529
1740	57083.7	6169.3	3.015	-1.187	0.000	-2.771	19.0	8359.1	90	-0.06	0	3.7	0.023	0.054	12141230	0	1227	109068
1800	56712.3	6097.8	3.162	-1.217	0.000	-2.918	18.8	8540.9	90	-0.06	0	3.8	0.023	0.055	12508893	0	1225	108447
1860	56324.5	6024.5	3.311	-1.247	0.000	-3.067	18.5	8736.9	90	-0.06	0	3.9	0.023	0.057	12872201	0	1223	107671
1920	55916.3	5949.4	3.463	-1.277	0.000	-3.218	18.3	8952.6	90	-0.07	0	4.0	0.023	0.058	13231050	0	1220	106742
1980	55484.8	5872.6	3.618	-1.308	0.000	-3.374	18.0	9191.8	90	-0.07	0	4.1	0.023	0.059	13585333	0	1217	105689
2040	55034.1	5793.9	3.775	-1.338	0.000	-3.530	17.7	9451.5	90	-0.08	0	4.1	0.023	0.060	13934944	0	1213	104451
2100	54567.9	5713.6	3.930	-1.367	0.000	-3.684	17.5	9728.5	90	-0.08	0	4.2	0.023	0.061	14279775	0	1209	103001
2160	54077.2	5631.5	4.084	-1.396	0.000	-3.838	17.2	10035.0	90	-0.09	0	4.2	0.022	0.062	14619726	0	1204	101397
2220	53549.6	5547.8	4.245	-1.425	0.000	-3.999	16.9	10370.8	90	-0.09	0	4.2	0.022	0.062	14954695	0	1199	99714
2280	52990.6	5462.4	4.410	-1.454	0.000	-4.163	16.7	10745.2	90	-0.10	0	4.2	0.022	0.063	15284584	0	1194	97912
2340	52412.2	5375.4	4.570	-1.481	0.000	-4.323	16.4	11149.3	90	-0.10	0	4.2	0.021	0.063	15609291	0	1188	95926
2400	51814.6	5286.9	4.730	-1.507	0.000	-4.484	16.1	11585.1	90	-0.11	0	4.2	0.021	0.063	15928724	0	1181	93809
2460	51194.1	5196.9	4.887	-1.534	0.000	-4.640	15.8	12060.8	90	-0.12	0	4.2	0.021	0.062	16242794	0	1174	91520
2520	50536.6	5104.7	5.054	-1.583	0.000	-4.800	15.5	12596.8	90	-0.13	0	4.1	0.020	0.062	16551394	0	1166	89121
2580	49827.8	5009.5	5.221	-1.634	0.000	-4.959	15.2	13218.8	90	-0.14	0	4.0	0.020	0.061	16854358	0	1158	86585

t	h	v	a	a_x	a_y	a_z	M	q	ψ	γ	ϕ	α	C_D	C_L	r	l	T	c
2640	49037.8	4911.5	5.375	-1.688	0.000	-5.103	14.9	13987.7	90	-0.17	0	3.9	0.020	0.059	17151512	0	1149	83883
2700	48123.6	4809.9	5.600	-1.761	0.000	-5.316	14.7	15000.9	90	-0.19	0	3.8	0.019	0.057	17442667	0	1140	81534
2760	47171.0	4704.2	5.759	-1.830	0.000	-5.461	14.4	16310.8	90	-0.20	0	3.6	0.018	0.054	17727579	0	1131	78726
2820	46123.0	4594.2	5.962	-1.912	0.000	-5.647	14.1	17951.2	90	-0.23	0	3.4	0.017	0.051	18006002	0	1121	76096
2880	44962.3	4480.3	6.219	-2.012	0.000	-5.884	13.8	20011.2	90	-0.27	0	3.1	0.016	0.048	18277677	0	1112	73645
2940	43608.6	4362.9	6.416	-2.112	0.000	-6.059	13.5	22847.1	90	-0.32	0	2.8	0.015	0.043	18542415	0	1102	71102
3000	42027.6	4236.7	6.485	-2.271	0.000	-6.074	13.2	26780.4	90	-0.39	0	2.4	0.014	0.037	18799823	0	1090	68143
3060	40159.9	4092.7	7.039	-2.689	0.000	-6.505	12.9	32943.3	90	-0.45	0	2.1	0.013	0.032	19049094	0	1084	66521
3120	38443.9	3923.0	7.486	-3.085	0.000	-6.821	12.4	38996.4	90	-0.36	0	1.8	0.013	0.028	19288831	0	1069	62959
3180	37218.5	3733.3	7.789	-3.318	0.000	-7.047	11.9	42301.2	90	-0.25	0	1.7	0.013	0.027	19517640	0	1043	57107
3240	36368.3	3532.9	7.934	-3.421	0.000	-7.159	11.3	42925.8	90	-0.21	0	1.7	0.013	0.027	19734654	0	1009	49938
3300	35575.7	3327.4	8.214	-3.503	0.000	-7.430	10.7	42976.7	90	-0.23	0	1.8	0.013	0.028	19939457	0	973	43134
3360	34739.6	3117.4	8.456	-3.583	0.000	-7.659	10.1	43018.9	90	-0.27	0	1.8	0.013	0.029	20131773	0	934	36634
3420	33815.3	2901.2	8.731	-3.736	0.000	-7.891	9.4	43047.7	90	-0.32	0	1.8	0.014	0.030	20311291	0	891	30441
3480	32771.6	2675.7	8.980	-3.903	0.000	-8.088	8.7	43062.9	90	-0.40	0	1.8	0.015	0.030	20477512	0	845	24585
3540	31578.9	2440.8	9.266	-4.079	0.000	-8.320	8.0	43076.9	90	-0.50	0	1.8	0.015	0.031	20629874	0	795	19211
3600	30163.8	2190.0	9.579	-4.496	0.000	-8.458	7.3	43069.1	90	-0.68	0	1.7	0.017	0.032	20767653	0	736	14151
3660	28466.1	1913.8	9.950	-4.985	0.000	-8.611	6.4	43060.6	90	-0.95	0	1.7	0.019	0.032	20889502	0	668	9584
3720	26183.4	1600.0	10.458	-6.166	0.000	-8.447	5.3	43017.0	90	-1.70	0	1.5	0.023	0.032	20993646	0	582	5537
3780	22538.3	1198.5	11.368	-8.136	0.000	-7.940	4.0	42953.8	90	-3.67	0	1.2	0.031	0.030	21076012	0	463	2220
3840	14148.7	610.9	16.157	-15.554	0.000	4.370	2.1	42603.5	90	-24.09	0	-0.4	0.059	-0.017	21128163	0	273	267

Table C-3: Low lift to drag entry along the APC (See Section 3.3.1.2)

t	h	v	a	a_x	a_y	a_z	M	q	ψ	γ	ϕ	α	C_D	C_L	r	l	T	c
0	100457.0	7448.6	0.002	-0.002	0.000	0.000	25.7	14.5	90	-0.98	0	0	0.026	0.000	0	0	628	7499
60	93136.6	7457.6	0.009	-0.009	0.000	0.000	26.6	54.7	90	-0.89	0	0	0.026	0.000	447178	0	720	12955
120	86521.1	7465.0	0.028	-0.028	0.000	0.000	27.0	171.9	90	-0.80	0	0	0.026	0.000	894856	0	808	20504
180	80638.9	7469.7	0.074	-0.074	0.000	0.000	27.0	457.9	90	-0.70	0	0	0.026	0.000	1342898	0	885	29550
240	75498.0	7469.2	0.167	-0.167	0.000	0.000	26.1	1028.2	90	-0.61	0	0	0.026	0.000	1791063	0	947	38767
300	71066.5	7460.6	0.318	-0.318	0.000	0.000	25.2	1973.9	90	-0.53	0	0	0.026	0.000	2238941	0	987	45777
360	67244.6	7440.8	0.509	-0.509	0.000	0.000	24.4	3331.6	90	-0.46	0	0	0.025	0.000	2685927	0	1000	48223
370	66654.8	7436.3	0.544	-0.544	0.000	0.000	24.3	3610.3	90	-0.45	0	0	0.024	0.000	2760288	0	1000	48099
380	65952.7	7394.5	9.105	-4.455	0.000	-7.940	24.0	3931.9	91	-0.58	88	20	0.183	0.326	2834336	35	1563	287457
390	65255.5	7349.1	9.836	-4.798	0.000	-8.586	23.8	4246.9	91	-0.48	78	20	0.183	0.327	2907939	146	1572	294296
400	64687.9	7300.4	10.442	-5.081	0.000	-9.122	23.5	4507.5	92	-0.43	89	20	0.182	0.327	2981065	340	1577	298384
410	64120.1	7248.9	11.077	-5.375	0.000	-9.686	23.3	4780.5	93	-0.48	93	20	0.182	0.328	3053682	623	1582	302105
420	63479.3	7194.3	11.851	-5.733	0.000	-10.372	23.0	5113.4	93	-0.53	90	20	0.181	0.328	3125761	998	1588	306795
430	62788.9	7135.9	12.746	-6.144	0.000	-11.167	22.7	5498.7	94	-0.56	87	20	0.181	0.328	3197265	1473	1595	311936
440	62108.8	7073.2	13.673	-6.568	0.000	-11.993	22.4	5898.0	95	-0.52	82	20	0.180	0.329	3268153	2053	1601	316265
450	61503.2	7006.4	14.511	-6.947	0.000	-12.740	22.1	6258.1	96	-0.47	83	20	0.179	0.329	3338384	2744	1603	318449
460	60961.3	6935.9	15.263	-7.285	0.000	-13.413	21.8	6578.2	97	-0.43	83	20	0.179	0.330	3407919	3553	1604	318710
470	60473.4	6862.3	15.929	-7.582	0.000	-14.009	21.5	6859.0	98	-0.38	83	20	0.179	0.330	3476726	4482	1602	317278
480	60041.4	6785.8	16.488	-7.829	0.000	-14.511	21.2	7092.9	100	-0.34	82	20	0.178	0.331	3544775	5536	1598	314178
490	59658.0	6707.1	16.885	-8.003	0.000	-14.868	20.9	7256.4	101	-0.31	83	20	0.178	0.331	3612043	6717	1591	309146
500	59303.9	6626.9	17.213	-8.144	0.000	-15.165	20.6	7389.5	102	-0.30	83	20	0.178	0.332	3678512	8026	1584	303231

t	h	v	a	a_x	a_y	a_z	M	q	ψ	γ	ϕ	α	C_D	C_L	r	l	T	c
510	58947.5	6545.2	17.541	-8.285	0.000	-15.461	20.3	7522.2	103	-0.32	84	20	0.178	0.332	3744168	9463	1576	297115
520	58558.9	6462.2	17.931	-8.453	0.000	-15.813	20.0	7681.4	105	-0.36	83	20	0.178	0.333	3808998	11028	1568	291296
530	58138.0	6377.3	18.392	-8.653	0.000	-16.229	19.8	7868.2	106	-0.39	82	20	0.178	0.333	3872983	12721	1560	285703
540	57699.4	6290.3	18.889	-8.869	0.000	-16.677	19.5	8069.3	108	-0.41	82	20	0.178	0.334	3936103	14543	1553	280036
550	57246.5	6201.2	19.414	-9.097	0.000	-17.151	19.1	8281.7	109	-0.43	82	20	0.178	0.335	3998338	16493	1544	274214
560	56774.2	6109.8	19.980	-9.341	0.000	-17.662	18.8	8510.7	111	-0.46	81	20	0.177	0.336	4059664	18571	1536	268293
570	56277.4	6015.9	20.600	-9.609	0.000	-18.222	18.5	8761.9	112	-0.49	81	20	0.177	0.336	4120057	20776	1527	262314
580	55746.6	5919.1	21.300	-9.911	0.000	-18.853	18.2	9046.0	114	-0.54	81	20	0.177	0.337	4179490	23109	1519	256365
590	55176.3	5819.3	22.103	-10.257	0.000	-19.579	17.8	9370.7	116	-0.59	81	20	0.177	0.338	4237932	25569	1510	250454
600	54575.0	5715.8	22.989	-10.637	0.000	-20.380	17.5	9727.8	118	-0.63	81	20	0.177	0.339	4295348	28156	1501	244369
610	53932.5	5608.5	23.980	-11.062	0.000	-21.276	17.1	10128.1	120	-0.70	82	20	0.177	0.340	4351700	30868	1491	238158
620	53213.7	5496.7	25.134	-11.556	0.000	-22.320	16.8	10595.5	122	-0.80	81	20	0.176	0.341	4406945	33704	1481	231958
630	52432.4	5379.8	26.477	-12.128	0.000	-23.536	16.4	11140.4	124	-0.87	81	20	0.176	0.342	4461033	36664	1471	225678
640	51600.9	5256.9	27.984	-12.768	0.000	-24.901	16.0	11751.6	127	-0.96	81	20	0.176	0.343	4513906	39744	1460	219024
650	50693.0	5127.1	29.797	-13.561	0.000	-26.532	15.6	12470.0	130	-1.09	82	20	0.176	0.344	4565499	42941	1448	212147
660	49664.6	4988.6	32.074	-14.570	0.000	-28.573	15.1	13371.0	133	-1.29	84	20	0.176	0.345	4615727	46253	1437	205262
670	48402.6	4838.8	35.324	-16.012	0.000	-31.487	14.7	14671.7	136	-1.74	87	20	0.176	0.347	4664483	49672	1426	199199
680	46861.3	4670.9	40.559	-18.330	0.000	-36.181	14.3	16775.9	140	-2.05	89	20	0.177	0.349	4711603	53191	1418	194721
690	44932.4	4475.3	48.719	-21.929	0.000	-43.505	13.7	20050.1	145	-2.93	97	20	0.177	0.351	4756831	56799	1410	190629
700	42006.7	4230.7	65.521	-29.348	0.000	-58.581	13.2	26817.4	152	-5.02	104	20	0.177	0.353	4799715	60469	1409	189934
710	37968.1	3870.7	100.369	-44.843	0.000	-89.794	12.3	40722.8	162	-4.90	67	20	0.178	0.356	4839231	64142	1398	183997
720	35805.1	3400.2	108.227	-48.378	0.000	-96.812	10.9	43284.2	176	-2.94	83	20	0.181	0.362	4874338	67670	1293	134559
730	33911.6	2920.3	109.406	-48.979	0.000	-97.830	9.5	42967.2	-166	-4.18	90	20	0.184	0.368	4904695	70783	1164	88558

t	h	v	a	a_x	a_y	a_z	M	q	ψ	γ	ϕ	α	C_D	C_L	r	l	T	c
740	31565.0	2433.2	111.827	-50.181	0.000	-99.936	8.0	42897.5	-145	-6.21	91	20	0.189	0.377	4930167	73192	1022	52484
750	28620.9	1931.7	116.688	-52.784	0.000	-104.067	6.4	42807.0	-118	-9.88	96	20	0.199	0.393	4950595	74626	856	25881
760	24562.5	1403.2	127.270	-58.522	0.000	-113.017	4.7	42432.1	-80	-21.14	112	20	0.223	0.431	4965650	74931	655	8880
765	21852.7	1123.3	133.291	-60.588	0.000	-118.725	3.8	42173.8	-53	-32.31	119	20	0.232	0.455	4970888	74717	538	4044
770	18524.0	860.7	136.784	-57.533	0.000	-124.096	2.9	41644.7	-17	-57.84	139	20	0.223	0.482	4974525	74436	427	1600

(this area intentionally left blank)

Table C-4: Entry with high cross range (See Section 3.3.2)

t	h	v	a	a_x	a_y	a_z	M	q	ψ	γ	ϕ	α	C_D	C_L	r	l	T	c
0	100518.8	7451.8	0.010	-0.004	0.000	-0.009	25.7	14.4	90.0	-0.82	-50.6	7.4	0.048	0.104	0	0	675	10013
60	94485.0	7459.0	0.031	-0.013	0.000	-0.028	26.4	43.1	90.0	-0.72	-50.5	7.4	0.049	0.104	447326	19	774	17325
120	89246.6	7464.4	0.077	-0.033	0.000	-0.070	27.0	108.3	90.0	-0.61	-50.5	7.4	0.049	0.104	895033	120	869	27443
180	84920.4	7466.9	0.161	-0.068	0.000	-0.145	27.0	225.1	89.9	-0.49	-50.5	7.4	0.049	0.104	1342978	419	951	39437
240	81677.2	7465.5	0.275	-0.117	0.000	-0.249	27.0	385.5	89.9	-0.34	-50.5	7.4	0.049	0.104	1790954	1121	1016	51430
300	79717.0	7459.6	0.379	-0.161	0.000	-0.343	26.9	531.1	89.8	-0.16	-50.5	7.4	0.049	0.104	2238697	2498	1057	60114
360	79150.4	7451.6	0.095	-0.095	0.000	0.003	26.7	581.3	89.7	0.00	45.0	-0.1	0.026	-0.001	2685976	4747	869	27480
420	79217.5	7444.2	0.297	-0.133	0.000	0.266	26.7	573.8	89.6	0.01	50.1	-5.3	0.037	-0.075	3132826	7485	430	1648
480	79234.0	7436.8	0.226	-0.116	0.000	0.194	26.7	571.1	89.5	0.00	49.1	-3.9	0.033	-0.055	3579215	10841	650	8625
540	79231.4	7430.1	0.193	-0.109	0.000	0.160	26.7	570.3	89.5	0.00	48.4	-3.2	0.031	-0.045	4025186	14669	705	11921
600	79233.7	7423.7	0.173	-0.105	0.000	0.138	26.7	569.1	89.4	0.00	47.9	-2.8	0.030	-0.039	4470767	18840	734	13994
660	79236.0	7417.6	0.152	-0.101	0.000	0.114	26.6	568.0	89.4	0.00	47.3	-2.3	0.029	-0.032	4915975	23268	762	16240
720	79237.9	7411.6	0.134	-0.099	0.000	0.091	26.6	566.9	89.4	0.00	46.6	-1.8	0.028	-0.026	5360819	27864	786	18380
780	79239.5	7405.7	0.119	-0.097	0.000	0.069	26.6	565.8	89.4	0.00	46.0	-1.4	0.028	-0.020	5805306	32541	807	20393
840	79241.0	7399.9	0.107	-0.096	0.000	0.049	26.6	564.8	89.4	0.00	45.5	-1.0	0.027	-0.014	6249444	37218	825	22303
900	79242.3	7394.2	0.098	-0.094	0.000	0.029	26.6	563.8	89.4	0.00	45.2	-0.6	0.027	-0.008	6693239	41815	841	24116
960	79243.5	7388.7	0.093	-0.092	0.000	0.010	26.5	562.9	89.4	0.00	45.0	-0.2	0.027	-0.003	7136700	46259	856	25852
1020	79244.5	7383.2	0.093	-0.092	0.000	-0.009	26.5	562.0	89.5	0.00	-45.0	0.2	0.026	0.003	7579831	50480	870	27567
1080	79245.1	7377.7	0.098	-0.093	0.000	-0.028	26.5	561.0	89.5	0.00	-45.2	0.6	0.027	0.008	8022630	54453	883	29311
1140	79245.4	7372.0	0.106	-0.095	0.000	-0.048	26.5	560.2	89.5	0.00	-45.5	1.0	0.027	0.014	8465092	58205	896	31106
1200	79245.3	7366.3	0.118	-0.096	0.000	-0.068	26.5	559.3	89.5	0.00	-46.0	1.4	0.028	0.020	8907213	61766	909	32955

t	h	v	a	a_x	a_y	a_z	M	q	ψ	γ	ϕ	α	C_D	C_L	r	l	T	c
1260	79245.0	7360.5	0.133	-0.098	0.000	-0.090	26.4	558.5	89.6	0.00	-46.6	1.8	0.028	0.026	9348986	65172	922	34863
1320	79244.4	7354.6	0.150	-0.099	0.000	-0.112	26.4	557.6	89.6	0.00	-47.3	2.3	0.029	0.032	9790409	68462	935	36848
1380	79243.7	7348.6	0.169	-0.102	0.000	-0.135	26.4	556.8	89.6	0.00	-47.9	2.8	0.030	0.039	10231474	71680	948	38903
1440	79242.8	7342.3	0.192	-0.107	0.000	-0.159	26.4	555.9	89.6	0.00	-48.5	3.3	0.031	0.046	10672169	74872	961	41073
1500	79241.6	7335.7	0.217	-0.112	0.000	-0.186	26.3	555.0	89.6	0.00	-49.0	3.8	0.033	0.054	11112478	78091	974	43371
1560	79240.2	7328.9	0.243	-0.117	0.000	-0.213	26.3	554.1	89.6	0.00	-49.6	4.4	0.034	0.062	11552382	81394	987	45798
1620	79238.6	7321.7	0.272	-0.123	0.000	-0.242	26.3	553.2	89.5	0.00	-50.0	5.0	0.036	0.071	11991865	84843	1001	48316
1680	79237.1	7314.0	0.303	-0.134	0.000	-0.272	26.3	552.1	89.5	0.00	-50.2	5.6	0.039	0.080	12430900	88504	1014	50925
1740	79235.1	7305.6	0.338	-0.147	0.000	-0.305	26.2	551.0	89.5	0.00	-50.4	6.4	0.043	0.089	12869448	92440	1028	53761
1800	79232.5	7296.4	0.377	-0.161	0.000	-0.341	26.2	549.9	89.4	0.00	-50.5	7.1	0.047	0.100	13307463	96722	1042	56900
1860	79225.3	7286.5	0.390	-0.165	0.000	-0.353	26.2	549.0	89.3	0.00	-50.5	7.4	0.049	0.104	13744901	101423	1046	57780
1920	79160.4	7276.6	0.393	-0.167	0.000	-0.356	26.1	553.4	89.3	-0.02	-50.5	7.4	0.049	0.104	14181745	106558	1047	57816
1980	78959.6	7266.8	0.405	-0.172	0.000	-0.366	26.0	570.2	89.2	-0.04	-50.5	7.4	0.049	0.104	14617998	112111	1050	58481
2040	78561.7	7256.7	0.430	-0.182	0.000	-0.390	25.9	606.7	89.2	-0.07	-50.5	7.4	0.049	0.104	15053653	118083	1057	60081
2100	77931.5	7246.1	0.474	-0.201	0.000	-0.430	25.8	669.6	89.1	-0.10	-50.6	7.4	0.048	0.104	15488687	124510	1069	62831
2160	77065.0	7234.4	0.539	-0.227	0.000	-0.488	25.5	761.2	89.0	-0.13	-50.6	7.4	0.048	0.104	15923050	131469	1084	66631
2220	75991.7	7221.2	0.630	-0.265	0.000	-0.572	25.3	892.0	88.9	-0.15	-50.6	7.4	0.048	0.104	16356660	139088	1104	71682
2280	74781.6	7205.4	0.752	-0.315	0.000	-0.683	25.0	1065.9	88.8	-0.17	-50.6	7.3	0.048	0.104	16789390	147557	1127	77787
2340	73544.2	7186.4	0.899	-0.375	0.000	-0.817	24.7	1277.1	88.6	-0.16	-50.7	7.3	0.047	0.103	17221066	157136	1150	84425
2400	72412.5	7163.5	1.057	-0.439	0.000	-0.962	24.4	1503.5	88.4	-0.14	-50.7	7.3	0.047	0.103	17651466	168138	1171	90730
2460	71506.0	7136.6	1.193	-0.494	0.000	-1.086	24.2	1699.6	88.1	-0.10	-50.7	7.3	0.047	0.103	18080350	180894	1186	95457
2520	70870.0	7106.6	1.291	-0.533	0.000	-1.176	23.9	1840.4	87.8	-0.07	-50.7	7.3	0.047	0.103	18507507	195671	1195	98259
2580	70448.9	7074.3	1.357	-0.558	0.000	-1.236	23.8	1933.2	87.5	-0.05	-50.8	7.3	0.047	0.103	18932782	212637	1199	99622

t	h	v	a	a_x	a_y	a_z	M	q	ψ	γ	ϕ	α	C_D	C_L	r	l	T	c
2640	70106.2	7040.7	1.409	-0.578	0.000	-1.285	23.6	2007.8	87.2	-0.05	-50.8	7.3	0.047	0.103	19356071	231872	1201	100389
2700	69670.8	7005.9	1.480	-0.606	0.000	-1.351	23.4	2111.5	86.9	-0.07	-50.8	7.3	0.046	0.103	19777301	253419	1205	101677
2760	69001.2	6969.1	1.603	-0.654	0.000	-1.464	23.2	2292.2	86.5	-0.11	-50.8	7.3	0.046	0.103	20196378	277355	1213	104458
2820	68046.1	6929.1	1.800	-0.729	0.000	-1.646	22.9	2585.9	86.1	-0.15	-50.9	7.2	0.046	0.103	20613142	303875	1227	109124
2880	66877.0	6884.1	2.074	-0.828	0.000	-1.901	22.5	3000.4	85.6	-0.17	-51.0	7.2	0.045	0.102	21027339	333342	1244	115294
2940	65676.0	6832.8	2.377	-0.936	0.000	-2.185	22.2	3478.4	85.1	-0.16	-51.1	7.1	0.043	0.102	21438621	366289	1259	121213
3000	64632.3	6775.3	2.639	-1.025	0.000	-2.432	21.8	3910.2	84.4	-0.13	-51.2	7.0	0.042	0.101	21846604	403300	1269	125135
3060	63811.2	6712.8	2.846	-1.094	0.000	-2.627	21.5	4265.7	83.7	-0.11	-51.3	7.0	0.041	0.100	22250958	444846	1274	127075
3120	63131.8	6646.5	3.019	-1.148	0.000	-2.792	21.2	4564.2	82.9	-0.10	-51.3	6.9	0.041	0.099	22651424	491246	1276	127806
3180	62422.5	6577.0	3.210	-1.207	0.000	-2.974	20.9	4897.1	82.0	-0.12	-51.4	6.8	0.040	0.098	23047797	542726	1278	128524
3240	61527.8	6503.6	3.468	-1.286	0.000	-3.221	20.5	5375.0	81.1	-0.15	-51.5	6.7	0.039	0.097	23439870	599537	1282	130056
3300	60404.6	6425.1	3.829	-1.392	0.000	-3.568	20.1	6066.8	80.1	-0.19	-51.7	6.6	0.037	0.095	23827368	662077	1288	132725
3360	59177.7	6339.8	4.270	-1.516	0.000	-3.992	19.7	6865.7	78.9	-0.19	-51.8	6.5	0.036	0.094	24209923	730970	1295	135746
3420	58060.4	6247.3	4.666	-1.620	0.000	-4.376	19.3	7621.3	77.6	-0.17	-52.0	6.4	0.034	0.093	24587101	806969	1299	137020
3480	57137.6	6149.3	4.977	-1.694	0.000	-4.680	19.0	8251.1	76.1	-0.14	-52.1	6.3	0.033	0.092	24958528	890697	1297	136286
3540	56419.9	6043.7	5.241	-1.756	0.000	-4.938	18.6	8691.8	74.4	-0.09	-52.2	6.3	0.033	0.092	25323840	982687	1292	134222
3600	55838.3	5936.7	5.701	-1.885	0.000	-5.380	18.2	8999.1	72.7	-0.12	-52.3	6.6	0.034	0.097	25682762	1083388	1292	134241
3660	55191.3	5822.8	6.121	-1.996	0.000	-5.787	17.8	9365.1	70.7	-0.13	-52.4	6.9	0.034	0.100	26035011	1193042	1289	132887
3720	54492.5	5702.4	6.543	-2.102	0.000	-6.196	17.4	9780.3	68.6	-0.15	-52.5	7.0	0.035	0.102	26380196	1312099	1283	130726
3780	53722.7	5576.5	6.989	-2.210	0.000	-6.631	17.0	10265.1	66.2	-0.17	-52.6	7.1	0.035	0.104	26717958	1440944	1277	128082
3840	52862.4	5444.7	7.489	-2.326	0.000	-7.119	16.6	10840.2	63.5	-0.20	-52.8	7.2	0.035	0.106	27047964	1579934	1270	125180
3900	51942.1	5307.1	7.937	-2.417	0.000	-7.561	16.2	11496.8	60.6	-0.22	-52.9	7.2	0.034	0.106	27369857	1729409	1259	121097
3960	50943.2	5162.3	8.375	-2.505	0.000	-7.992	15.7	12266.0	57.4	-0.25	-53.0	7.1	0.033	0.105	27683246	1889504	1246	116162

t	h	v	a	a_x	a_y	a_z	M	q	ψ	γ	ϕ	α	C_D	C_L	r	l	T	c
4020	49834.4	5012.4	9.38€	-2.788	0.000	-8.962	15.2	13223.2	53.8	-0.30	-53.0	7.4	0.034	0.110	27987736	2060183	124	114366
4080	48527.6	4855.6	9.98€	-2.930	0.000	-9.550	14.8	14549.8	49.9	-0.37	-53.1	7.1	0.033	0.106	28283009	2241244	1226	103839
4140	47040.5	4691.4	11.056	-3.191	0.000	-10.585	14.3	16513.6	45.5	-0.41	-53.2	6.9	0.031	0.104	28568612	2432231	1215	104888
4200	45409.3	4523.5	11.825	-3.324	0.000	-11.348	13.9	19187.1	40.6	-0.48	-53.4	6.3	0.028	0.096	28844234	2632538	1196	98742
4260	43708.5	4345.1	12.079	-3.262	0.000	-11.631	13.4	22352.9	34.8	-0.37	-53.6	5.5	0.024	0.084	29109535	2841173	1169	90148
4320	43387.5	4151.4	11.692	-3.171	0.000	-11.254	12.8	21324.1	28.0	-0.11	-53.6	5.5	0.024	0.085	29363441	3056925	1132	79031
4380	43025.3	3967.5	11.346	-3.085	0.000	-10.919	12.3	20471.1	21.3	-0.43	-53.6	5.6	0.024	0.086	29606042	3276421	1095	69398
4440	41243.5	3777.3	13.219	-3.506	0.000	-12.746	11.8	23902.8	13.6	-0.66	-53.7	5.5	0.024	0.086	29837536	3496231	1081	65810
4500	40111.1	3560.3	14.046	-3.713	0.000	-13.547	11.2	25110.2	3.9	-0.24	-53.7	5.5	0.024	0.087	30056660	3712095	1047	57987
4560	42723.2	3353.0	8.944	-2.483	0.000	-8.593	10.4	15242.6	0.0	1.83	0.0	5.7	0.026	0.091	30262789	3917857	954	39929
4620	47147.4	3231.9	4.949	-1.522	0.000	-4.709	9.9	7723.6	0.3	-0.33	0.0	6.1	0.032	0.099	30459295	4113574	863	27310
4680	41840.2	3139.0	9.018	-2.500	0.000	-8.665	9.8	15110.5	0.7	-2.57	0.0	5.7	0.027	0.093	30650019	4303425	914	33626
4740	39407.4	2952.4	11.537	-3.140	0.000	-11.101	9.3	19160.7	1.0	1.24	0.0	5.6	0.026	0.094	30832171	4485430	902	31948
4800	44019.8	2803.1	5.826	-1.742	0.000	-5.562	8.6	8913.8	1.4	0.28	0.0	6.0	0.032	0.101	31003565	4656453	804	20115
4860	40546.0	2703.1	8.516	-2.382	0.000	-8.176	8.5	13573.6	1.7	-2.60	0.0	5.7	0.028	0.097	31168221	4820498	820	21755
4920	37287.7	2525.7	12.066	-3.300	0.000	-11.606	8.1	19165.3	2.1	0.75	0.0	5.6	0.028	0.098	31324603	4976846	814	21141
4980	40959.6	2361.3	6.696	-1.979	0.000	-6.396	7.4	9741.8	2.5	0.42	0.0	5.9	0.033	0.106	31469917	5122040	724	13277
5040	38250.4	2248.1	8.957	-2.547	0.000	-8.587	7.1	13177.2	3.0	-2.57	0.0	5.8	0.031	0.105	31607590	5259330	723	13153
5100	35480.2	2067.9	11.728	-3.325	0.000	-11.247	6.7	16850.6	3.4	0.62	0.0	5.8	0.032	0.108	31736539	5388357	700	11598
5160	37900.5	1898.0	7.401	-2.207	0.000	-7.064	6.0	9839.0	3.9	0.01	0.0	6.0	0.036	0.115	31854263	5506092	625	7346
5220	35105.3	1768.5	10.003	-2.948	0.000	-9.564	5.7	13073.3	4.4	-2.58	0.0	5.9	0.036	0.118	31963643	5615287	611	6715
5280	33638.0	1571.8	10.862	-3.308	0.000	-10.346	5.1	12989.3	4.9	0.91	0.0	6.0	0.041	0.129	32063135	5715014	561	4774
5340	34688.6	1397.5	8.005	-2.567	0.000	-7.582	4.5	8714.8	5.3	-1.16	0.0	6.2	0.048	0.141	32150993	5802992	495	2399

t	h	v	a	a_x	a_y	a_z	M	q	ψ	γ	ϕ	α	C_D	C_L	r	l	T	c
5400	31366.5	1244.7	11.046	-3.521	0.000	-10.469	4.1	11573.0	5.8	-2.72	0.0	6.2	0.049	0.146	32229634	5881685	466	2278
5460	30848.0	1015.1	10.750	-3.843	0.000	-10.039	3.3	8335.9	6.3	1.54	0.0	8.7	0.075	0.195	32296617	5949189	400	1240
5520	31159.9	820.9	7.866	-2.849	0.000	-7.332	2.7	5196.4	6.8	-3.50	0.0	10.0	0.089	0.228	32350126	6003081	333	595
5580	26337.5	675.2	11.465	-4.227	0.000	-10.657	2.3	7478.4	7.3	-6.38	0.0	10.0	0.091	0.230	32394328	6047499	300	388

(this area intentionally left blank)

APPENDIX D: 6-DOF SIMULATOR DESCRIPTION

D.1 Model Block Diagram

The description of the block diagram for the trajectory simulator refers to Figure D-1. In the figure each block is labeled with a number. The blocks are described in the order of their numbers. They are all SIMULINK "subsystems" in that they each contain more sub-blocks. For the purpose of the description the different levels are not explained to the last detail, as the model includes about six hundred elementary SIMULINK blocks.

The blocks reused from the trajectory simulator are not numbered or described. For information on these blocks refer to Appendix B.

All blocks sending simulation data to the MATLAB workspace have been deleted for clarity.

For additional details the reader is referred to the actual SIMULINK files; these are available from the archives of the Space Systems Development Laboratory at Stanford University.

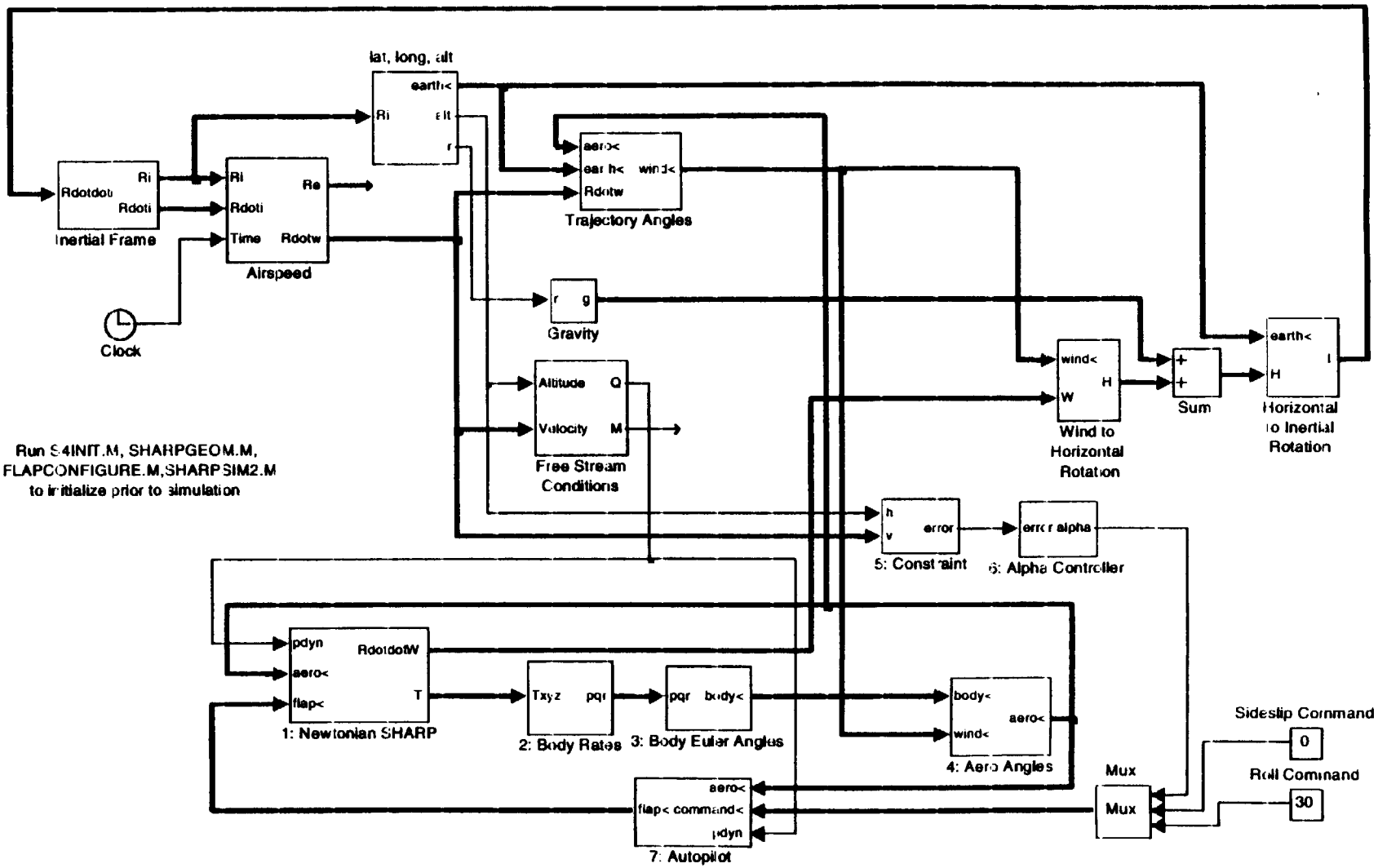

Figure D-1: 6-DOF simulator block diagram

D.2 Block Descriptions

1) **Newtonian SHARP**: This block computes the aerodynamic forces and moments experienced by the SHARP vehicle using the Newtonian model described in Chapter 4. The Newtonian model is recomputed at each simulation step using calls to the MATLAB function 'newtonsharp.m'. This file is further described in section D.3. The input to the MATLAB call requires dynamic pressure, angle of attack, angle of sideslip, and the six flap position angles. The output is the force on the vehicle (in the wind frame) as well as the moment (in the body frame). The force is divided by mass so that acceleration is passed to the 'Wind to Horizontal Rotation' block as before.

2) **Body Rates**: This block uses the moment (in the body frame) to produce the body rotation rates p, q and r (about the body axes). With the principal axes of the vehicle aligned with the body axes, the rates are computed according to the following equations:

$$\dot{p} = \frac{T_x - (I_z - I_y)qr}{I_x}$$

$$\dot{q} = \frac{T_y - (I_x - I_z)pr}{I_y}$$

$$\dot{r} = \frac{T_z - (I_y - I_x)pq}{I_z}$$

The three equations are solved by taking the rates, the body moments and the inertia properties. The resulting dotted quantities are integrated to find p, q and r, and fed back into the computation. The integrator initial condition is specified in the simulation initial conditions as initial yaw, pitch and roll rates.

3) **Body Euler Angles**: This block calculates the Euler angles of the body frame with respect to the horizontal frame. The Euler angles are combined with p, q and r to find the rate of change of the Euler angles according to the kinematic relation:

$$\begin{bmatrix} \dot{\psi} \\ \dot{\gamma} \\ \dot{\phi} \end{bmatrix} = \begin{bmatrix} 0 & \frac{\sin\phi}{\cos\gamma} & \frac{\cos\phi}{\cos\gamma} \\ 0 & \cos\phi & -\sin\phi \\ 1 & \tan\gamma\sin\phi & \tan\gamma\cos\phi \end{bmatrix} \begin{bmatrix} p \\ q \\ r \end{bmatrix}$$

The angles in this relation are the body Euler angles and should not be confused with the wind frame Euler angles, which are denoted by the same symbols. The resulting Euler angle rates are integrated to solve for the Euler angles themselves, and fed back into the calculation. The initial value of the Euler angles is computed by the m-file that initializes the simulation, based on user-specified values of the aerodynamic angles.

4) **Aero Angles**: This block compares the body frame Euler angles with the wind frame Euler angles to compute the angle of attack and the angle of sideslip. The computation is a series of rotation matrix multiplications, with the key relation

$$[\alpha\hat{x}][-\beta\hat{z}] = [\phi\hat{x}]^{-1}[\gamma\hat{y}]^{-1}[\psi\hat{z}]^{-1}[\psi_B\hat{z}][\gamma_B\hat{y}][\phi\hat{x}]$$

where each quantity between brackets is a 3x3 rotation matrix by the specified angle about the specified axis (x, y or z). The body frame Euler angles are distinguished from the wind frame Euler angles by the subscript B. The angle of attack and the angle of sideslip can be extracted from the left-hand side through the inverse sine of the appropriate matrix elements.

5) **Constraint**: This block is the same as was used in Appendix B, computing the altitude error from the APC.

6) **Alpha Controller**: This block is the same as was used in Appendix B, computing a command angle of attack based on the altitude error. This PID controller forms the slow feedback loop around the autopilot's (described next) fast feedback loop.

7) **Autopilot**: This block takes aerodynamic angle commands and computes the proper position for each of the six aerodynamic control surfaces so as to achieve the desired angles. The autopilot is made of three separate PID controllers. Each of them first computes an error signal from the difference of the commanded angle and the true

angle (perfect state knowledge is assumed in this case). This error is then fed into a PID controller which outputs a relative position angle. The relative position angle is then fed through the flap logic (which flaps to deploy for what resulting motion, as depicted in Figure 4-3). The three relative flap position commands coming from each of the three controllers are added together to compute the net position command. This position command is then fed through a simple model of the flap dynamics, limiting the flap position between 0 and 10 degrees and the flap position rate to 10 degrees per second. This rate limit introduces strongly non-linear dynamics; the lower it is set, the less linear is the response to a sinusoidal excitation of the angle command. For more information on the motivation for this controller design, refer to Chapter 4.

D.3 Files for Newtonian Model

Several MATLAB m-files support the computation of the Newtonian aerodynamic model. These are briefly outlined here.

1) **sharpgeom.m**: This file initializes the geometry of the vehicle by specifying the nodes of the wire frame model as seen in the body frame (with the origin at 50% of the length of the vehicle). It also defines the variable 's6flapfraction' which determines the flap chord length as a fraction of vehicle length. This is set to 0.15 by default.
2) **flapconfigure.m**: This file prepares all the geometric data for the Newtonian model from the information specified in the previous file. The nodes of the wire frame model that depend on the flap dimensions are computed first. These consist of all the nodes in the vicinity of the flap hinge line. Next, the polygon connectivity is defined (the nodes are grouped together to form each facet of the model). The normals and centroids of each polygon, referred to the body frame, are computed using 'centroidnormal.m' described next. For the purpose of recomputing the centroid and normal of each flap polygon the hinge line vectors as well as the hinge line centers are computed for each flap. The properties of each flap polygon change at each simulation step according to flap position.

3) **centroidnormal.m**: This file takes an input of three or four nodes enumerated in counterclockwise order and computes the centroid and normal of the resulting triangle or trapezoid. Since all of the elements of the Newtonian model of SHARP have either three or four nodes, this is sufficient to compute all facets of the model. The function is based on simple vector algebra which is not detailed here.

4) **newtonsharp.m**: This file computes the force (in the wind frame) and moment (in the body frame) on the vehicle, based on inputs of angle of attack, angle of sideslip, dynamic pressure, and flap positions. Based on the aerodynamic angles, three unit basis vectors of the body frame are computed as seen in the wind frame. This is so that force calculations may be specified in the wind frame. Next, the force and moment arising from the parts of the vehicle that do not change in time (i.e. everything except the flaps) are added up, with the function 'computepolygon.m' being called for each polygon. Next, for each of the six flaps and based on the position angles the centroid and normal of each flap is recomputed before adding their contribution to the total force and moment using 'computepolygon.m' as before.

5) **computepolygon.m**: This file takes as inputs the normal and centroid of a polygon as seen in the body frame, and the basis of the body frame as seen from the wind frame. This file is where the Newtonian aerodynamics come into play. According to the description in Chapter 4, a normal force and a tangential force are computed and added to give the net force. The tangential force is determined by the coefficient of friction, specified in this file. The net force vector is projected onto the basis so the result is in wind coordinates. The moment of the two force components about the body frame origin is also computed.

6) **findangles.m**: This file performs the matrix rotations and operations detailed in the description of block 4 (aero angles) and finds the angle of attack and the angle of sideslip.

7) **animate.m**: This file is used to animate the simulation results as described in Chapter 4. An animation time step can be set in this file. The aerodynamic angles, output time vector and flap position angles are interpolated to create a regular time spacing. These resampled vectors are then used for the animation. At each step the vehicle and the six flaps are displayed using the appropriate rotations, achieved

through matrix algebra. The flaps are treated differently as the distal nodes of the polygons (away from the hinge line) must be recomputed for proper display. This is done using vector algebra, and is not detailed here. The animation function allows the inclusion of an exaggeration factor so that small motion of the flaps becomes more obvious. Since the vehicle is flown using very small flap deployments this feature is almost always used. The exaggeration factor can be set in the file.

8) **s4init.m**: This file initializes all the parameters used in the model. This represents a change from the trajectory simulator, where the parameters were specified through input dialogs on masked SIMULINK blocks. This time the variables are changed using a custom programmed graphical user interface in MATLAB. The interface, described next, operates on the variables defined in this file. The SIMULINK model then retrieves the parameters as needed from the MATLAB workspace.

9) **sharpsim.m**: This file implements the graphical user interface where the user can select the parameters for the simulation. When this file is run three buttons appear in a separate window. The first brings up a dialog to set planetary characteristics as in the trajectory simulator. The second brings up a dialog to set the trajectory initial conditions, twelve of them for six degrees of freedom. These include speed, altitude, latitude, longitude, heading angle, entry angle, angle of attack, angle of sideslip, roll angle, yaw rate, pitch rate and roll rate. Finally, the third brings up a dialog to set the vehicle parameters such as inertia properties and mass.

D.4 User's Guide

To use the 6-DOF simulator, follow these steps:

1) Launch MATLAB

2) Type 'simulink' at the prompt

3) From the SIMULINK File menu, select the model to be opened (e.g. sharp7.mdl)

4) In MATLAB, run 'sharpgeom.m'. This file creates the vehicle geometry. Then specify the variable 'só flapfraction' to set the flap size. Next, run 'flapconfigure.m' to compute the vehicle geometry for use in the Newtonian model routines. Call

's4init.m' to initialize simulation variables, and then call 'sharpsim.m' to bring up the dialog window where simulation parameters can be set and modified.

5) In MATLAB, run the m-file that specifies the entry profile to be flown (if applicable)

6) Using the appropriate dialogs, enter the desired planetary characteristics, trajectory start conditions, and vehicle parameters.

7) Place all the 'To Workspace' blocks required for collecting data to the MATLAB workspace. 'Scope' blocks may be places to monitor the value of any parameter while the simulation executes.

8) From the Simulation menu in SIMULINK, select the stop time, the integration method and the solver tolerances.

9) From the Simulation menu, select 'Start'.

10) Monitor simulation progress by clicking on the 'clock' block.

11) When simulation ends, display and analyze data using MATLAB plotting functions. Useful m-files include 'plotapc.m' for plotting the aerothermal performance constraint and 'earth3.m' for displaying a three dimensional plot of the earth for trajectory plotting. Use 'animate.m' to gain a better understanding of the attitude dynamics.

REFERENCES

[Anderson 1960]: R.A. Anderson and R.T. Swann; Structures for Reentry Heating; NASA Technical Memorandum X-313: Langley Field. VA. 1960.

[Carroll 1995]: J. Carroll; Preliminary Design of SHARP, a Sharp Hypersonic Aerodynamic Research Probe: Report on NASA Ames PO A46818D: Moffett Field. CA. 1995.

[Dommasch 1967]: D.O. Dommasch, S.S. Sherby, T.F. Connolly; Airplane Aerodynamics: 4th Edition. Pitman Publishing: New York. NY. 1967.

[Graves 1978]: C.A. Graves and J.C. Harpold; Shuttle Reentry Guidance; AAS 78-147; American Atronautical Society 25th Anniversary Conference: Houston. TX. 1978.

[Hankey 1988]: W.L. Hankey; Re-entry Aerodynamics; AIAA Education Series; Washington. DC. 1988

[Humusoft 1997]: Humusoft; Real Time Toolbox; Information on Internet at www.humusoft.cz

[JSC 1973]: Johnson Space Center; Space Shuttle Guidance, Navigation, and Control Design Equations: JSC document 04217. Volume III and IV: Houston. TX. 1973.

[Kafer 1983]: G. Kafer and D. Wilson; Space Shuttle Descent Flight Control Design Requirements and Experiments; NASA Conference Publication 2283. Part 1. Hampton. VA, 1983.

[Kolodziej 1996]: P. Kolodziej, J. Bull, D. Rasky; Tether Deployed Flight Demonstrations: NASA Ames Memorandum: Moffett Field. CA. 1996.

[Kolodziej 1997]: P. Kolodziej, personal communication of aerodynamic database calculated using the HAVOC code. June 1997.

[Kolodziej 1998]: P. Kolodziej, J.V. Bowles, C. Roberts; Optimizing Hypersonic Sharp Body Concepts from a Thermal Protection System Perspective: AIAA. 1998.

[Larson 1992]: W.J. Larson and J.R. Wertz (editors); Space Mission Analysis and Design: Microcosm/Kluwer. Torrance. CA. 1992.

[Mathworks 1997]: The MathWorks, Inc.; SIMULINK Dynamic System Simulation and MATLAB: Information on Internet at www.mathworks.com

[NASA 1998]: National Aeronautics and Space Administration; Advanced Space Transportation Programs: Information on Internet at astp.msfc.nasa.gov

[Neumann 1989]: J.J. Bertin, R. Glowinski, J. Periaux; Hypersonics: Volume 1: Defining the Hypersonic Environment: Chapter by R.D. Neumann on Defining the Aerothermodynamic Methodology; Birkhauser Boston, Cambridge, MA, 1989.

[NOAA 1976]: National Oceanic and Atmospheric Administration; U.S. Standard Atmosphere 1976: Washington, DC. 1976.

[Quinn 1990]: R.D. Quinn, L. Gong; Real-Time Aerodynamic Heating and Surface Temperature Calculations for Hypersonic Flight Simulation: NASA Technical Memorandum 4222; Edwards, CA, 1990.

[Shkadov 1975]: L.M. Shkadov, R.S. Bukhanova, V.F. Illarionov, V.P. Plokhikh; Mechanics of Optimum Three-Dimensional Motion of Aircraft in the Atmosphere: NASA TT F-777; 1975.

[Sims 1996]: B.A. Sims; Flight Code Validation Simulator; Proceedings of the SPIE conference: Technologies for Synthetic Environments: Hardware in the Loop Testing. Vol. 2741. International Society for Optical Engineering, 1996.

[STS 1998]: National Aeronautics and Space Administration; Space Shuttle Reference Manual: Information on Internet at shuttle.nasa.gov/reference/shutref/

[Tauber 1996]: M. Tauber; Atmospheric Entry; Stanford University AA213 Course Notes: Stanford. CA. 1996.

[Tiwari 1992]: S.N. Tiwari, D.J. Singh, A.K. Sehgal; Combined Effect of Nose Bluntness and Angle of Attack on Slender Bodies in Viscous Hypersonic Flows: AIAA-92-0755: 30th Aerospace Sciences Meeting and Exhibit; Reno, NV, 1992.

[Windhorst 1997]: R. Windhorst, M. Ardema, J. Bowles; Minimum Heating Re-Entry Trajectories for Advanced Hypersonic Launch Vehicles: AIAA. 1997.

[Young 1998]: L.W. Young, personal communication, 13 February 1998.